THE PREPARATION AND CHARACTERIZATION OF TUNGSTEN AND MOLYBDENUM SULFIDE FLUORIDES

JARED NIEBOER
B.Sc., University of Lethbridge, 2005

A Thesis
Submitted to the School of Graduate Studies
of the University of Lethbridge
in Partial Fulfillment of Requirements
for the Degree
MASTER OF SCIENCE

Department of Chemistry and Biochemistry
University of Lethbridge
LETHBRIDGE, ALBERTA, CANADA

ABSTRACT

Silanethiolate salts of $K(18\text{-crown-6})^+$, $N(CH_3)_4^+$, Cs^+, K^+ were synthesized and characterized by vibrational and NMR spectroscopy. The $[N(CH_3)_4][SSi(CH_3)_3]$ salt was used to prepare the new $[N(CH_3)_4][WSF_5]$ salt directly from WF_6. Alternatively, $[N(CH_3)_4][WSF_5]$ was prepared by the reaction of WSF_4 with $[N(CH_3)_4][F]$.

Pure WSF_4 was prepared via a facile new route and was fully characterized by Raman, infrared, and ^{19}F NMR spectroscopy, and an improved crystal structure. The Lewis-acid properties of WSF_4 were studied in reactions with pyridine, yielding the new $WSF_4 \cdot C_5H_5N$ adduct, which was studied by Raman and ^{19}F NMR spectroscopy. A 2:1 stoichiometry of WSF_4 and $[N(CH_3)_4][F]$ yielded $W_2S_2F_9^-$ in solution. The novel $W_2SOF_9^-$ anion was characterized in solution by ^{19}F NMR spectroscopy.

Molybdenum sulfide tetrafluoride was synthesized and unambiguously characterized by Raman, infrared, and ^{19}F NMR spectroscopy and single-crystal X-ray diffraction.

The experimental characterization of WSF_4, $MoSF_4$, WSF_5^-, and $SSi(CH_3)_3^-$ was supplemented by density functional theory calculations.

ACKNOWLEDGEMENTS

I would like to thank Prof. Michael Gerken for giving me the chance to work on an interesting and exciting research project. His patience, guidance, experience, enthusiasm, support and confidence in me were invaluable throughout my years of study. I appreciate having had the opportunity to share in his excitement for understanding fundamental chemistry.

I would like to thank the other members of my committee René T. Boeré and Steve Patitsas for their interest and investment of time into helping me further my research.

I would like to thank Prof. René T. Boeré for his patience, advice and for his instruction in the areas of X-ray crystallography and for introducing me to the value of density functional theory calculations.

I would like to thank Prof. Steve Patitsas for many years ago encouraging me to get involved in research, which opened up a world of interesting topics and my life immensely.

I thank Anwar Abo-Amer and Kati Schmuck for their company and their assistance during the course of my research.

I would also like to thank the members of the Boeré Lab, Tracy Roemmele, Twyla Gietz, Maria Ksiaczek, Xin Yu for always keeping life interesting and David Franz and Marc Slingerland for their friendship throughout the my research time.

I am grateful to have received the Keith and Hope Ferguson Memorial scholarship, which helped me cover so many costs associated with the pursuit of a graduate degree.

I would like to acknowledge the Alberta Ministry of Education and the Department of Chemistry and the University of Lethbridge for their financial support.

Finally, I thank my wife and parents for their constant support that helped me achieve my goal.

TABLE OF CONTENTS

LIST OF TABLES

LIST OF FIGURES

LIST OF ABBREVIATIONS

General

ax	axial
eq	equatorial
Kel-F	chlorotrifluoroethylene
NMR	Nuclear Magnetic Resonance
DMEU	Dimethylethyl Urea

Nuclear Magnetic Resonance

δ	chemical shift
J	scalar coupling constant in Hertz
ppm	parts per million
TMS	tetramethylsilane

X-ray Crystallography

a, b, c, *α, β, γ*	cell parameters
V	cell volume
λ	wavelength
Z	molecules per unit cell
mol. wt.	molecular weight
μ	absorption coefficient
R_1	conventional agreement index
wR_2	weighted agreement index
GOOF	goodness of fit

Chapter 1
Introduction

1.1 Introduction

It has long been known that electronegative ligands tend to stabilize metal centers in high oxidation states. As such, most metals in their highest oxidation states are surrounded by oxygen or fluorine ligands. The group six metals molybdenum and tungsten are no exception. Therefore, the introduction of the less electronegative sulfur atom to the ligand environment about the metal would be expected to cause a decrease in stability and an increase in reactivity rendering the synthesis of metal sulfide fluorides more challenging. As a result, little is known about tungsten and molybdenum sulfide fluorides in comparison to the oxide fluorides.

In the chemistry of fluorides it has been observed that many compounds form fluorine-bridged oligomeric or polymeric solids of MF_6 octahedra, often sharing vertices, sometimes edges but never faces. Similar trends have been observed for the oxide fluorides $MoOF_4$ and WOF_4 where polymeric solids contain MOF_5 octahedra. In both, the fluorides and oxide fluorides, the strong preference for a hexa-coordinate environment about the metal atom is observed.

1.2 Tungsten and Molybdenum Fluorides

Tungsten and molybdenum fluorides are useful starting materials for oxide fluorides and sulfide fluorides. They are prepared primarily by the combination of the elements in direct fluorination reactions.[1]

$$M + 3\ F_2 \rightarrow MF_6 \quad (M = Mo, W) \qquad 1.2.1$$

Tungsten fluorides exist for oxidation states four through six. They are easily identifiable by their respective physical properties. Tungsten hexafluoride is a volatile colourless liquid at temperatures below its boiling point of 17.1 °C. Tungsten pentafluoride is a pale yellow solid at room temperature while WF_4 is a red/brown solid at room temperature. Lower fluorides of tungsten have not been observed.

Tungsten pentafluoride is known to crystallize as a fluorine-bridged tetramer.[2] The arrangement allows for a pseudo-octahedral environment about tungsten with a coordination number of six. The structure of tungsten tetrafluoride is unknown though it is believed to form a fluorine-bridged polymer with coordination number six. X-ray diffraction studies have suggested that WF_4 is an amorphous solid.[3]

The combination of tungsten metal with a dilute stream of fluorine results in WF_5. Tungsten pentafluoride is noted for the ease with which it disproportionates to form WF_4 and WF_6.[4] Reactions of WF_6 with hot tungsten or nickel filaments have been shown to generate WF_5.[3,5,6] Tungsten tetrafluoride has been obtained from reduction of WF_6 with benzene at 110 °C and PF_3 (Equation 1.2.2).[7,1] It is clear from the ease with which WF_5 disproportionates and the results of reduction reactions with WF_6 that WF_4 is more stable than WF_5.

$$WF_6 + PF_3 \rightarrow WF_4 + PF_5 \qquad 1.2.2$$

$$2\ MoF_6 + PF_3 \rightarrow 2\ MoF_5 + PF_5 \qquad 1.2.3$$

Molybdenum fluorides are known for oxidation states three through six. Like the tungsten fluorides, molybdenum fluorides of different oxidation states vary in appearance significantly. Molybdenum hexafluoride, like WF_6, is a colourless volatile liquid with a freezing point of 17.4 °C, slightly higher than the boiling point of WF_6. It is well known that MoF_6 is less stable than WF_6 and is considered to be a strong oxidizing agent.

Molybdenum pentafluoride is a yellow solid with a melting point of 64 °C. The reduction of MoF_6 using PF_3 readily yields MoF_5 (Equation 1.2.3), which was attributed to the particularly stable tetrameric structure of MoF_5.[1,8] The tetrafluoride, MoF_4, was formed by the reduction of the hexafluoride with benzene at 110 °C. Mixtures of MoF_5 and MoF_4 have also been obtained from the oxidation of $Mo(CO)_6$ with F_2; the significantly higher volatility of MoF_5 allows for their separation.[9] Unlike tungsten, molybdenum forms the metal trifluoride, MoF_3, illustrating the trend of heavier group 6 transition metals to form more stable compounds in higher oxidation states. The trifluoride has been reported as both a dark-pink[10] and a tan-coloured solid.[11] It was later suggested that the pink solid could have been an oxide fluoride of unknown

composition.[11] Molybdenum fluorides also maintain a coordination number of six about molybdenum throughout all oxidation states.

The reactivity of WF_6 and MoF_6 has been compared in a series of reactions by O'Donnell *et al.*[1] Reactions between MoF_6 and WF_4 were shown to yield WF_6,[1] showing directly that MoF_6 is a stronger oxidizer than WF_6. Furthermore, quantitative comparisons of the stability of MoF_6 and WF_6 using electrochemistry[12] of their respective MF_6^- anions are in agreement with the stronger oxidizing ability of MoF_6. Halogen exchange reactions with a variety of reagents, such as PCl_3, $AsCl_3$, $SbCl_3$, CCl_4, and $SiCl_4$, have shown that MoF_6 readily undergoes reaction to form mixtures of products with $Mo_2Cl_3F_6$ being produced in all reactions, while WF_6 remains comparatively inert.[1]

The fluoride-ion affinity of WF_6 has been illustrated in reaction with alkali metal fluorides.[13] In addition, the non-alkali metal fluoride CuF_2 was found to react with WF_6 in CH_3CN to produce a blue-coloured solution, which upon removal of solvent produced a moisture-sensitive, blue solid, $CuF_2 \cdot 2WF_6 \cdot 5CH_3CN$ according to elemental analysis. Analysis of the infrared spectrum revealed the adduct to be $[Cu(NCCH_3)_5][WF_7]_2$.[14] The WF_7^- anion has been characterized by ^{19}F NMR spectroscopy for many salts. The X-ray crystal structures of $CsWF_7$ as well as that of $CsMoF_7$ show monocapped octahedral anions. The use of larger cations, such as $N(CH_3)_4^+$ and $C_{11}H_{24}N^+$, showed that the F^- ligands in the MoF_7^- anion also assume a monocapped octahedral symmetry about molybdenum, indicating that neither crystal packing nor lattice type have influence over the structure of the anion.[13] Three types of bonds were distinguished: one apical, three equatorial, and three basal bonds having varying lengths with equatorial bonds always shorter. In solution the structure was clearly fluxional as all complexes were observed as singlets by ^{19}F NMR spectroscopy.[13]

It has been argued that the very existence of WF_7^- in CH_3CN might be the result of the poor salvation of F^- by CH_3CN, as it has been observed that WF_7^- in HF immediately dissociates to form WF_6 and F^-. It was also shown that $Ag[WF_6]$ and WF_6 react in CH_3CN to produce WF_7^-.[14]

The presence of $[WF_8]^{2-}$ in solution has never been demonstrated. The MF_8^{2-} (M = Mo, W) anions have been suggested by elemental analysis[15] though there has been controversy over the existence of the MoF_8^{2-} anion as it has never been observed.

Hexavalent K_2WF_8[15] has been isolated as a white solid that is sensitive to hydrolysis. Raman spectroscopy and single-crystal X-ray diffraction of $[NO_2]_2[WF_8]$, produced in low-temperature reaction of WF_6 and substantial excess NO_2F, have determined WF_8^{2-} to be a regular square antiprism.[16]

1.3 Tungsten and Molybdenum Oxide Fluorides

Tungsten and molybdenum oxide fluorides in +6 oxidation state have been studied intensively for some time. Tungsten oxide tetrafluoride is a white solid with a melting point of 101 °C. It was first prepared by reaction of $WOCl_4$ with HF in 1907.[17] The production of WO_2F_2 from WO_2Cl_2 by analogous reaction was also attempted but was unsuccessful according to the mass balance.[17] Since then reactions between WO_3 and F_2,[18] tungsten metal and dilute F_2 with O_2 (3:1 F:O ratio)[19](5:1 F:O ratio)[20] have been shown to generate WOF_4. Small amounts of tungsten oxide tetrafluoride have also been obtained from reactions between CrO_3 and WF_6.[21] Hydrolysis reactions of WF_6 have been used in attempts to produce WOF_4, however, the single product of this reaction was found to be $[H_3O][W_2O_2F_9]$.[38] The reaction of WF_6 with SiO_2 has been used to generate WOF_4 though the presence of anionic side products that were difficult to separate were observed (Equation 1.3.3).[22,23]

$$MO_3 + F_2 \rightarrow MOF_4\ (M = Mo, W) + (\text{other products}) \qquad 1.3.1$$

$$M + F_2 + O_2 \xrightarrow{350-400\ ^\circ C} MOF_4\ (M = Mo, W) + (\text{other products}) \qquad 1.3.2$$

$$WF_6 + SiO_2 \xrightarrow{HF} WOF_4 + (WOF_5^- + W_2O_2F_9^-) \qquad 1.3.3$$

Single crystal X-ray diffraction studies show WOF_4 as a fluorine-bridged tetramer [24,25] that crystallizes in the *C2/m* space group.[26,27] Vibrational spectroscopy had previously suggested a fluorine-bridged network structure.[24,25,28-30] Initially, the solid was incorrectly determined to be oxygen-bridged,[26] which was later corrected based on the vibrational spectrum. The structure was believed to contain a significant degree of disorder between the fluorine and oxygen atoms, though the suspected disorder may have been due to quality of the X-ray diffraction data and the difficulty distinguishing between oxygen and fluorine atoms by X-ray diffraction.[28] Raman spectra of WOF_4 as a solid and

in the melt have been reported.[31] Additional Raman spectroscopy of WOF_4 in the gas phase was also performed indicating a monomeric structure of gaseous WOF_4. Polarization studies showed significant changes in intensity for bands at 1055, 733 and 248 cm^{-1}, which helped assign their symmetry as A_1.[30]

Tungsten dioxide difluoride, WO_2F_2, has been generated by the hydrolysis of WOF_4 in HF [32] and the reaction of K_2WO_4 with IF_5 yielded a white solid that exhibited peaks attributable to WO_2F_2 in its infrared spectrum.[33] Electron diffraction was performed on WO_2F_2 in the vapour phase as it was produced from heating solid W_2O_4F to 1043K.[34]

Tungsten oxide fluoride anions WOF_5^- and $W_2O_2F_9^-$ have been observed by ^{19}F NMR spectroscopy (Table 1.3.1). These anions have also been observed in the reaction of $WOCl_4$ with HF.[35] Solutions of WOF_4 in HF have also produced the $W_2O_2F_9^-$ anion.[31] The direct hydrolysis of WF_6 in HF (Equation 1.3.5) solution was reported to mainly produce $[H_3O][W_2O_2F_9]$, though production of $[H_3O][WOF_5]$ by this method was erroneously reported[36,37] since the vibrational spectra corresponded to $[H_3O][W_2O_2F_9]$.[38] The controlled reaction of WF_6 with $B(OH_3)$ in HF (Equation 1.3.4) was also found to produce exclusively $[H_3O][W_2O_2F_9]$.[36] Hydrolysis of WF_6 in aqueous HF (48 %) in the presence of two equivalents of CsF (Equation 1.3.8) resulted in the formation of $Cs_2WO_2F_4$.[38]

$$WF_6 + B(OH)_3 \xrightarrow{HF} [H_3O][W_2O_2F_9] + \text{(other products)} \qquad 1.3.4$$

$$WF_6 + 2\,H_2O \xrightarrow{HF} [H_3O][WOF_5] + HF \qquad 1.3.5$$

$$WF_6 + 2\,CsF \xrightarrow{HF\ (48\ \%)} Cs_2WO_2F_4 \qquad 1.3.6$$

The tungsten oxide fluoride anions have been generated as salts of NO^+, ClO_2^+, Cs^+, and NF_4^+. Their equilibrium reactions in HF have been the subject of considerable interest.[31,38] Studies involving infrared, Raman, and ^{19}F NMR spectroscopy were performed on the NO^+ salts of WOF_5^- and WOF_6^{2-},[31] as well as Cs^+ and NF_4^+ salts of WOF_5^-, $WO_2F_4^{2-}$ and $W_2O_2F_9^-$.[38,39]

Single-crystal X-ray diffraction studies of $[NO][WOF_5]$ have been reported, showing a pseudo-octahedral anion.[40] Dissolving $[NO][WOF_5]$ in anhydrous HF

followed by removal of HF gave a mixture of $[NO][WOF_5]$ and $[NO][W_2O_2F_9]$ based on X-ray powder diffraction.[31] The observation of a mixture indicates the presence of an equilibrium between the monomeric and dimeric anions in HF solution. Single-crystal X-ray diffraction of the $[H_3O][W_2O_2F_9]$ salt showed discrete fluorine-bridged $W_2O_2F_9^{2-}$ anions where the fluorine bridge is *trans* to the W=O bond. The complex was found to crystallize in space group $P2/c$.[36]

Alkali metal tungsten dioxide fluorides have been prepared from CsF and WO_3 in aqueous HF with dissolved Cs_2WO_4. Upon evaporation of the solvent, $Cs_2WO_2F_4$ was obtained in crystalline form. X-ray crystallography studies showed isolated $WO_2F_4^{2-}$ octahedra where fluorine and oxygen atoms were completely disordered. Crystals of $Na_2WO_2F_4$ were studied by single-crystal X-ray diffraction, also showing disorder between oxygen and fluorine. The *cis*-dioxo arrangement of the $WO_2F_4^{2-}$ anion was deduced from Raman and ^{19}F NMR spectroscopy.[41]

Molybdenum(VI) oxide fluorides, like tungsten(VI) oxide fluorides, generally appear as white solids at room temperature. Molybdenum oxide tetrafluoride, $MoOF_4$, was first studied by Ruff and Eisner in 1907.[42] Molybdenum oxide tetrafluoride has been formed in reactions of MoO_3 with F_2 (Equation 1.3.1),[18] and CrO_3 with MoF_6.[21] Direct hydrolysis of MoF_6 in HF with a deficiency of H_2O has been found to generate $MoOF_4$ almost exclusively, unlike hydrolysis of WF_6.[37] The formation of the oxide tetrafluoride was attributed to the lower electron affinity of MoF_6 compared to WF_6.[36]

$MoOF_4$ was found to crystallize in polymeric chains of distorted *cis*-fluorine-bridged $MoOF_5$ octahedra[43] in the monoclinic space group $P2_1/c$[43] ($P2_1/a$[27]), as opposed to the tungsten analogue.[27] Raman spectroscopy on solid $MoOF_4$ was performed with the resulting spectra showing weak bands in the 500 cm^{-1} region indicating fluorine bridging.[31]

Infrared spectra of $MoOF_4$ and WOF_4 were later collected in the gas phase as well as in argon and nitrogen matrices.[18,30] Gas-phase infrared spectroscopy strongly supported C_{4v} symmetry for monomeric molecules. It was noticed that the gas-phase spectra observed for $MoOF_4$ were of poorer quality than for WOF_4, which was attributed to the seven isotopes of molybdenum between mass numbers 92 and 100. The Raman and

infrared spectra of gaseous and matrix-isolated $MoOF_4$ and WOF_4 were quite similar indicating related structures.[30]

The molybdenum dioxide difluoride analogue, MoO_2F_2, has been generated in reaction between MoO_2Cl_2 and HF. A similar reaction with stoichiometric amounts of XeF_2 also formed MoO_2F_2, greater amounts of XeF_2 formed $MoOF_4$.[32] Molybdenum dioxide difluoride has been characterized by Raman spectroscopy as both a solid and a melt.[28,31]

The reagent NOF was shown to react with $MoOF_4$ in HF yielding $[NO][MoOF_5]$. Single-crystal X-ray diffraction studies of $[NO][MoOF_5]$ have been reported.[40]

The formation of the dimeric $Mo_2O_2F_9^-$ anion in solutions of $MoOF_4$ in HF has been observed by ^{19}F NMR spectroscopy. The H_2F^+ cation was suggested as a possible counter ion, but has not been confirmed by its experimental observation. The equilibrium between $[NO][MoOF_5]$ and $[NO][Mo_2O_2F_9]$ in HF has been studied by powder X-ray diffraction.[31] Fluorine-19 NMR spectroscopy studies of the reaction of $MoOF_4$ with acetylacetone in CH_3CN have also shown the presence of the $Mo_2O_2F_9^-$ anion.[44] The formation of the dimeric anion from HF solutions of MOF_4 (M = Mo, W) tends to be favoured for solutions of WOF_4 in HF indicating stronger acceptance of F^- by WOF_4 compared to $MoOF_4$.[31]

Reactions of MoO_3 and WO_3 with SeF_4 and IF_5 reportedly produced the $[SeF_3][MoO_2F_3]$, $[IF_4][MoO_2F_3]$ and $[SeF_3][WOF_5]$, $[SeOF][WOF_5]$, $[IF_4][WOF_5]$ salts. The nature of the salts were solely deduced by the mass balance of the reaction. Addition of KF to the reaction of SeF_4 and WO_3 was said to produce $K[WOF_5]$.[45]

The Lewis-acid properties of the tungsten oxide fluorides towards nitrogen bases have been studied by single crystal X-ray diffraction, where possible, and vibrational and NMR spectroscopy. The formation of the tungsten oxide-fluoride adducts with pyridine and bipyridine, $WOF_4 \cdot bipy$[46], $WO_2F_2 \cdot bipy$[46], $WOF_4 \cdot py$[47], and $WOF_4 \cdot 2py$,[47,48] were studied. The $WOF_4 \cdot py$ adduct was shown to take the form of a distorted octahedron with the oxygen atom trans to the nitrogen ligand of pyridine. The dipyridyl analogue, $WOF_4 \cdot 2py$ exhibited a pentagonal bipyramidal geometry about tungsten. Low-temperature ^{19}F NMR spectroscopy showed an A_2MX spin system for $WOF_4 \cdot 2py$.[48] At

temperatures above 0 °C the WOF_4·2py adduct was shown to give up a pyridine ligand as only WOF_4·py and free pyridine were observed.[47]

When 2-fluoropyridine was introduced as a ligand only the mono F-pyridine, WOF_4·Fpy adduct was observed. The adduct was studied by vibrational and NMR spectroscopy along with single-crystal X-ray crystal and powder diffraction showing the tungsten with a distorted octahedral arrangement of ligands with nitrogen of the F-pyridine ligand trans to the oxygen atom.[49] The XeF_2 adducts of $MoOF_4$ and WOF_4 were explored by ^{129}Xe and ^{19}F NMR spectroscopy.[20,50] The relative fluoride-acceptor strengths of WOF_4 and $MoOF_4$ were deduced from ^{129}Xe and ^{19}F chemical shifts indicating WOF_4 to be a stronger fluoride acceptor than $MoOF_4$ toward XeF_2 and presumably other fluoride donors.[20]

Table 1.3.1 ^{19}F NMR Spectroscopic Data of Tungsten and Molybdenum Oxide Fluorides

Compound or Complex	δ (ppm)[a]	$^2J(^{19}F\text{-}^{19}F)$ (Hz)	$^1J(^{183}W\text{-}^{19}F)$ (Hz)	Solvent[b]	Multiplicity	Ref.
WOF_4	68.5			HF/CH_3CN	Singlet	35
WOF_4	65.2		69	PC	Singlet	31
WOF_4	61.9			HF	Singlet	31
WOF_5^-	53.7	55	72	HF/CH_3CN	Doublet	35
	-104.0				Quintet	
$[NO][WOF_5]$[c]	54.4		84	HF	Singlet	31
$W_2O_2F_9^-$	62.6	59	72	HF/CH_3CN	Doublet	35
	-146.5				Nonet	
$MoOF_4$	142.7			HF	Singlet	31
$MoOF_4$	145.9			PC	Singlet	31
$[NO][MoOF_5]$[c]	134.5			HF	Singlet	31

[a] All chemical shifts referenced to $CFCl_3$ [b] Propylene Carbonate, $C_4H_6O_3$ (PC) [c] Exists in equilibrium with $M_2O_2F_9^-$ (M = Mo, W) in HF solvent.

1.4 Tungsten and Molybdenum Sulfide Fluorides

Among all transition-metal sulfide fluorides, WSF_4 has attracted the most attention. The first report of WSF_4 described the ^{19}F NMR spectroscopic characterization of the reaction between $WSCl_4$ and HF in CH_3CN.[51,52] It was noticed that with time the ^{19}F NMR resonance attributed to WSF_5^- increased in intensity and others would decrease.[52] The substitution of chlorine atoms with fluorine atoms was said to take place

at a very high rate once HF was added. It was also noted that in contrast to the oxide fluorides the $^{2}J(^{19}F\text{-}^{19}F)$ coupling constant increases with an increasing number of fluorine atoms. Alternatively, chlorine-fluorine substitution could be accomplished using XeF_2 according to Equation 1.4.3; the reaction between XeF_2 and $WSCl_4$ in CH_3CN solvent was described as beginning at ca. 0 °C with a colour change from dark red to pale orange. The reaction products were studied by ^{19}F NMR spectroscopy. The ^{19}F NMR spectrum contained eight signals between 90 and -160 ppm, which were dominated by a singlet attributed to WSF_4 at 84.3 ppm. The other signals that could be assigned were assigned to $WSFCl_3$, WSF_2Cl_2, WSF_3Cl.[51]

Solid WSF_4 was isolated from the reactions of WF_6 with B_2S_3 at 260 °C[53] and WF_6 with Sb_2S_3 at 300 °C for 3 hours.[52] Small amounts of WOF_4 were common impurities found in the products generated by all methods evidencing the hydrolytic sensitivity of WSF_4. It was observed by others that the sublimation of WSF_4 occurred readily at 50 °C under vacuum.[53]

$$Sb_2S_3 + 3\ WF_6 \xrightarrow{300\ °C} 3\ WSF_4 + 2\ SbF_3 \qquad 1.4.1$$

$$B_2S_3 + 3\ WF_6 \xrightarrow{260\ °C} 3\ WSF_4 + 2\ BF_3 \qquad 1.4.2$$

$$WSCl_4 + XeF_2 \xrightarrow{CH_3CN} WSF_4 + \text{(other products)} \qquad 1.4.3$$

$$WSCl_4 + HF \xrightarrow{CH_3CN} WSF_4 + \text{(other products)} \qquad 1.4.4$$

The most common sulfide transfer agent used for producing WSF_4 and other transition-metal thiohalides has been Sb_2S_3 as it is commercially available (Equation 1.4.1). Yellow and pale brown crystals were isolated from the cooler part of the reactor after the high-temperature reaction of WF_6 with Sb_2S_3. When ground, both types of crystals appeared pale yellow and gave exactly the same vibrational data. Tungsten sulfide tetrafluoride was characterized by infrared spectroscopy with stretching bands for W=S at 577 cm^{-1}, terminal W-F at 699, 673, and 634 cm^{-1}, and bridging W-F at 534 and 514 cm^{-1}. One Raman band for the W=S stretching mode was observed at 580 cm^{-1}.[52]

In a solution synthesis, WSF_4 was synthesized at ambient temperature in the reaction of $((CH_3)_3Si)_2S$ with WF_6 in CH_3CN. The products contained WSF_4 as shown by a singlet at 86.2 ppm with ^{183}W-satellites showing $^{1}J(^{19}F\text{-}^{183}W)$ coupling of 33.4 Hz in

the ^{19}F NMR spectrum. Banger *et al.* tried various solvents and temperatures and indicated that reactions always generated a brown insoluble byproduct, suggested to be WS_3 (Equation 1.4.6). Extended X-ray absorption fine structure (EXAFS) studies were conducted on *ca.* 0.05 M solutions of WSF_4 in CH_3CN. The EXAFS spectrum exhibited a single broad peak at *ca.* 200 pm, and weaker features at *ca.* 290 and 360 pm. The broad band at 200 pm was attributed to both the four tungsten-fluorine and one tungsten-sulfur bond. The distances of 290 and 360 pm were too long to correspond to tungsten-fluorine bridges, therefore, it was determined that WSF_4 was monomeric in CH_3CN solution, presumably forming the $WSF_4 \cdot CH_3CN$ adduct.[54]

$$WF_6 + ((CH_3)_3Si)_2S \xrightarrow{CH_3CN} WSF_4 + 2\ (CH_3)_3SiF \qquad 1.4.5$$

$$3\ WSF_4 \xrightarrow{CH_3CN} WS_3 + 2\ WF_6 \qquad 1.4.6$$

Attempts at generating WS_2F_2 by increasing the ratio of $((CH_3)_3Si)_2S$ to WF_6 were unsuccessful resulting in greater amounts of a brown solid.[54]

The fluorine-bridged structure of solid WSF_4, which was suggested by the infrared bands at 534 and 514 cm^{-1} [52] was confirmed by single crystal X-ray diffraction.[55] This is in line with studies of other tungsten sulfide halides where single-crystal X-ray diffraction studies of the chloride and bromide analogues have shown square pyramidal molecules bridged asymmetrically via the halide to form dimers.[56]

Electron diffraction data were recorded on WSF_4 in the gas phase confirming the square pyramidal geometry around tungsten in the monomer. The square pyramidal structure is consistent with all WSX_4 (X = F, Cl, Br) in the gas phase. It is interesting to note that W-F bond lengths for WSF_4 and WOF_4 were the same, a result consistent with the chloride analogues (Table 1.4.1). This result would indicate that W-F stretching bands of oxygen and sulfur analogues should be very similar.[53]

Table 1.4.1 Bond Lengths of Various Tungsten Sulfide and Oxide Halides Using Different Methods

		Bond Lengths, pm		
Compound	Bond	Electron Diffraction[53]	Crystal Structure	EXAFS[54]
WOF_4	W=O	166.6(7)	165[26]	168.6(3)
	W-F	184.7(2)	184[26]	185.2(2)
WSF_4	W=S	210.4(7)	207[55]	202.6(8)
	W-F	184.7(3)	187[55]	186.3(3)
$WOCl_4$	W=O	168.5(15)	181[56]	169.1(3)
	W-Cl	228.0(3)	228[56]	230.3(1)
$WSCl_4$	W=S	208.6(6)	209.8[56-58]	NA
	W-Cl	227.7(3)	229.9(11)[56-58]	NA

Table 1.4.2 ^{19}F NMR Chemical Shifts and Coupling Constants of Tungsten Sulfide Fluorides

Material	δ (^{19}F) [a] (ppm)	$^{2}J(^{19}F\text{-}^{19}F)$ (Hz)	$^{1}J(^{183}W\text{-}^{19}F)$ (Hz)	**Solvent**	**Ref.**
WSF_4	85.1 (s)		37 ± 2	CH_3CN	[52]
WOF_4	66.9 (s)			CH_3CN	[52]
WF_6	169.9 (s)			CH_3CN	[52]
$W_2S_2F_9^-$	83.7 (d) -159.3 (n)	70 ± 2		CH_3CN	[51,52]
WSF_5^-	80 (d) -141.2 (qn)	72 ± 2	32	CH_3CN	[52]

[a] Abbreviations denote singlet (s), doublet (d), triplet (t), quartet (q), and quintet (qn).

The Lewis-acid/base character of the tungsten oxide fluorides has been studied extensively, while there have been relatively few studies performed on WSF_4. The Lewis-acid/base properties of WSF_4 are of interest since it remains to be seen what the effect of replacing the oxygen ligand with heavier less electronegative sulfur will have. The $WSF_4 \cdot CH_3CN$ adduct was studied, showcasing the Lewis-acid behaviour of WSF_4. The $WSF_4 \cdot SbF_5$ adduct has been suggested by Holloway, but the adduct was not characterized.[55]

Molybdenum sulfide trifluoride, $MoSF_3$, was reportedly generated by reduction of SF_6 with a molybdenum metal filament between 600 and 800 °C.[59] A liquid film formed on the walls of the reactor at 50 °C that upon cooling to room temperature formed orange crystals of $MoSF_3$. A melting temperature of 85.6 °C was reported and the solid was characterized by powder X-ray diffraction and infrared spectroscopy. The infrared spectrum contained broad signals, 490 - 525 cm^{-1} and 660 - 690 cm^{-1}, attributed to Mo-$F_{bridging}$ and Mo-$F_{terminal}$ bond stretches, respectively.[59]

Holloway and Puddick claimed the synthesis of $MoSF_4$ in 1979.[60] An amber product was produced in reaction between Sb_2S_3 and MoF_6 at 275 °C for six hours (Equation 1.4.7). The product mixture reportedly contained the starting reagents MoF_6 and Sb_2S_3 along with reaction side products MoF_5 and SbF_3, which were removed by sublimation at 40 °C and 130 °C, respectively. The amber-coloured solid $MoSF_4$ was isolated in unspecified amounts. The product $MoSF_4$ was reportedly stable for long periods under vacuum at ambient temperature. X-ray powder diffraction studies were performed on $MoSF_4$ that indicated its structure differed from that of WSF_4. Mass spectrometry of $MoSF_4$ showed a peak corresponding to $MoSF_4^+$ and a much larger peak corresponding to $MoSF_3^+$. Infrared spectroscopy of $MoSF_4$ showed strong bands at 690, 670, and 633 cm^{-1} attributed to terminal Mo-F stretches and bands at 500 and 458 cm^{-1} which were attributed to stretches of bridging fluorides. A band at 564 cm^{-1} attributed to Mo=S stretching was also identified.[60]

$$3\ MoF_6 + Sb_2S_3 \xrightarrow[6\ h]{275\ ^\circ C} 3\ MoSF_4 + 2\ SbF_3 \qquad 1.4.7$$

The known tungsten and molybdenum sulfide fluorides along with the techniques used to study their structures are listed in Table 1.4.3.

Table 1.4.3 Tungsten and Molybdenum Sulfide Fluorides and Their Methods of Structural Characterization

	Sulfide fluoride	Characterization
Mo(V)	$MoSF_3$	powder X-ray diffraction[59] infrared spectroscopy[59]
Mo(VI)	$MoSF_4$	infrared spectroscopy[60] mass spectrometry[60]
W(VI)	WSF_4	infrared spectroscopy[52] Raman spectroscopy[52] matrix-isolated infrared spectroscopy[61] UV/VIS spectroscopy[61] NMR spectroscopy[54] single crystal X-ray diffraction[55] gas-phase electron diffraction[53] EXAFS[54]
	WSF_5^-	NMR spectroscopy[51,52] infrared spectroscopy[62] Raman spectroscopy[62] single crystal X-ray diffraction[62]
	$W_2S_2F_9^-$	NMR spectroscopy[51,52]

The disproportionation and thermal decomposition of $MoSF_3$ and $MoSF_4$ were studied by mass spectral analysis. Studies conducted on $MoSF_3$ vapour at 308 K suggest that $MoSF_3$ is susceptible to disproportionation and decomposition as it volatizes forming $MoSF_4$, MoF_5 and S_8 molecules that were found in the gas phase. The heat of removal of sulfide from molybdenum sulfides was shown to be much lower than for corresponding tungsten sulfide fluorides, which may help explain the relative instability of $MoSF_4$, compared to WSF_4.[63]

The heats of formation for $MoSF_3$ and $MoSF_4$ were calculated for the gas-phase molecules. Bond lengths for $MoSF_3$ and $MoSF_4$ were also estimated at 207 pm for Mo=S and 184 pm for Mo-F bonds.[63]

Due to their instability and lack of a method for bulk production of $MoSF_4$, molybdenum sulfide fluorides have not been studied further and hence have yet to be characterized by NMR and Raman spectroscopy.

1.5 Goal of Present Research

The main hurdle to further studies of tungsten and molybdenum sulfide fluorides is the inability to easily produce them in high purity on a preparative scale. It is hoped that novel, ambient temperature and pressure preparative methods can be developed that will make both, WSF_4 and $MoSF_4$, readily accessible. It is also hoped that use of new trimethylsilanethiolate salts as sulfide transfer agents will allow for the facile generation of WSF_5^- and $MoSF_5^-$ anions directly from WF_6 and MoF_6, respectively. It is the main goal of this research to shed light on the reactivity of these elusive and highly reactive species.

References

(1) O'Donnell, T. A.; Stewart, D. F. *Inorg. Chem.* **1966**, *5*, 1434.

(2) Edwards, A. J. *J. Chem. Soc. A.* **1969**, 909.

(3) Schroeder, J.; Grewe, F. J. *Chem. Ber.* **1970**, *103*, 1536.

(4) Quellette, T. J.; Ratcliffe, C. T.; Sharp, D. W. A. *J. Chem. Soc.* **1969**, 2351.

(5) Gusarov, A. V.; Pervov, V. S.; Gotkis, I. S.; Klyuev, L. I.; Butskii, V. D. *Dokl. Akad. Nauk SSSR* **1974**, *216*, 1296.

(6) Falconer, W. E.; Jones, G. R.; Sunder, W. A.; Haigh, I.; Peacock, R. D. *J. Inorg. Nucl. Chem.* **1973**, *35*, 751.

(7) Priest, H. F.; Schumb, W. C. *J. Amer. Chem. Soc.* **1948**, *70*, 3378.

(8) Edwards, A. J.; Peacock, R. D.; Small, R. W. H. *J. Chem. Soc.* **1962**, 4486.

(9) Peacock, R. D. *Proc. Chem. Soc.* **1957**, 59.

(10) Emeleus, H. J.; Gutmann, V. *J. Chem. Soc.* **1949**, 2979.

(11) LaValle, D. E.; Steele, R. M.; Wilkinson, M. K.; Yakel, H. L. *J. Am. Chem. Soc.* **1960**, *82*, 2433.

(12) Moock, K. H.; Macgregor, S. A.; Heath, G. A.; Derrick, S.; Boeré, R. T. *J. Chem. Soc., Dalton Trans.* **1996**, 2067.

(13) Giese, S.; Seppelt, K. *Angew. Chem., Int. Ed. Engl.* **1994**, *33*, 461.

(14) Prescott, A.; Sharp, D. W. A.; Winfield, J. M. *J. Chem. Soc., Dalton Trans.* **1975**, 934.

(15) Hargreaves, G. B.; Peacock, R. D. *J. Chem. Soc. A.* **1958**, 2170-2175.

(16) Adam, S.; Ellern, A.; Seppelt, K. *Chem. Eur. J.* **1996**, *2*, 398.

(17) Ruff, O.; Eisner, F.; Heller, W. Z. *Anorg. Allg. Chem.* **1907**, 52, 256-269.

(18) Levason, W.; Narayanaswamy, R.; Ogden, J. S.; Rest, A. J.; Turff, J. W. *J. Chem. Soc., Dalton Trans.* **1981**, 2501.

(19) Cady, G. H.; Hargreaves, G. B. *J. Chem. Soc. A.* **1961**, 1568.

(20) Holloway, J. H.; Schrobilgen, G. J. *Inorg. Chem.* **1980**, *19*, 2632.

(21) Green, P. J.; Gard, G. L. *Inorg. Chem.* **1977**, *16*, 1243.

(22) Paine, R. T.; McDowell, R. S. *Inorg. Chem.* **1974**, *13*, 2366

(23) Wilson, W. W.; Christe, K. O. *Inorg. Synth.* **1986**, *24*, 37.

(24) Beattie, I. R.; Reynolds, D. J. *J. Chem. Soc., Chem. Commun.* **1968**, 1531.

(25) Asprey, L. B.; Ryan, R. R.; Fukushima, E. *Inorg. Chem.* **1972**, *11*, 3122.

(26) Edwards, A. J.; Jones, G. R. *J. Chem. Soc. A.* **1968**, 2074.

(27) Edwards, A. J.; Jones, G. R.; Steventon, B. R. *J. Chem. Soc., Chem. Commun.* **1967**, 462.

(28) Beattie, I. R.; Livingston, K. M. S.; Reynolds, D. J.; Ozin, G. A. *J. Chem. Soc. A.* **1970**, 1210.

(29) Bennett, M. J.; Haas, T. E.; Purdham, J. T. *Inorg. Chem.* **1972**, *11*, 207.

(30) Alexander, L. E.; Beattie, I. R.; Bukovsky, A.; Jones, P. J.; Marsden, J.; Van Schalkwyk, G. J. *J. Chem. Soc., Dalton Trans.* **1974**, 81

(31) Bougon, R.; Huy, T. B.; Charpin, P. *Inorg. Chem.* **1975**, *14*, 1822

(32) Atherton, M. J.; Holloway, J. H. *J. Chem. Soc., Chem. Commun.* **1978**, 254.

(33) Brisdon, A. K.; Holloway, J. H.; Hope, E. G. *J. Fluorine Chem.* **1998**, *89*, 35.

(34) Petrov, V. M.; Giricheva, N. I.; Rakov, E. G.; Girichev, G. V.; Melnichenko, E. I. *J. Struct. Chem.* **1993**, *34*, 372.

(35) Buslaev, Y. A.; Kokunov, Y. V.; Bochkareva, V. A. *J. Struct. Chem.* **1972**, *13*, 570.

(36) Hoskins, B. F.; Linden, A.; O'Donnell, T. A. *Inorg. Chem.* **1987**, *26*, 2223.

(37) Selig, H.; Sunder, W. A.; Schilling, F. C.; Falconer, W. E. *J. Fluorine Chem.* **1978**, *11*, 629

(38) Wilson, W. W.; Christe, K. O. *Inorg. Chem.* **1981**, *20*, 4139.

(39) Beuter, A.; Sawodny, W. *Z. Anorg. Allg. Chem.* **1976**, *427*, 37.

(40) Ralston, K.; Musil, F. J. Goodyear Atomic Corp., 1960.

(41) Chaminade, J. P.; Moutou, J. M.; Villeneuve, G.; Couzi, M.; Pouchard, M.; Hagenmuller, P. *J. Solid State Chem.* **1986**, *65*, 27.

(42) Ruff, O.; Eisner, F. *Ber.* **1907**, *40*, 2931.

(43) Edwards, A. J.; Steventon, B. R. *J. Chem. Soc. A.* **1968**, 2503.

(44) Buslaev, Y. A.; Kokunov, Y. V.; Bochkareva, V. A.; Shustorovich, E. M. *J. Struct. Chem.* **1972**, *13*, 491.

(45) Bartlett, N.; Robinson, P. L. *J. Chem. Soc. A.* **1961**, 3549-3550.

(46) Arnaudet, L.; Bougon, R.; Ban, B.; Charpin, P.; Isabey, J.; Lance, M.; Nierlich, M.; Vigner, J. *Can. J. Chem.* **1990**, *68*, 507.

(47) Arnaudet, L.; Bougon, R.; Ban, B.; Charpin, P.; Isabey, J.; Lance, M.; Nierlich, M.; Vigner, J. *J. Inorg. Chem* **1989**, *28*, 257.

(48) Arnaudet, L.; Bougon, R.; Buu, B. *J. Fluorine Chem.* **1995**, *74*, 223.

(49) Arnaudet, L.; Bougon, R.; Buu, B.; Lance, M.; Nierlich, M.; Vigner, J. *Inorg. Chem.* **1993**, *32*, 1142.

(50) Schrobilgen, G. J.; Holloway, J. H.; Granger, P.; Brevard, C. *Inorg. Chem.* **1978**, *17*, 980

(51) Buslaev, Y. A.; Kokynov, Y. B.; Chubar, Y. D. *Proc. Acad. Sci.* **1973**, *213*, 912.

(52) Atherton, M. J.; Holloway, J. H. *J. Chem. Soc., Chem. Commun.* **1977**, 424.

(53) Rice, D. A.; Hagen, K.; Hedberg, L.; Hedberg, K.; Staunton, G. M.; Holloway, J. H. *Inorg. Chem.* **1984** *23* 1826

(54) Banger, K. K.; Blackman, C. S.; Brisdon, A. K. *J. Chem. Soc., Dalton Trans.* **1996**, 2975

(55) Holloway, J. H.; Kaucic, V.; Russell, D. R. *J. Chem. Soc., Chem. Commun.* **1983**, 1079.

(56) Drew, M. G. B.; Mandyczewsky, R. *J. Chem. Soc. A*. **1970**, 2815.

(57) Atherton, M. J.; Holloway, J. H. *Adv. Inorg. Chem. Radiochem.* **1979**, *22*, 171.

(58) Rice, D. A. *Coord. Chem. Rev.* **1978**, *25*, 199.

(59) Pervov, V. S.; Butskii, V. D.; Podzolko, L. G. *Russ. J. Inorg. Chem.* **1978**, *23*, 819.

(60) Holloway, J. H.; Puddick, D. C. *Inorg. Nucl. Chem. Letters* **1979**, *15*, 85.

(61) Jones, P. J.; Levason, W.; Ogden, J. S.; Turff, J. W. *J. Chem. Soc., Dalton Trans.* **1983**, 2625.

(62) Hilbers, M.; Lage, M.; Mattes, R. *Inorg. Chim. Acta* **1992**, *201*, 1.

(63) Malkerova, I. P.; Alikhanyan, A. S.; Gorgoraki, V. I. *Russ. J. Inorg. Chem.* **1980**, *25*, 1742.

Chapter 2
Experimental Section

2.1 Standard Techniques

The compounds used in the course of this work are all moisture and air-sensitive; consequently all manipulations were carried out under rigorously anhydrous inert-atmosphere conditions. Glass and metal vacuum line systems, a dry-nitrogen-filled glove bag, and the oxygen- and moisture-free atmosphere of a Vacuum Atmospheres (Omni Lab) drybox were used. Preparative work inside the dry box requiring low temperatures was carried out in a metal Dewar containing 4.5-mm copper-plated spheres (air rifle BB's) which had been previously cooled in a cryowell by immersion of the cryowell in liquid nitrogen for several hours.

Volatile materials that were non-corrosive towards glass in the absence of water were manipulated on a Pyrex-glass vacuum line equipped with grease-free 6-mm J. Young glass stopcocks equipped with PTFE barrels (Figure 2.1.1). Pressures inside the manifold were monitored using a Heise gauge (model CC, 0–1000 mmHg, beryllium/copper Bourdon tube, Dresser Instruments). The final vacuum was monitored by a Varian thermocouple gauge connected to the vacuum line between the liquid-nitrogen trap and the vacuum pump.

Volatile materials, which attacked glass, were handled on a metal vacuum line constructed from nickel and 316 stainless steel, and equipped with 316 stainless steel valves and fittings (Autoclave Engineers Inc.), PTFE, and FEP (Figure 2.1.2) Pressures were measured at ambient temperature using Baratron capacitance manometers (MKS, Type 626A, effective range 0 – 1000 mmHg) having inert wetted surfaces constructed of Inconel, in conjunction with a digital readout.

Vacuum on the glass (ca. 10^{-5} Torr) and metal lines (ca. 10^{-4} Torr) was attained by the use of Edwards two stage direct drive RV8 Edwards vacuum pumps. Two vacuum pumps were used on the metal vacuum line; one, a roughing pump, was connected to a fluoride/fluorine trap consisting of a stainless-steel cylinder (75-cm length, 17-cm outer diameter) packed with soda lime absorbent (EMD, 4 mesh). Removal and disposal of volatile reactive fluorinated compounds was accomplished by pumping through, and

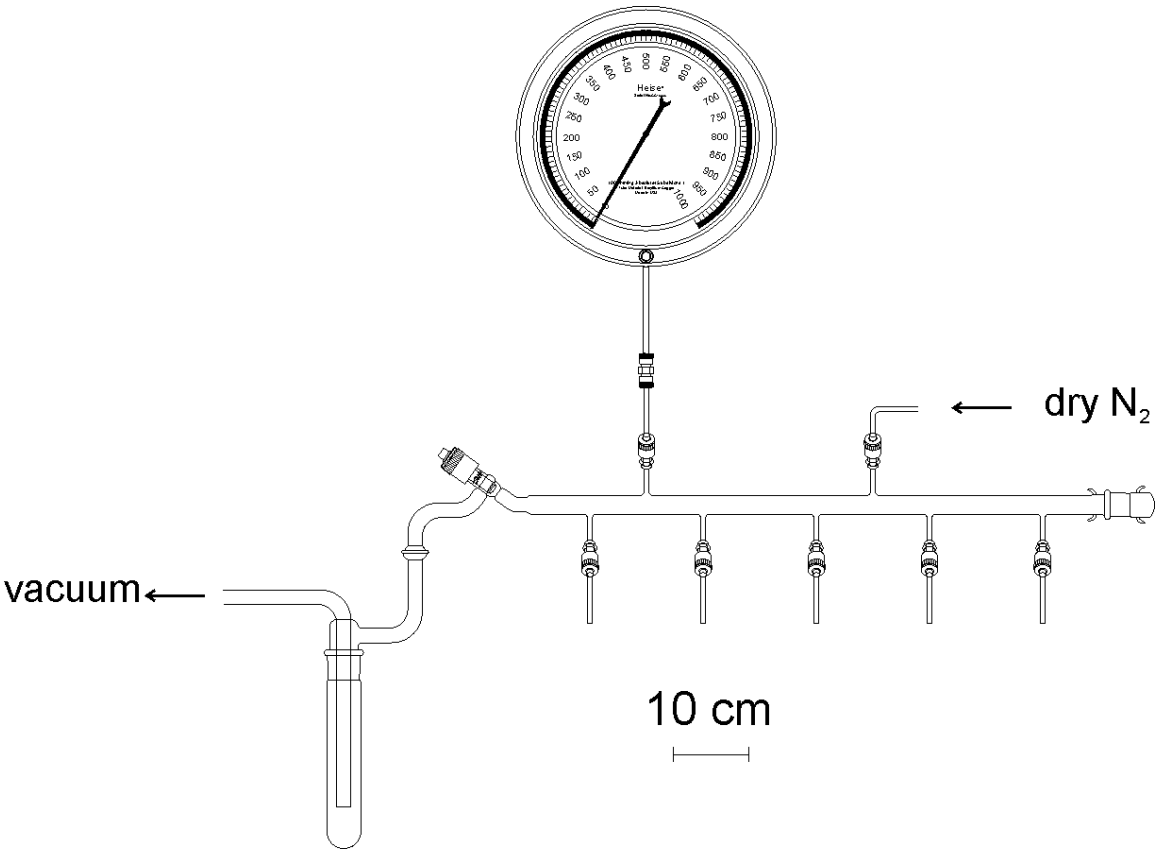

Figure 2.1 1 Glass vacuum line system equipped with J. Young PTFE/glass stopcocks and a Heise gauge.

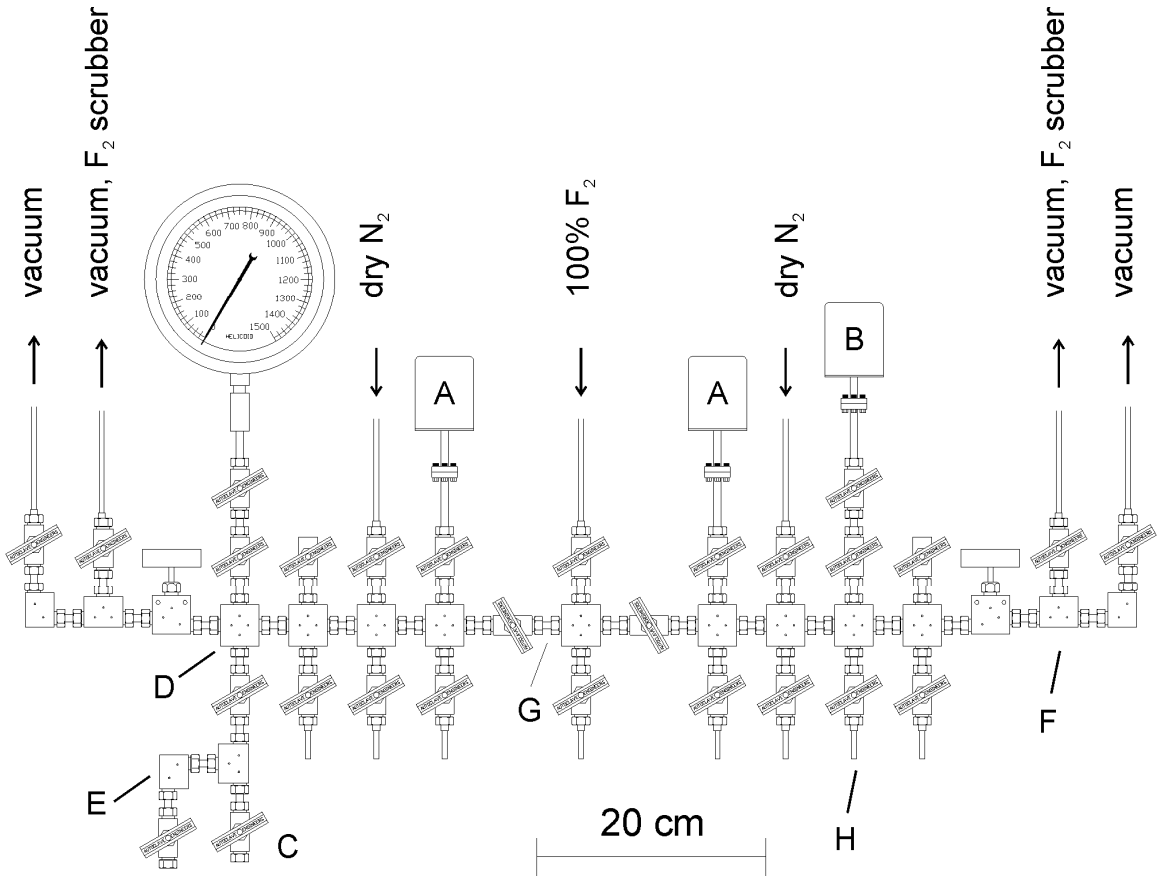

Figure 2.1.2 Metal vacuum system; (A) MKS type 626A capacitance manometer (0-1000 Torr), (B) MKS Model PDR-5B pressure transducers (0-10 Torr), (C) 3/8-in. stainless-steel high-pressure valves (Autoclave Engineers, 30VM6071), (D) 316 stainless-steel cross (Autoclave Engineers, CX6666), (E) 316 stainless-steel L-piece (Autoclave Engineers, CL6600), (F) 316 stainless steel T-piece (Autoclave engineers, CT6660), (G) $^{3}/_{8}$-in o.d., $^{1}/_{8}$-in. i.d. nickel connectors, (H) $^{1}/_{8}$-in o.d., $^{1}/_{8}$-in. i.d. nickel tube.

entrapment on a bed of soda lime followed by trapping of the volatile reaction products, CO_2 and H_2O, in a glass liquid nitrogen trap. The second vacuum pump provided the high vacuum source for the manifold and was cold trapped with a glass liquid nitrogen trap. All preparative work involving WF_6, MoF_6, and anhydrous HF was carried out in ¾-in, ¼-in., or 4-mm o.d. FEP tubes which were heat-sealed at one end and connected through 45° flares to Kel-F or 37 ° flares to stainless-steel valves (Swagelok SS-ORM2 and SS-IRF2 valves). The FEP sample tubes were dried under dynamic vacuum overnight on a glass vacuum line prior to transfer onto the metal line where they were checked for leaks, passivated with F_2 at 1 atm for 12 h, re-evacuated and then back filled with dry N_2 before transferring to the dry box. Pyrex-glass reaction vessels were dried under dynamic vacuum overnight periodically flamed out by use of a Bunsen burner.

Nuclear magnetic resonance (NMR) spectra were recorded on samples prepared in 4-mm o.d. FEP tubes. The NMR tubing had one end heat sealed by pushing the end of the FEP tube into the hot end of a thin-walled 5-mm o.d. NMR tube and the other end was fused to a ¼-in. o.d. thick-walled FEP tubing which was heat-flared for direct attachment to a Kel-F valve (Figure 2.1.3(a)). The 4-mm sample tubes used for NMR were heat sealed under dynamic vacuum with a heat gun while the sample was frozen at –196 °C. All heat-sealed samples were stored submerged in liquid nitrogen (-196 °C) until they could be spectroscopically characterized. For NMR measurements, the 4-mm FEP tubes were inserted into standard 5-mm precision NMR tubes before insertion into the NMR probe.

Raman spectra of solids that are stable at room temperature and which do not attack glass were recorded on samples in Pyrex-glass melting point capillaries. Before use, the melting point capillaries were heated under dynamic vacuum for 24 h at 200 °C and then stored in the drybox where they were loaded with the appropriate materials. The end of the loaded melting point capillary was temporarily sealed with Kel-F grease before removal from the drybox. The capillaries were then immediately heat-sealed with an oxygen-natural gas torch.

Vessels were attached to vacuum lines through thick-walled FEP tubing and ¼-in. PTFE Swagelok connectors or ¼-in. stainless-steel Ultra-Torr connectors fitted with viton rubber O-rings.

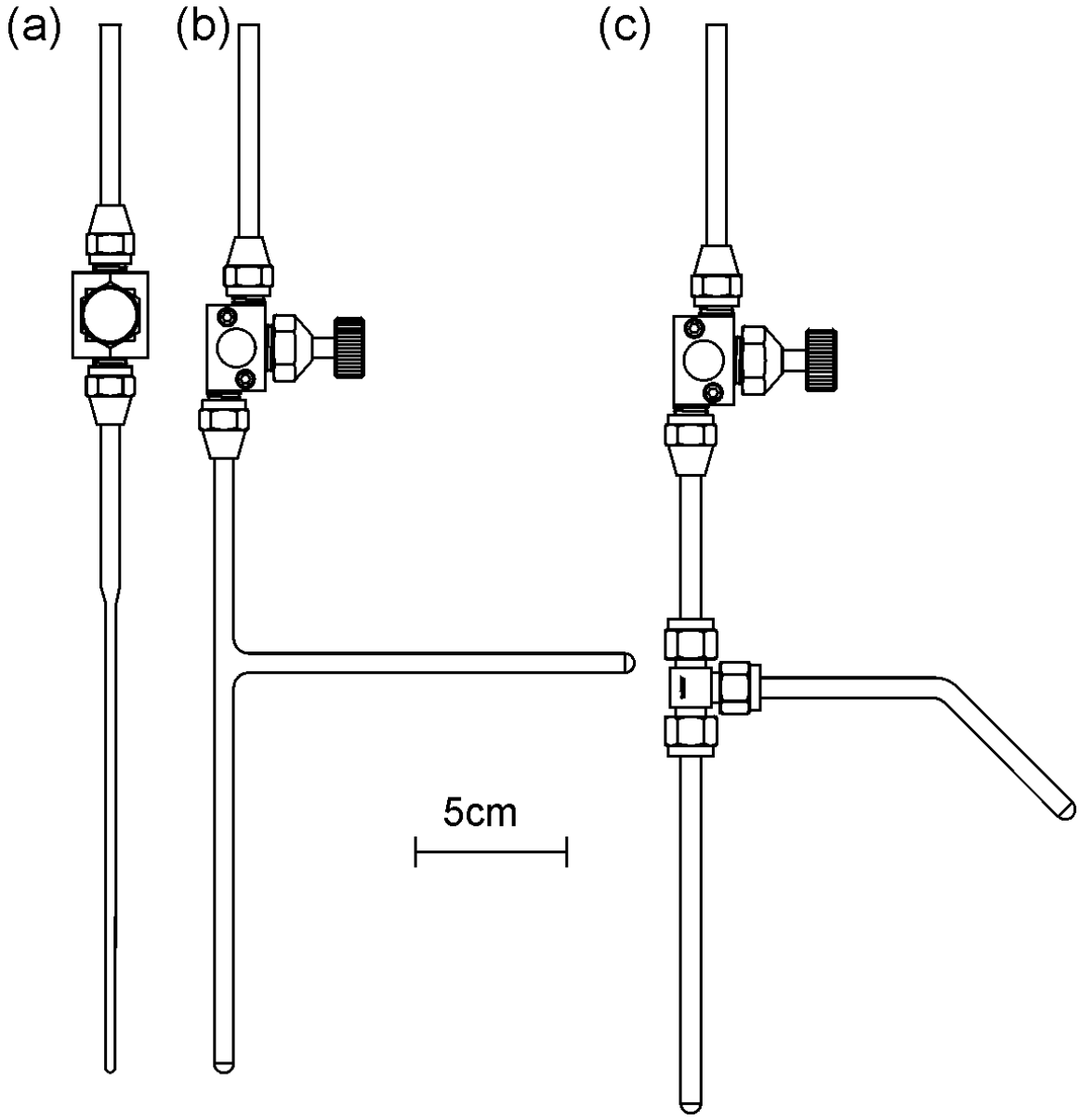

Figure 2.1.3 Common FEP reactors used to conduct experiments: (a) 4-mm o.d. reaction vessel equipped with a Kel-F valve. (b) ¼-in. o.d. FEP T-reactor equipped with Kel-F valve. (c) ¼-in. o.d. FEP T-reactor equipped with a stainless-steel Swagelok-T and a Kel-F valve.

2.2 Preparation and Purification of Starting Materials

2.2.1 Purification of HF, CH_3CN, SO_2ClF, C_5H_5N, THF, Solvents and $(Me_3Si)_2S$

Anhydrous hydrogen fluoride (Air Products) was stored at room temperature in a nickel storage vessel equipped with a monel (Autoclave Engineers) valve. Hydrogen fluoride was dried over potassium hexafluoronickelate(VI) in a ¾-in. o.d. FEP vessel (Figure 2.2.1), equipped with a stainless steel valve prior to transfer to reaction vessels by vacuum distillation on the metal vacuum line through connections constructed of FEP.

Acetonitrile (Sigma-Aldrich) was purified according to the literature procedure [1] and was transferred under vacuum using a glass vacuum line and glass Y-piece.

Pyridine (Sigma-Aldrich, 99.8%) was added to CaH_2 in a glass storage bulb inside the glove bag. Then the liquid was vacuum distilled from the original storage bulb and stored over CaH_2 in a glass storage bulb equipped with a Teflon J. Young stopcock.

Tetrahydrofuran was obtained from a dry solvent system and was refluxed over sodium metal with benzophenone indicator and subsequently distilled into a glass storage vessel equipped with PTFE J. Young stopcock over sodium metal.

Hexamethyldisilathiane, $(Me_3Si)_2S$, (Fluka, purum) was purified by vacuum distillation at room temperature through a glass Y-piece into a glass storage vessel equipped with a Teflon J. Young stopcock.

2.2.2 Purification of MoF_6, WF_6, SbF_3, and SbF_5

Molybdenum hexafluoride (Elf Atochem) and WF_6 (Elf Atochem) were used as provided and were transferred into reaction vessels by vacuum distillation through passivated stainless-steel and fluoroplastic connections.

Antimony trifluoride, SbF_3 (Ozark Fluorine Specialties) was sublimed under vacuum and transferred into a drybox.

Antimony pentafluoride, SbF_5 (Ozark-Mahoning Co) was purified by vacuum distillation in a Teflon and glass apparatus connected with PTFE Swagelok unions and stored in a glass U-tube equipped with PTFE J. Young stopcocks, which was kept in a dessiccator. Subsequent transfers of SbF_5 were performed through a glass Y-piece with PTFE Swagelok connections.

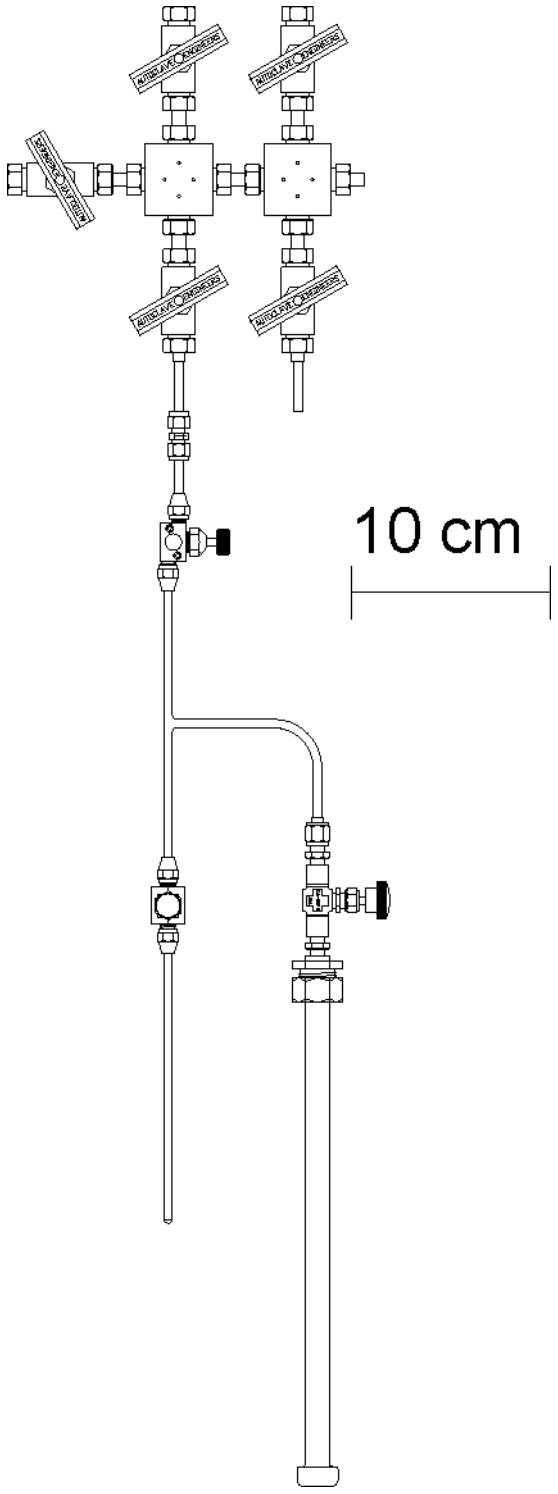

Figure 2.2.1 A ¾-in. o.d. FEP vessel equipped with a stainless steel valve and a FEP T-piece connection for distillation of HF to reactors.

2.2.3 Drying of $[N(CH_3)_4][F]$, CsF, KF, Sb_2S_3, Sb_2S_5

Anhydrous tetramethylammonium fluoride, $[N(CH_3)_4][F]$, was prepared from tetramethylammonium fluoride tetrahydrate (Fluka > 98 %) according to the literature method. [2]

Cesium fluoride, CsF (Sigma-Aldrich, 99.99%) was dried by fusion in a platinum crucible, followed by the transfer of the red hot clinker to the dry box port where it was immediately evacuated. Upon transferring to the dry nitrogen atmosphere of the glove box, the sample was ground to a fine powder and stored in the dry box until use.

Potassium fluoride was dried under dynamic vacuum at temperatures of 160° C for six hours prior to being transferred in the dry box.

Antimony (III) sulfide, Sb_2S_3 (Alpha Aesar, 100%) was ground to a fine powder followed by drying under dynamic vacuum at 160 °C for ca. six hours prior to being brought into the dry box.

Antimony (V) sulfide, (Sigma-Aldrich) was heated to 80°C for 16 h under dynamic vacuum prior to being brought into the dry box.

2.3 Synthesis of Silanethiolate Salts

2.3.1 Preparation of $[N(CH_3)_4][SSi(CH_3)_3]$

Inside the dry box, 0.273 g (2.93 mmol) of $N(CH_3)_4F$ was transferred into a glass reactor equipped with J. Young Teflon stopcock and a PTFE-coated stirring bar. The sealed reactor was connected to the glass vacuum line where 4.490 g of CH_3CN and 0.530 g (2.96 mmol) of $((CH_3)_3Si)_2S$ were vacuum distilled on top of the powder. The CH_3CN solvent was allowed to melt at -35 °C using an ethanol bath, followed by stirring of the reaction mixture. The clear colourless solution turned milky white for a few moments before a white solid settled from the reaction mixture. The volatiles were removed under dynamic vacuum at -35 °C yielding a white solid aggregate. The solid was further heated to 50 °C under dynamic vacuum to completely remove CH_3CN solvent. Inside the dry box, the aggregate was ground and 0.458 g (2.55 mmol) $[N(CH_3)_4][SSi(CH_3)_3]$ was collected. Typical yields for the reaction were 87.1 %.

2.3.2 Preparation of [K(18-crown-6)][SSi(CH$_3$)$_3$]

Inside the dry box, 0.042 g (0.72 mmol) of KF and 1.950 g (0.73 mmol) of 18-crown-6 were transferred into a glass reactor equipped with a J. Young. PTFE/glass stopcock and a PTFE-coated stiring bar. The sealed reactor was connected to the glass vacuum line where 4.883 g CH_3CN was vacuum distilled on top of the powders. The reaction vessel was warmed to -38 °C and the reaction mixture was stirred. The solution was cooled to -196 °C and 0.192 g (1.08 mmol) of $((CH_3)_3Si)_2S$ was vacuum distilled on top of the frozen solution. The solution was allowed to warm to -38 °C using a cold-ethanol bath followed by stirring. The clear colourless solution turned milky white for a few moments before a white solid settled from the reaction mixture. The volatiles were removed under dynamic vacuum at -40 °C leaving white solid on the sides of the reactor. Inside the drybox, 0.259 g (0.634 mmol) of solid [K(18-crown-6)][SSi(CH$_3$)$_3$] was collected and stored inside the dry box for further analysis and future use. Typical yields for reaction were 87.7 %.

2.3.3 Preparation of Cs[SSi(CH$_3$)$_3$]

Inside the dry box, 0.238 g (1.57 mmol) CsF powder was transferred to one side of a glass H-reactor equipped with J. Young Teflon stopcocks (Figure 2.3.1). The sealed reaction vessel was connected to the glass vacuum line where 3.202 g of CH_3CN and 0.376 g (2.11 mmol) of $((CH_3)_3Si)_2S$ were vacuum distilled on top of the powder. The reaction vessel was warmed to 0 °C and agitated using an ultrasonic bath. The solution turned milky white, but significantly less intensely than the reaction with $N(CH_3)_4F$, for several minutes before a white solid settled from the reaction mixture. The volatiles were removed under dynamic vacuum at 0 °C yielding white solid on the sides of the reaction vessel and on the bottom of the reactor indicating solubility in CH_3CN. A further purification step was employed by decanting the CH_3CN to the other side of the H-reactor and washing the solid by vacuum distilling the CH_3CN solvent back to the original side, followed by decantation of the solution until all solid soluble in CH_3CN was transferred. After removal of the solvent, the solid that was soluble in CH_3CN was brought inside the drybox and stored in glass vials in the dry box for further analysis and future use. Typical yields were 71.8 % for the reaction.

2.3.4 Preparation of $K[SSi(CH_3)_3]$

Inside the dry box 0.118g (2.03 mmol) KF powder was transferred to a glass reactor equipped with a J. Young PTFE/glass stopcock. The sealed reaction vessel was taken from the dry box to the glass vacuum line where 3.262 g of CH_3CN and 0.551 g (3.09 mmol) $((CH_3)_3Si)_2S$ were vacuum distilled on top of the powder. The reaction vessel was warmed to room temperature and agitated with sonication for several minutes. The solution turned milky white, but significantly less intensely than the reaction with $N(CH_3)_4F$, before a white solid settled from the reaction mixture. The contents were repeatedly sonicated as KF is insoluble in CH_3CN and decomposition of the solvent from nucleophilic F^- attack was not a concern. The volatiles were removed under dynamic vacuum yielding a white solid. Solid $K[SSi(CH_3)_3]$ (0.189 g, 1.31 mmol) was collected and stored in glass vials in the dry box for further analysis and future use. Typical yield for reaction was 64.5 %.

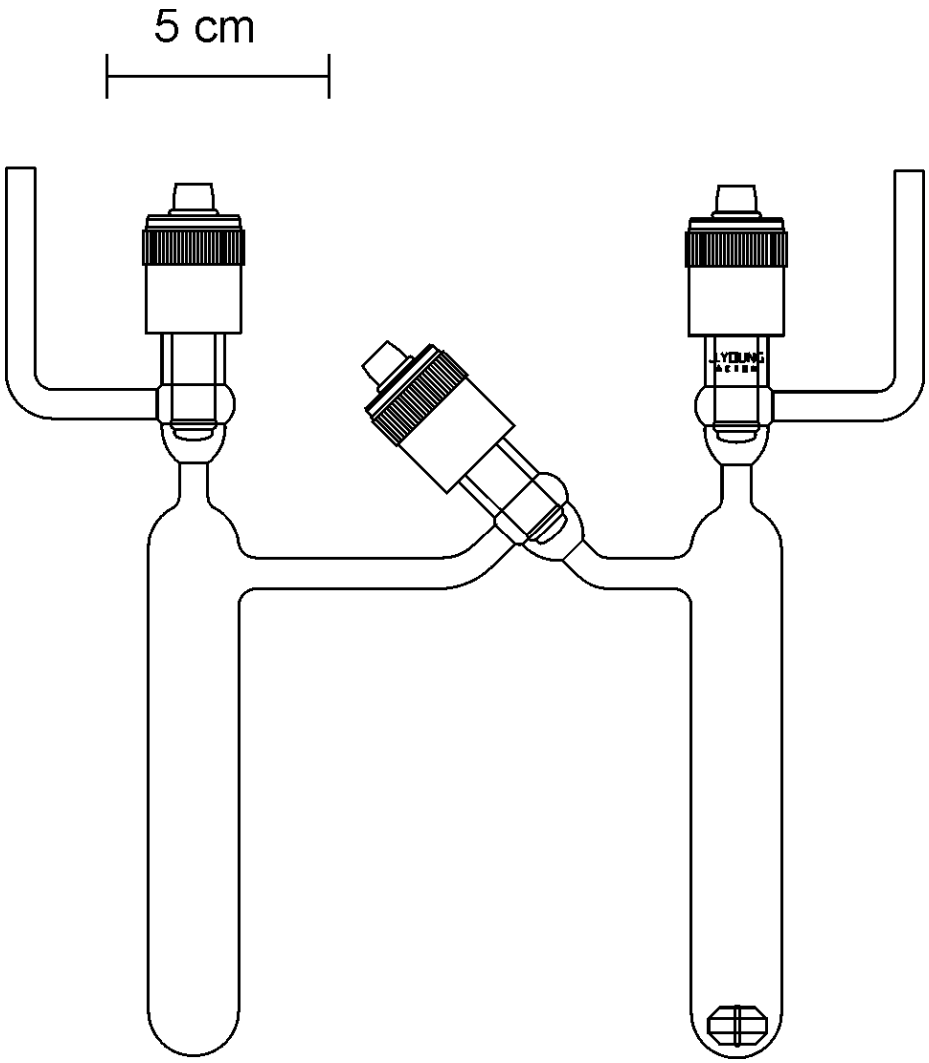

Figure 2.3.1 Glass H-reactor equipped with J. Young PTFE/glass stopcocks and PTFE-coated stir bar.

2.4 Synthesis and Reactions of WSF_4

2.4.1 Synthesis of WSF_4 in HF

Inside the drybox, dried Sb_2S_3 (0.136 g 0.400 mmol) was added to a ¼-in. o.d. thin wall FEP T-reactor equipped with a Kel-F valve (Figure 2.1.3(b)). The reactor was taken from the dry box and 1.76 g of anhydrous HF was vacuum distilled on top of the powder at –196 °C. Tungsten hexafluoride (0.326 g 1.09 mmol) was vacuum transferred on top of the frozen reaction mixture at –196 °C. The reactor was backfilled with dry $N_{2(g)}$ and allowed to warm to room temperature. The reactor mixture was agitated to dissolve frozen WF_6 as the solution warmed to room temperature. The reaction progressed as the solution above the insoluble dark-grey Sb_2S_3 slowly changed from colourless to deep yellow over the course of 16 hours. The reaction mixture was agitated intermittently as the reaction progressed in order to maximize the contact between reactants. The deep yellow solution was decanted over to side arm of FEP T-reactor at which time the solution was cooled to ca. –78 °C. Yellow solid precipitated out of the solution, allowing for colourless HF solvent to be decanted back to original side. The reaction mixture was washed with the HF and the resulting yellow solution was re-decanted to the side-arm of the reaction vessel. The washing procedure was performed 2-3 times. Anhydrous HF was removed under vacuum at –78 °C, over several hours, yielding yellow crystalline material. Pumping was continued for an additional 10 min at room temperature to guarantee complete removal of HF and unreacted WF_6. The amount of recovered WSF_4 was 0.258 g (0.867 mmol) with a yield of 79.3 %. The highest yield obtained using this method was 82 %.

2.4.2 Reaction of WF_6 with H_2S in $CFCl_3$

Approximately 1.8 mL (1.496 g) of $CFCl_3$ was distilled into a ¼-in. o.d. FEP reactor equipped with a Kel-F valve at -196 °C. Hydrogen sulfide (0.043g, 1.3 mmol) was condensed into the reactor at -196 °C. Upon warming to room temperature the solution was clear and colourless. Tungsten hexafluoride (0.228 g, 0.766 mmol) was vacuum distilled into the reactor forming a pale yellow solution. The pale colour of the solution persisted for several hours. Raman spectroscopy of the solution showed strong bands corresponding to WF_6 and H_2S respectively. Both reactants were observed to

coexist in solution at the same time. Above the solution reactions in the gas phase slowly resulted in a red/brown deposit on the sides of the reactor. When the solution was placed in the Raman spectrometer at room temperature the laser light caused the immediate formation of brown solid throughout the solution. At temperatures of -20 °C no brown solid was observed. Volatiles were removed under dynamic vacuum at room temperature yielding a red/brown solid. The order of addition of reagents and amounts always gave the same results. This method was abandoned due to an inability to prevent gas-phase reactions from occurring above the solution level.

2.5 Lewis Acid Chemistry of WSF_4

2.5.1 Reaction of WSF_4 with Pyridine

Inside the dry box, 0.039 g (0.13 mmol) of WSF_4 was transferred to a ¼-in o.d. FEP vessel equipped with a Kel-F valve. On the glass line, 0.566 g (7.15 mmol) of pyridine was vacuum distilled on top of brown WSF_4 powder at -196°C. The powder dissolved completely generating a deep orange solution. Excess C_5H_5N was removed under dynamic vacuum at room temperature yielding 0.051g (0.14 mmol) of dark solid $WSF_4 \cdot C_5H_5N$. The ratio WSF_4 to pyridine was found to be 1:1.1.

Inside the dry box, 0.10 g (0.034 mmol) of WSF_4 was loaded into a 4-mm FEP reactor with Kel-F valve. Pyridine (0.494 g 6.24 mmol) was vacuum transferred to the reactor through a glass Y-piece on the glass vacuum line, generating an orange solution. Approximately 93.1 % of the C_5H_5N was removed at temperatures from –40 to –5 °C over 2 h leaving a intense orange-coloured concentrated solution. Acetonitrile was vacuum transferred into the reaction vessel giving an orange solution. The sample tube was heat-sealed under dynamic vacuum at –196 °C and the sample was stored at -196 °C for analysis by NMR spectroscopy.

2.5.2 Production of $[N(CH_3)_4][WSF_5]$

Inside the dry box, 0.026 g (0.15 mmol) of $[N(CH_3)_4][SSi(CH_3)_3]$ and a small Teflon coated magnetic stir bar were added to a ¾-in. o.d. FEP reactor equipped with a stainless steel valve. Subsequently 6.219 g (86.23 mmol) THF was vacuum distilled onto the solid at -196 °C. The reaction mixture was then stirred at 20 °C to achieve maximum

dissolution of $[N(CH_3)_4][SSi(CH_3)_3]$, which formed a clear colourless solution. White solid was still visible at the bottom of the reaction vessel as not all dissolved. Vacuum distillation of 0.040 g (0.13 mmol) of WF_6 at –196 °C was followed by warming the mixture to –78 °C and stirring for ca. one hour as the solution went from yellow to pink. The solvent THF was removed under dynamic vacuum overnight at –78 °C and then for 30 minutes at room temperature into a FEP U-tube at –196 °C that was connected to the glass vacuum line. The reaction vessel contained 0.060 g of a homogeneous pink coloured powder. The amount of solid recovered corresponded to 0.15 mmol of $[N(CH_3)_4][WSF_5]$ indicating the presence of a small amount of C_4H_8O in the final product. The ^1H NMR spectrum shows a very small peak at 12.39 ppm and a broad feature at *ca.* 4.9 ppm, which likely correspond to carboxylic acids and aliphatic chains, respectively, resulting from the ring-opening step in the polymerization of THF.

2.5.3 Production of $[N(CH_3)_4][WSF_5]$ from WSF_4

Direct combination of 0.0070 g (0.024 mmol) WSF_4 and 0.0023 g (0.024 mmol) of $N(CH_3)_4F$ in CH_3CN resulted in the formation of $[N(CH_3)_4][WSF_5]$ in high purity. The powders were added to a 4-mm o.d. FEP reactor equipped with a Kel-F valve in the dry box. Approximately 0.45 mL of CH_3CN solvent was distilled on top of the solids at -196 °C and the contents were warmed to -35 °C and agitated yielding a bright yellow solution. After the contents were mixed thoroughly, the reactor contents were frozen and heat-sealed under dynamic vacuum. The NMR sample was warmed to room temperature and the sample was studied by ^1H and ^{19}F NMR spectroscopy.

2.6 Preparation of $MoSF_4$

2.6.1 Synthesis of $MoSF_4$

On the glass vacuum line, 5.388 g of $CFCl_3$ was vacuum distilled into a ¼-in o.d. FEP reactor with stainless steel valve containing a small Teflon-coated stir bar. Subsequently, 0.306 g (1.71 mmol) of $((CH_3)_3Si)_2S$ was vacuum distilled on top of the frozen $CFCl_3$ at –196 °C and the resulting solution was stirred for one minute at 20 °C to mix the $((CH_3)_3Si)_2S$ into solution well. A slight excess of MoF_6, 0.410 g (1.95 mmol) was transferred into the reaction vessel at -196 °C. The reaction vessel was allowed to

warm towards room temperature very slowly with constant agitation and quenching in liquid N_2 to prevent side-reactions. The reaction mixture changed from colourless to yellow/brown even as solvent was still solid at temperatures below –120 °C. As the reaction progressed the reaction mixture changed to a homogeneous dark purple colour which persisted even at room temperature. The dark purple solid settled from the solvent, which was slowly removed into a ¾-in. o.d. FEP U-tube at –196 °C with other volatile byproducts, yielding 0.300 g (1.47 mmol) yellow-brown $MoSF_4$ in a 86 % yield.

2.6.2 Attempted Preparation of $MoSF_4$ from MoF_6 with $(CH_3)_3SiS$ in CH_3CN

Acetonitrile (0.410 g) was vacuum distilled into a ¼-in. o.d. FEP T-reactor at equipped with a stainless-steel Swagelok T-connection at –196 °C (Figure 2.1.3(c)). Then, 0.014 g (0.078 mmol) of $((CH_3)_3Si)_2S$ was vacuum distilled on top of the frozen CH_3CN on the glass line. The reaction vessel was connected to the metal line and 0.10 mmol of MoF_6 was transferred to the frozen reaction mixture. When the solvent melted the reaction mixture began to darken significantly. Upon warming to room temperature the dark red/brown solution was decanted to the other arm of the T-reactor and the solvent was removed under dynamic vacuum into a U-tube at –196 °C leaving a dark solid in the side arm of the reactor. After solvent removal was complete the reactor was backfilled and brought into the dry box where the straight arm of the T-reactor was disconnected from the Swagelok T-connector and exchanged for a 4-mm o.d. FEP tube. Outside the drybox, acetonitrile was vacuum-distilled on top of the recovered solid. The CH_3CN solution was decanted into the 4-mm FEP NMR tube where the contents were frozen and the tube was heat-sealed under dynamic vacuum.

2.6.3 Attempted Preparation of $MoSF_4$ from MoF_6 and H_2S in $CFCl_3$

Approximately 1.8 mL of $CFCl_3$ was distilled into a ¼-in. o.d. FEP reactor equipped with a Kel-F valve at -196 °C. Hydrogen sulfide was condensed into the reactor, which upon warming to room temperature, formed a clear and colourless solution in $CFCl_3$. Molybdenum hexafluoride was vacuum distilled into the reactor at -110 °C. Yellow and brown solid immediately appeared on the side walls of the reactor above the solution. Everything that came into contact with solution was dark brown/black a

possible sign of MoS_3 production. The reaction was very difficult to control. The solid product was characterized by vibrational and NMR spectroscopy.

2.6.4 Synthesis of MoF_5

Inside the dry box 0.155g Sb_2S_3 (0.456 mmol) was transferred into a bent ¼-in. o.d. FEP reaction vessel. A large excess of MoF_6 (0.494 g, 2.35 mmol) was vacuum distilled on top of the Sb_2S_3 at -196 °C and the contents were warmed to room temperature. The contents were agitated once the reactor was at room temperature. The MoF_6 began to turn yellow until ca. 1h later the MoF_6 solution was dark yellow. The solution was decanted and the MoF_6 was removed under vacuum at room temperature. A yellow crystalline solid was left behind. The reactor was brought into the glove box where crystals were collected and Raman and infrared samples were prepared. The yellow solid readily dissolved in CH_3CN forming a clear and colourless solution which upon freezing appeared bright yellow.

2.6.5 Reaction of MoF_5 with $[N(CH_3)_4][SSi(CH_3)_3]$

Inside the dry box, 0.007 g (0.04 mmol) of MoF_5 and 0.007 g (0.04 mmol) of $[N(CH_3)_4][SSi(CH_3)_3]$ were added to a 4-mm o.d. FEP reactor equipped with a Kel-F valve. Approximately 0.005 mL of CH_3CN was vacuum distilled into the reaction vessel at -196 °C. The reactor was heat-sealed under dymanic vacuum and allowed to warm to room temperature. The solution immediately turned a brown colour with light brown precipitate. Fluorine-19 NMR spectroscopy on the sample did not show any signals.

2.7 Attempted Preparation of $MoSF_5^-$

2.7.1 Reaction of MoF_6 with $[N(CH_3)_4][SSi(CH_3)_3]$.

Inside the dry box, 0.004 g (0.02 mmol) of $[N(CH_3)_4][SSi(CH_3)_3]$ was added to a 4-mm o.d. FEP reactor. Acetonitrile (0.308 g) and MoF_6 were distilled on top of the solution at -196 °C. The reactor was heat sealed under dynamic vacuum and the solution was warmed to room temperature and agitated to encourage mixing. The solution turned a yellow colour. The sample was characterized by ^{19}F NMR spectroscopy. An extended period at room temperature caused the sample to turn a deep brown.

2.7.2 Reaction of $MoSF_4$ with $[N(CH_3)_4][F]$

Inside the dry box, 0.0020 g (0.0098 mmol) of $MoSF_4$ and 0.0016 g (0.017 mmol) of $N(CH_3)_4F$ were added to a 4-mm o.d. FEP reactor equipped with a Kel-F valve. Approximately 0.005 mL of CH_3CN was vacuum distilled into the reactor at -196 °C. The reactor was heat sealed and allowed to warm to room temperature. The sample was agitated to encourage mixing. Dark precipitate formed at the bottom of the reactor indicating a reaction took place. Fluorine-19 NMR spectroscopy showed one peak at -22.1 ppm most likely a result of excess $N(CH_3)_4F$.

2.8 NMR Spectroscopy

All NMR spectra were recorded on a 300 MHz Bruker Advance II NMR spectrometer. Samples were contained in sealed 4-mm FEP reaction vessels. All samples were collected unlocked and were externally referenced. Fluorine-19 NMR spectra were externally referenced to neat $CFCl_3$ while ^{1}H and ^{13}C NMR spectra were referenced to neat TMS at room temperature.

2.9 Raman Spectroscopy

All Raman Spectra were recorded on a Bruker RFS 100 FT Raman spectrometer with a quartz beam splitter, a liquid-nitrogen cooled Ge detector, and low temperature accessory. The backscattered (180°) radiation was sampled. The useable Stokes range was 50-3500 cm^{-1} with a spectral resolution of 2 cm^{-1}. A Nd:Yag laser with a 1064-nm line was used for excitation of the sample. Spectra were recorded on powdered samples in sealed mp capillaries and solution samples in either 4-mm or ¼-in. o.d. FEP using powers between 40 and 300 mW. Samples were collected at temperatures between -100 and 20 °C.

2.10 Infrared Spectroscopy

All infrared spectra were recorded on a Nicolet Avatar 360 FTIR spectrometer at ambient temperature. The IR spectra were collected as KBr pellets formed inside the dry box using a Wilks minipress. The spectra were aquired in 16 scans at a resolution of 2 cm^{-1}.

2.11 Single Crystal X-ray Diffraction

2.11.1 Crystal Growth

Powdered $MoSF_4$ (0.015 g, 0.074 mmol) was added to a ¼-in. o.d. FEP T-reactor (Figure 2.1.3(b)) inside the dry box. Anhydrous hydrogen fluoride (*ca.* 1.2 mL) was vacuum distilled on top of the powder at -196 °C. The orange solution was agitated and left to settle for ca. 1 h before the solution was decanted to the side arm of the T-reactor.

Crystals of $MoSF_4$ were grown using a vacuum jacketed low-temperature Raman sample holder and the low-temperature liquid-nitrogen boil-off apparatus and controller that are part of the low-temperature Raman accessory. The temperature of the solution was slowly decreased from –65 to –72 °C on the controller (-53 to -59 actual) over a period of 6 hours. After completed crystal growth the solvent was decanted to the other sidearm of the T-reactor and subsequently removed by roughing vacuum. The crystals were kept cold at -78 °C while under dynamic vacuum.

Crystals of WSF_4 were formed directly from the reaction mixture by the slow removal of solvent HF at -78 °C under dynamic vacuum.

Crystals of MoF_5 were prepared by the removal of solvent MoF_6 from the decanted yellow solution under dynamic vacuum at 20 °C.

2.11.2 Low-Temperature Crystal Mounting

A low temperature crystal mounting technique was utilized for thermally unstable and/or moisture sensitive crystals. Each FEP reactor containing crystals was cut open below the KelF valve under a flow of dry nitrogen. The crystals were then quickly dumped from the chilled tube into an aluminum trough cooled by passing a flow of dry nitrogen through a 5-L Dewar of liquid nitrogen (Figure 2.11.1). The temperature of the trough had been previously adjusted to approximately -85 °C and had been measured with a copper-constantan thermocouple inserted midway into the stream ca. 2-mm above the trough. Each crystal was selected under a microscope and mounted on a glass fibre using an inert perfluorinated polyether, Fomblin Z-25 (Ausimont Inc.). The glass fibre had previously been attached using an epoxy to a metallic pin that was, in turn magnetically mounted on a wand. The polyether selected for crystal mounting was sufficiently viscous to adhere to the crystal, engulf it, and freeze quickly thereafter. The

attached crystal was quickly (<30 s) transferred to the goniometer head of the X-ray instrument using cryotongs which had been chilled by liquid nitrogen prior to use, and attached via a magnetic interface.

2.11.3 Collection and Reduction of X-ray data

Crystal structures were collected at temperatures from -100 to -120 °C on a Bruker AXS X-ray diffractometer equipped with an Apex II 4K charge-coupled device (CCD) area detector utilizing Mo Kα radiation (λ = 0.71073 Å) with a graphite monochrometer. The crystal-to-detector distance was 6.000 cm. A hemisphere of data was collected with 30 s exposure times. Cell reduction was carried out using the Program *SAINT* [3] which applied Lorentz and polarization corrections to three dimensionally integrated diffraction spots.

2.11.4 Solution and Refinement of Structures

Calculations were performed using the *Shelxtl v.614* plus package[4] for structure determination, refinement and molecular graphics. The *Xprep* program was used to confirm the unit cell dimensions and the crystal lattice. Solutions were obtained using direct methods. Successive difference Fourier syntheses revealed all light atoms. The structures were minimized by least squares refinement based on the square of the structure factors, F^2. Atom positions were refined anisotropically. Extinction coefficients were calculated for each crystal structure. Both residual values, R_1 based on F and the weighted residual values wR_2 based on F^2, are available in the structure refinement tables along with the goodness of fit *GooF*. They represent the following equations:

$$R_1 = \frac{\sum || Fo | - | Fc ||}{\sum | Fo |}$$ The conventional R-factor based upon the structure factor.

$$wR_2 = \sqrt{\frac{\sum [w(Fo^2 - Fc^2)^2]}{\sum [w(Fo^2)^2]}}$$ The Weighted R-Factor based upon intensity.

$$GooF = \sqrt{\frac{\sum [w(Fo^2 - Fc^2)]}{(n-p)}}$$ The *GooF* is based upon intensity where n is the number of reflections, p is the number of parameters refined.

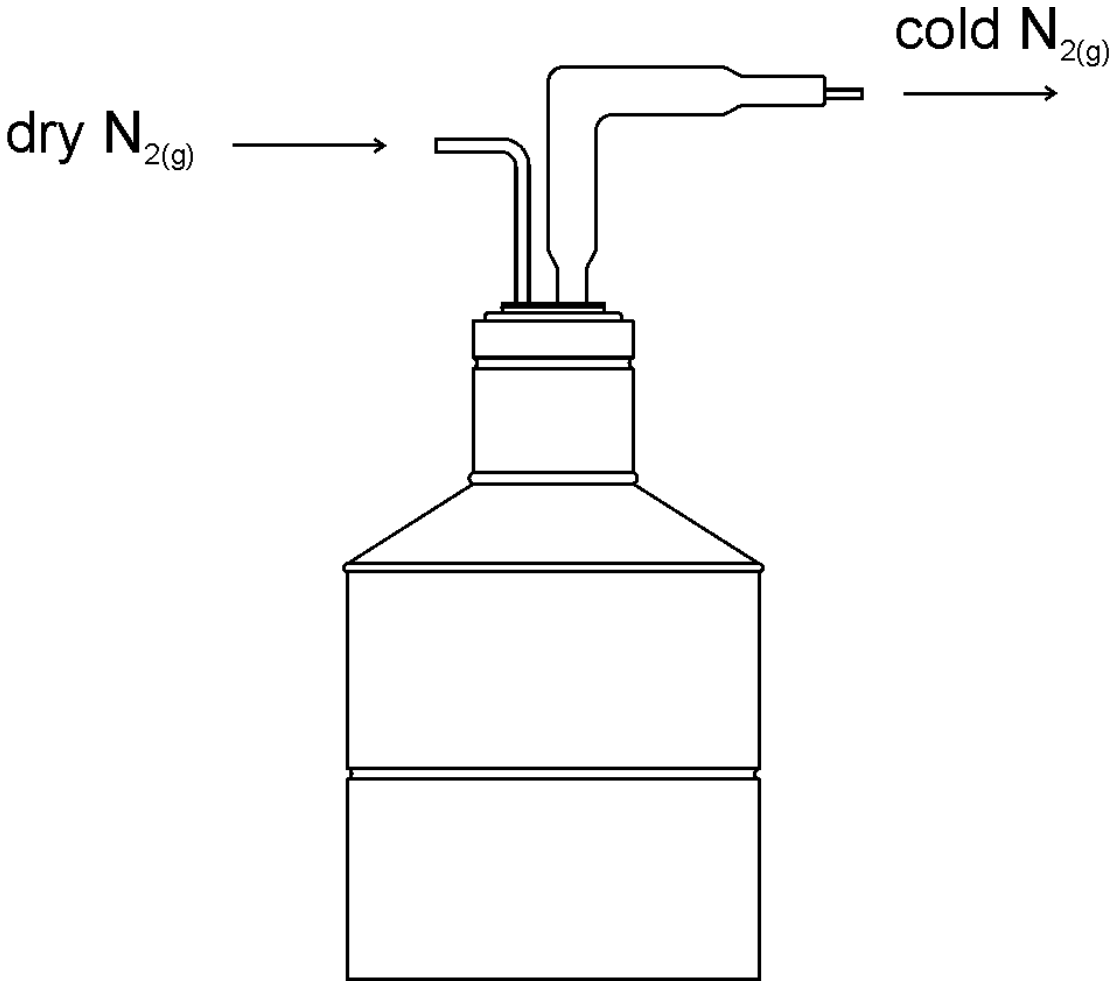

Figure 2.11.1 Crystal mounting apparatus consisting of a five-litre liquid nitrogen Dewar equipped with a rubber stopper, a glass dry nitrogen inlet and a silvered-glass cold nitrogen outlet with aluminium cold trough .

2.12 Computational Results

All calculations were performed in Gaussian 98[5] and viewed in Gaussview 03. Density functional theory calculations were performed at the B3LYP level of theory using the 6-31G(D) basis set for the trimethylsilanethiolate anion and the LANL2DZ basis set for $MoSF_4$, WSF_4, and WSF_5^-.

References

(1) Winfield, J. M. *J. Fluorine Chem.* **1984**, *25*, 91.

(2) Christe, K. O.; Wilson, W. W. *J. Fluorine Chem.* **1990**, *47*, 117.

(3) Bruker; Apex2 and Saint-plus. Bruker AXS Inc.: Madison, Wisconsin, USA, 2006.

(4) Sheldrick, G. M.; 6.14 ed.; Bruker AXS INC.: Madison, Wisconsin, USA., 2003.

(5) M. J. Frisch, G. W. T., H. B. Schlegel, G. E. Scuseria, M. A. Robb, J. R. Cheeseman, V. G. Zakrzewski, J. A. Montgomery, Jr., R. E. Stratmann, J. C. Burant, S. Dapprich, J. M. Millam, A. D. Daniels, K. N. Kudin, M. C. Strain, O. Farkas, J. Tomasi, ; V. Barone, M. C., R. Cammi, B. Mennucci, C. Pomelli, C. Adamo, S. Clifford, J. Ochterski, G. A. Petersson, P. Y. Ayala, Q. Cui, K. Morokuma, D. K. Malick, A. D. Rabuck, K. Raghavachari, J. B. Foresman, J. Cioslowski, J. V. Ortiz, A. G. Baboul, ; B. B. Stefanov, G. L., A. Liashenko, P. Piskorz, I. Komaromi, R. Gomperts, R. L. Martin, D. J. Fox, T. Keith, M. A. Al-Laham, C. Y. Peng, A. Nanayakkara, M. Challacombe, P. M. W. Gill, B. Johnson, W. Chen, M. W. Wong, J. L. Andres, C. Gonzalez, M. Head-Gordon, E. S. Replogle, and J. A. Pople; Gaussian, Inc: Pittsburgh PA, 1998.

Chapter 3

Synthesis and Characterization of Silanethiolate Salts

3.1 Introduction

Several sulfide transfer agents have been used in the past. Alkali metal or silver sulfides are common reagents, though these reagents have not been the preferred reactants for synthetic chemistry involving high-valent tungsten and molybdenum fluorides. For such syntheses antimony (III) sulfide and boron (III) sulfide have been the principal sulfide sources for high-temperature reactions. Observation and isolation of pure products unstable at high-temperature are untenable with such methods. It has been shown directly by Blackman *et al*.[1] that trimethylsilyl-sulfide reagents have great potential as sulfide transfer agents for group six metal fluorides in room temperature syntheses.

The very useful and commercially available hexamethyldisilathiane, $((CH_3)_3Si)_2S$, was first synthesized by Eaborn in 1950. Since then, the chemistry of $((CH_3)_3Si)_2S$ has become quite diverse as it has been used as a reagent in both organic and inorganic synthesis reactions especially in cases where disulfide bridges are a desired product.[2] Sodium trimethylsilanethiolate, has been prepared by at least two methods (Equations 3.1.1-2).[3-5] It has found utility in organic chemistry in cyclizations,[6] demethylations of aromatic methyl ethers,[3,7,8] conversion of nitriles to thioamides[3,9], and conversion of aromatic nitro to amine groups.[3,4] It has been shown for cyclization reactions that fluorine is the preferred nucleophile for successful heterocycle generation.[6] Sodium trimethylsilanethiolate has also been used successfully in inorganic chemistry for generation of transition-metal silanethiolate complexes[10,11] and sulfido ligand substitution reactions.[5]

$$((CH_3)_3Si)_2S + NaOCH_3 \xrightarrow{DMEU} NaSSi(CH_3)_3 + (CH_3)_3SiOCH_3 \qquad 3.1.1$$

$$(CH_3)_3SiCl + Na_2S \xrightarrow[EtOH]{DMEU} NaSSi(CH_3)_3 + NaCl \qquad 3.1.2$$

The strong silicon-oxygen bond (444 kJ/mol) relative to silicon-sulfur bond (292 kJ/mol) provides the significant driving force that has been employed in the conversion of carbonyls to thiocarbonyls at moderate temperatures[2]. The even stronger silicon-fluorine bond (594 kJ/mol) provides a much greater driving force, making silanethiolate salts prospective agents for efficient fluoride-sulfide substitution reactions.

3.2 Results and Discussion

3.2.1 Preparation of Trimethylsilanethiolate Salts

Four trimethylsilanethiolate salts were prepared by reactions of $((CH_3)_3Si)_2S$ and $[N(CH_3)_4][F]$, [K(18-crown-6)][F], CsF, and KF salts (Equation 3.2.1) at low temperature in CH_3CN. Temperatures below -35 °C proved necessary for synthesis of $[N(CH_3)_4][SSi(CH_3)_3]$ and $[K(18\text{-crown-6})][SSi(CH_3)_3]$ salts because the starting materials, anhydrous $[N(CH_3)_4][F]$ and [K(18-crown-6)][F] contained "naked fluoride," which attacks CH_3CN at temperatures higher than -35 °C. Temperatures of 0°C were used for reactions involving CsF and KF. The volatile $(CH_3)_3SiF$ byproduct was easily removed under vacuum.

$$MF + ((CH_3)_3Si)_2S \xrightarrow{CH_3CN} MSSi(CH_3)_3 + (CH_3)_3SiF \quad (M = N(CH_3)_4, K(18\text{-crown-6}), Cs, K) \qquad 3.2.1$$

Reaction 3.2.1 was most successful for production of $[N(CH_3)_4][SSi(CH_3)_3]$ and $[K(18\text{-crown-6})][SSi(CH_3)_3]$ salts with yields of 87.1 and 87.7 %, respectively. Production of $[Cs][SSi(CH_3)_3]$ and $[K][SSi(CH_3)_3]$ had lower yields of 71.8 and 64.5 %, respectively. The $[N(CH_3)_4][SSi(CH_3)_3]$ salt was produced successfully in high purity as verified by Raman and infrared spectroscopy. The trimethylsilanethiolate salts were all white flocculent solids that decomposed rapidly in contact with moisture generating volatile malodorous products.

Slow decomposition of the salts was observed in CH_3CN which resulted in fluorescence in the Raman spectra. Salts of $[N(CH_3)_4]^+$ and $[K(18\text{-crown-6})]^+$ were observed to readily react with CH_2Cl_2 upon dissolution while the $[Cs]^+$ salt seemed inert towards CH_2Cl_2.

The $[N(CH_3)_4][SSi(CH_3)_3]$ salt decomposed slowly at 167 °C without melting, decomposition became rapid at temperatures above 189 °C generating a colourless gas. The Cs^+ salt began to decompose slowly at 337 °C, liquidified at 340 °C and boiled by 343 °C leaving a small amount of unidentified white solid. The K^+ salt was stable to temperatures of 400 °C. The $[K(18\text{-crown-6})]^+$ salt decomposed at 50 °C

Crystal growth of $[N(CH_3)_4][SSi(CH_3)_3]$ was attempted from acetonitrile and THF by slow removal of solvent at low temperature and room temperature. Sublimation was also attempted, but the solid only decomposed into a colourless gas and a clear colourless unidentified substance. All attempts for crystal growth were unsuccessful.

The $Cs[SSi(CH_3)_3]$ salt formed solids with a small degree of crystallinity when CH_3CN was removed at -40 °C . A unit cell could not be obtained due to the poor quality of X-ray diffraction data.

3.2.2 Vibrational Spectroscopy of Trimethylsilanethiolate Salts

Raman and infrared spectra were recorded of $[N(CH_3)_4][SSi(CH_3)_3]$, $[K(18\text{-crown-6})][SSi(CH_3)_3]$, $Cs[SSi(CH_3)_3]$ and $K[SSi(CH_3)_3]$ (Figures 3.2.1-4). Vibrational frequencies together with their assignments are found in Tables 3.2.1-4. Raman frequencies of $SSi(CH_3)_3^-$ are compared in Table 3.2.5. Strong bands in the Raman spectra at *ca.* 500 cm^{-1} attributable to the Si-S (A_1) stretching mode are compared in Table 3.2.6.

Vibrational spectroscopy of alkali metal silanethiolate salts, K^+ and Cs^+, show only bands that are directly attributable to the stretching and bending modes of the $[SSi(CH_3)_3]^-$ anion (Tables 3.2.1-2). The assignment of these bands is based upon calculated frequencies and infrared intensities which are compared in Table 3.2.1. It is quite apparent that the infrared spectrum of $CsSSi(CH_3)_3$ contained more weak signals above 3000 cm^{-1}, than were found for the K^+ salt, which were likely the result of small amounts of hydrolysis while collecting infrared data.

Vibrational spectra of the $[K(18\text{-Crown-6})][SSi(CH_3)_3]$ salt are dominated by the 18-crown-6 constituent of the complex (Figure 3.2.4). Infrared and Raman data for neat 18-crown-6 were collected and are shown for comparison in Table 3.2.4.

Good agreement was found for the relative intensities and frequencies of the Raman bands attributed to the trimethylsilanethiolate anion (Table 3.2.5) of all salts.

From Table 3.2.6 it is quickly observed that the Si-S bond becomes stronger with larger, less coordinating cations. This trend continues to the covalently bonded, H^+, found in $(CH_3)_3SiSH$ with an Si-S stretch at 454 cm^{-1}.[12,13] This effect could be due to an increase in the ionic character of the S-Si bond as a result of stronger ion pairing from smaller more coordinating Cs^+ and K^+ cations resulting in lower stretching frequencies for the S-Si bond. With large, sterically hindered cations a higher degree of S-Si backbonding results from the effectively more negatively charged sulfur of trimethylsilanethiolate salts. Hyperconjugation would serve to increase Si-S bond strength upon donating electrons into the σ* antibonding molecular orbital of SiC_3, subsequently elongating the Si-C bonds and decreasing their frequency of vibration. This trend is observed in Table 3.2.5 with the slight decrease in the SiC_3 asymmetric stretch for salts with larger cations.

According to theory, non-linear molecules have 3N-6 normal modes of vibration, where N denotes the number of atoms in the molecule. The trimethylsilanethiolate anion should have 36 vibrational modes, as are found in table 3.2.8. The symmetry of the vibrational modes in the C_{3v} point group are represented by $\Gamma_{vib} = 8\ A_1 + 4\ A_2 + 12\ E$. Vibrations of A_1 and E symmetry can be observed in the Raman and infrared spectra while A_2 vibrations are Raman and infrared inactive. The observed vibrations therefore span the $8\ A_1 + 12$ E symmetry. Ignoring C-H vibrations and approximating CH_3 groups to spheres, the vibrations are simplified greatly to $\Gamma_{vib} = 3\ A_1 + 3$ E describing four stretching modes and five bending modes. The symmetry assignment of the vibrational bands is given in Table 3.2.5.

Table 3.2.1 Vibrational Spectroscopy Data from $K[SSi(CH_3)_3]$

Frequency, [a] cm^{-1}			
Raman[b]	Infrared[c]	Calculated [d]	Assignment
2948 (47)	2945 vs	3007 [94]	$\nu(CH_3)$ and combination
2887 (41)	2887 s	3000 [23]	
2810 (4)	2810 sh	3000 [23]	
1434 (3)	1435 m	1486-1499	$\delta(CH_3)$ deformations
1417 (sh)			
1403 (9)	1390 m		
	1304 w	1287-1298	
1246 (6)	1246 vs		
1239 (sh)			
849 (2)	852 vs	892 [224]	δ(Si-CH_3 rocking)
820 (5)	821 vs	855 [74]	
746 (3)	745 s	762 [20]	
736 (4)	730 s	761 [20]	
673 (17)	672 s	675 [0]	$\nu_{as}SiC_3$, E
667 (sh)			
641 (25)	637 s	641 [66]	ν_s SiC_3, A_1
	550 vw		
500 (100)	501 s	504 [11]	ν Si-S, A_1
	493 s		
	477 vw		
259 (19)		233 [4.3]	δ_{as} SiC_3, E
247 (18)		227 [0]	δ_s SiC_3, A_1
204 (31)		177 [0.7]	δ_{as} SiC_3, E

[a] Abbreviations denote shoulder (sh), very strong (vs), strong (s), medium (m), weak (w), and very weak (vw). [b] Neat solid in melting point capillary at room temperature. [c] KBr pellet at room temperature. [d] Calculations performed at B3LYP/6-31G(D) level of theory, calculated infrared intensities in square brackets; units of km/mol.

Table 3.2.2 Vibrational Spectroscopy Data from $Cs[SSi(CH_3)_3]$

Frequency, [a] cm^{-1}		
Raman[b]	Infrared[c]	Assignment
	3752 vw	$\nu(CH_3)$ and combination
	3695 br vw	
	3612 vw	
	3184 w	
2808 (sh)	3133 br w	
2790 (sh)	3040 sh	
2943 (32)	2942 sh	
2932 (48)	2931 vs	
2874 (42)	2874 s	
	2819 sh	
	2784 sh	
	2675 vw	
	2636 vw	
2457 (1)	2457 m	
	2069 w	
	1983 w	
	1904 m	
	1875 m	
	1745 w	
	1652 vw	
	1494 m	
1435 (2)	1432 s	
1420 (sh)		
1404 (11)	1399 s	$\delta(CH_3)$ deformations
	1338 m	
	1309 m	
	1280 vw	
1245 (5)	1245 vs	
1237 (9)	1234 vs	
	1145 w	
	1093 m	
	1011 m	
	959 vw	
843 (4)	843 vs	
826 (8)	826 vs	$\delta(CH_3)$ rocking
746 (6)	746 vs	
669 (32)	670 vs	ν_{as} SiC_3, E
640 (12)	640 vs	ν_s SiC_3, A_1
505 (100)	505 vs	ν Si-S, A_1
254 (24)		δ_s SiC_3, A_1
206 (31)		δ_{as} SiC_3, E

[a]Abbreviations denote shoulder (sh), very strong (vs), strong (s), medium (m), weak (w), and very weak (vw). [b] Neat solid in melting point capillary at room temperature. [c] KBr pellet at room temperature.

Table 3.2.3 Vibrational Spectroscopy Data of $[N(CH_3)_4][SSi(CH_3)_3]$

Frequency, [a] cm^{-1}		Assignment [14]	
Raman[b]	Infrared[c]	$N(CH_3)_4^+$	$SSi(CH_3)_3^-$
	3087 br w		$\nu(CH_3)$
3024 (13)			
3013 (29)		ν(CH) and combination	
3000(35)	3000 vs		
2993 (39)			$\nu(CH_3)$
2941 (51)	2941 vs		
2887 (53)	2888 s	$\nu(CH_3)$ and combination	
2813 (25)	2812 m		
2784 (5)	2776 m		
	2749 w		
	2679 vw		
	2594 vw		$\nu(CH_3)$
	2524 vw		
	2505 vw		
	1632 br vw		(CH_3) deformations
1488 (5)	1488 vs	$\nu_2(A_1)$, $\nu_6(E)$	
1464 (15)	1465 m		
1451 (15)	1451 vw		(CH_3) deformations
	1421 vw	$\nu_{16}(T_2)$	
1414 (11)			
1398 (12)	1397 w		(CH_3)deformations
1292 (7)	1290 m	$\nu_{17}(T_2)$	
1244 (5)	1241 vs		
1236 (3)	1232 sh		(CH_3) deformations
1179 (7)			
	1071 vw		
966 (2)		$\nu_{18}(T_2)$	
952 (14)	952 vs		
941 (7)	943 w		
843 (3)	845 vs		
814 (3)	821 vs		$\delta(CH_3$ rocking)
765 (3)			
751 (30)	737 m	$\nu_3(A_1)$	
665 (18)	664 s		ν_{as} SiC_3, E
641 (8)	641 vs		ν_s SiC_3, E
509 (100)	508 s		ν Si-S, A_1
458 (24)	454 w	$\nu_{19}(T_2)$	
374 (sh)		$\nu_8(E)$	
364 (1)		$\nu_8(E)$	
250 (17)			δ_{as} CSiS, E
198 (38)			δ_{as} SiC_3, E

[a]Abbreviations denote shoulder (sh), very strong (vs), strong (s), medium (m), weak (w), and very weak (vw). [b] Neat solid in melting point capillary at room temperature. [c] KBr pellet at room temperature.

Table 3.2.4 Vibrational Spectroscopy Data of Solid [K(18-Crown-6)][$SSi(CH_3)_3$] Compared to Vibrational Spectroscopy Data of Neat 18-crown-6

Frequency, [a] cm^{-1}				
[K(18-Crown-6)][$SSi(CH_3)_3$]		18-crown-6		
Raman[b]	Infrared[c]	Raman[b]	Infrared[c]	Assignment
2991 (sh)		2991 (sh)		
2978 (sh)		2982 (sh)		
2948 (57)	2938 s	2949 (80)	2948 s	
2895 (100)[d]	2897 vs	2895 (100)	2899 vs	
2875 (71)	2865 sh	2874 (74)	2877 s	
2843 (64)		2842 (70)		
2824 (31)	2823 m	2822 (35)		
2810 (47)		2810 (54)	2815 sh	
2782 (16)[d]		2784 (16)		
2766 (16)[d]		2766 (17)		
2759 (sh)	2744 m	2759 (sh)	2742 m	
2735 (12)		2736 (13)		$\nu(CH_3)$ and combination
2726 (sh)		2722 (10)		
2702 (13)		2704 (15)	2704 w	
2664 (7)		2665 (1)		
	1972 m		1972 m	
1493 (33)	1495 m	1493 (45)	1495 m	
1473 (35)[d]	1475 s	1477 (26)	1465 m	
1460 (12)[d]		1454 (9)	1459 m	
1446 (22)[d]		1445 (22)	1444 m	
1413 (6)[d]	1413 sh	1413 (4)	1412 w	
1388 (<1)	1382 s	1389 (4)	1384 w	
1374 (5)		1374 (6)	1378 w	
1354 (<1)	1350 s	1356 (<1)	1354 vs	
1340 (<1)		1340 (<1)		
1334 (<1)	1333 s		1334 s	
1295 (17)		1296 (23)	1297 s	
1279 (sh)	1282 m			
1273 (26)[d]		1276 (20)		$\delta(CH_3)$ deformations
1259 (22)		1259 (25)	1260 s	and 18-crown-6
1245 (sh)	1244 sh	1245 (sh)		
1237 (12)[d]	1238 m	1236 (11)	1238 m	
	1228 m	1220 (<1)	1219 m	
1158 (8)		1159 (10)	1153 sh	
1136 (sh)	1137 sh		1137 sh	
1133 (26)		1133 (32)		
1109 (6)	1103 vs	1109 (5)	1105 vs	
1090 (7)	1090 w	1090 (9)		
1082 (1)				
1070 (sh)			1075 w	
1063 (6)		1063 (8)	1058 m	
1046 (9)	1050 w	1046 (14)	1041 m	
1008 (<1)				
987 (12)	991 m	987 (16)	991 s	
	963 s	974 (<1)	963 s	
937 (<1)		935 (<1)	944 s	
892 (21)[d]	889 s	892 (22)	887 w	
872 (sh)				
867 (19)		866 (24)	859 vs	$\delta(Si\text{-}CH_3$ rocking)
830 (sh)	837 s	834 (sh)	828 m	and 18-crown-6
823 (20)	818 m	823 (24)		
739 (<1)	739 m	739 (<1)		
673 (sh)				
662 (5)	661 m			$\nu_{as}\,SiC_3$, E
642 (3)	642 m			$\nu_s\,SiC_3$, A_1
620 (<1)		620 (<1)		
600 (<1)		598 (<1)		
580 (8)	569 w	581 (10)	569 s	18-crown-6
549 (6)	537 m	551 (<1)	537 s	
523 (5)		524 (5)		
511 (33)	510 s			ν Si-S, A_1
493 (1)				
455 (<1)	465 w	449 (3)	462 m	
416 (22)[d]		416 (3)	406 m	
367 (2)				
353 (3)		353 (2)		
322 (5)		321 (8)		
309 (1)[d]		309 (sh)		
280 (sh)				$\delta_{as}\,CSiS$, E
270 (12)		271 (15)		
250 (sh)				$\delta_s\,SiC_3$, A_1
196 (8)[d]		190 (1)		$\delta_{as}\,SiC_3$, E
131 (sh)				

[a]Abbreviations denote shoulder (sh), very strong (vs), strong (s), medium (m), weak (w), very weak (vw), [b] Neat solid in melting point capillary at room temperature. [c] KBr pellet at room temperature. [d] [$SSi(CH_3)_4$] bands that overlap with those of 18-crown-6.

Table 3.2.5 Comparison of Raman Vibrational Data for Trimethylsilanethiolate Salts

Frequency, cm^{-1}					
H^{+} [12,13]	K^{+}	Cs^{+}	$[N(CH_3)_4]^{+}$	[K(18-crown-6)]$^{+}$ [a]	Assignment
180 (65)	204 (31)	206 (31)	198 (38)	196 (7) [21]	δ_{as} SiC_3, E
232 (64)	247 (18)	254 (24)	250 (17)	250 (sh)	δ_s SiC_3, A_1
335 (2)	259 (19)			280 (sh)	δ_{as} CSiS, E
454 (100)	500 (100)	505 (100)	509 (100)	511 (33) [100]	ν Si-S, A_1
634 (100)	641 (25)	640 (12)	641 (8)	642 (3) [9]	ν_s SiC_3, A_1
699 (28)	673 (17)	669 (32)	665 (18)	662 (5) [15]	ν_{as} SiC_3, E

[a] Values in square brackets show relative intensity compared to ν_s Si-S, A_1 for direct comparison to other silanethiolate salts.

Table 3.2.6 Si-S Stetching Modes Found in Raman Spectra of Silanethiolate Salts

Salt	Frequency, cm^{-1}
$HSSi(CH_3)_3$	454 (100)[12,13]
$[K][SSi(CH_3)_3]$	500 (100)
$[Cs][SSi(CH_3)_3]$	505 (100)
$[N(CH_3)_4][SSi(CH_3)_3]$	509 (100)
[K(18-crown-6)][$SSi(CH_3)_3$]	511 (33)

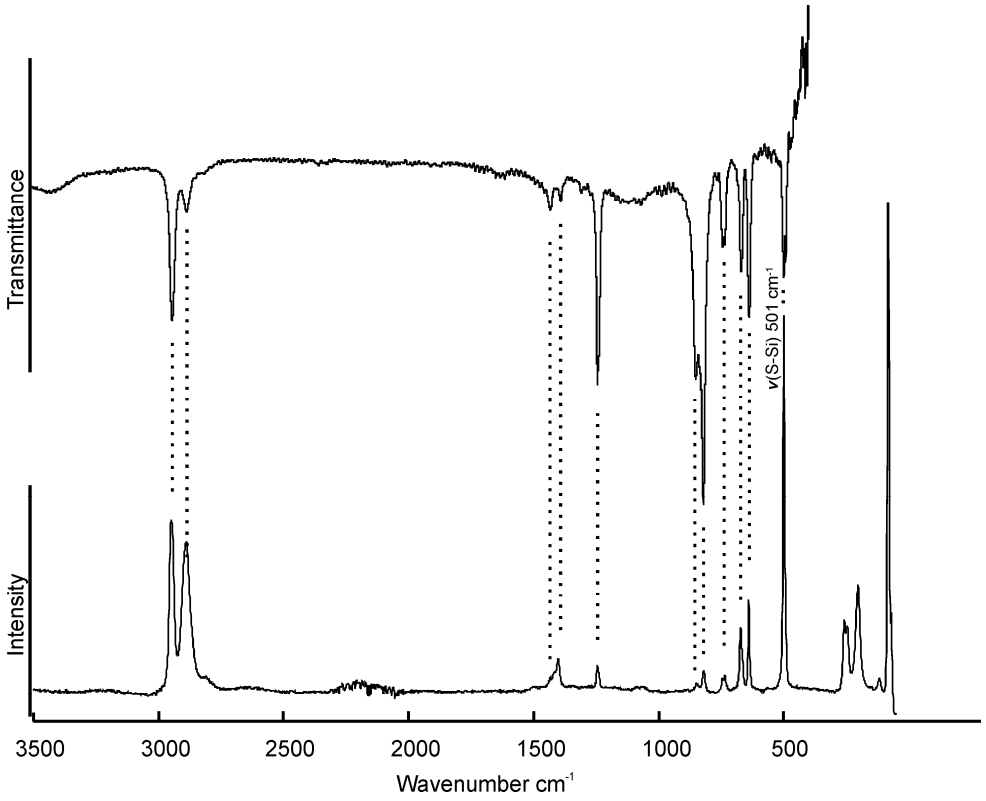

Figure 3.2.1 The vibrational spectra of $K[SSi(CH_3)_3]$ were collected at room temperature. The Raman spectrum (lower trace) was recorded on the neat solid in a glass melting point capillary. The infrared spectrum (upper trace) was collected as a KBr pellet.

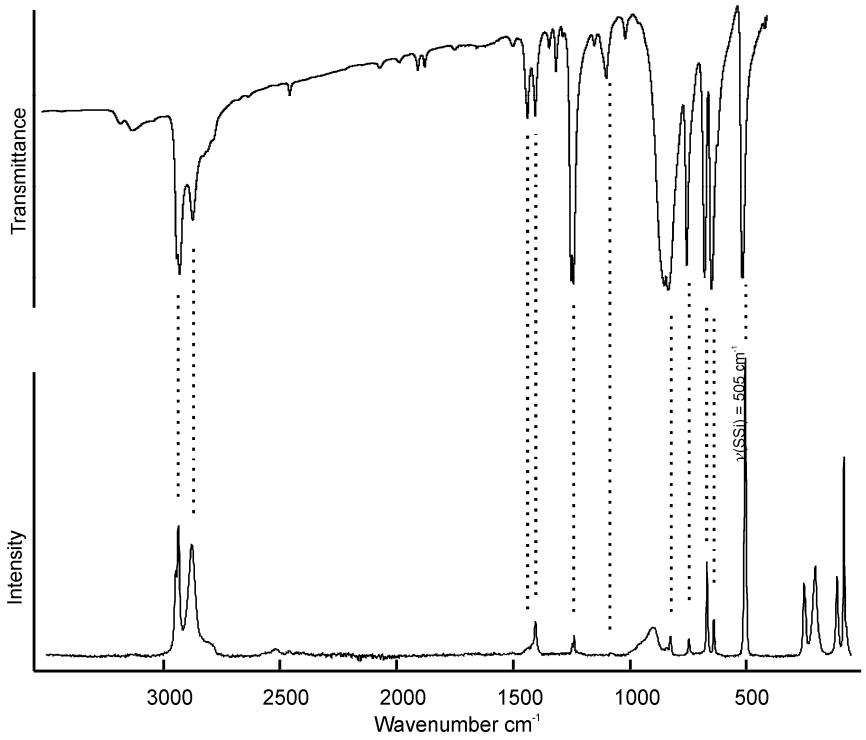

Figure 3.2.2 The vibrational spectra of $Cs[SSi(CH_3)_3]$ were collected at room temperature. The Raman spectrum (lower trace) was recorded on the neat solid in a glass melting point capillary. The infrared spectrum (upper trace) was collected as a KBr pellet.

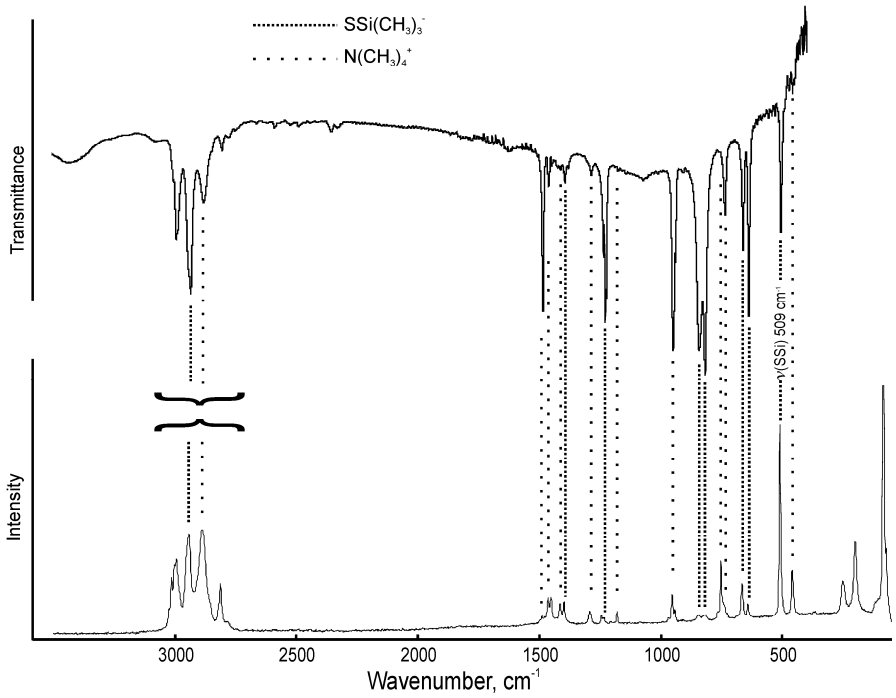

Figure 3.2.3 The vibrational spectra of $[N(CH_3)_4][SSi(CH_3)_3]$ were collected at room temperature. The Raman spectrum (lower trace) was recorded on the neat solid in a melting point capillary. The infrared spectrum (upper trace) was collected as a KBr pellet.

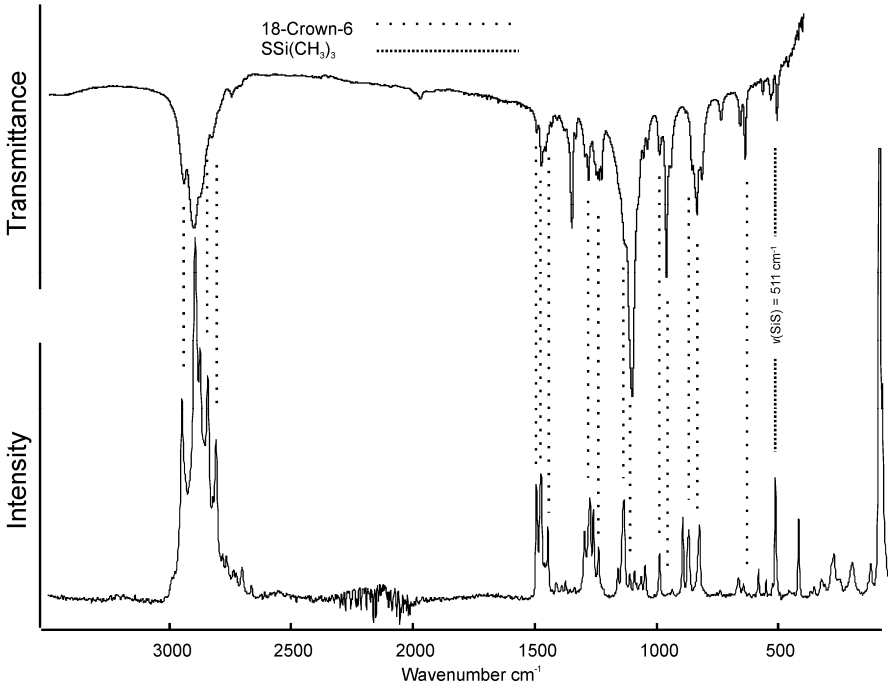

Figure 3.2.4 The vibrational spectra of [K(18-crown-6)][$SSi(CH_3)_3$] were collected at room temperature. The Raman spectrum (lower trace) was recorded on neat solid in a glass melting-point capillary. The infrared spectrum (upper trace) was collected as a KBr pellet

3.2.3 Density Functional Theory Calculations of Silanethiolate Salts

Density Functional Theory Calculations were performed on the $[SSi(CH_3)_3]^-$ anion at the B3LYP/6-31G(D) level of theory. Geometry optimization and frequency calculations were performed in separate steps. Calculated vibrations were viewed using Gaussview 3.09.

The $[SSi(CH_3)_3]^-$ anion ideally assumes C_{3v} point symmetry, this geometry is confirmed by DFT calculations (Figure 3.2.5) (Table 3.2.7). Bond lengths and angles are given and compared to calculated bond lengths and angles for $(CH_3)_3SiSH$ in Table 3.2.7. Comparision of the calculated values for $(CH_3)_3SiS^-$ and $(CH_3)_3SiSH$ indicate that the anion has a significantly shorter Si-S bond and longer Si-C bonds which is confirmed by experimental spectroscopic evidence. This in turn supports the argument that the higher frequency for the Si-S stretch of larger cation salts is a result of hyperconjugation.

The calculated frequencies, Raman scattering activities, and infrared intensities are shown in Table 3.2.8 along with vibrational descriptions and symmetry assignments. The Si-S stretching mode (Table 3.2.2) was calculated to appear at 505 cm^{-1} which is in the midst of experimental data for the silanethiolate salts prepared. The good agreement along with identical calculations performed on the $(CH_3)_3SiSH$ molecule that calculated the Si-S stretch for that molecule at 451 cm^{-1}, (literature 454 cm^{-1} Table 3.2.6) indicate that DFT calculations at the B3LYP level of theory using the 6-31G(D) basis set are good at describing these systems.

The calculated vibrational intensities (Table 3.2.8) have been shown to be much closer to experiment in predicting infrared intensity than for predicting Raman scattering activity. For this reason only calculated infrared intensity is given in comparison of experiment to calculation in Table 3.2.1.

The strong agreement between the number of signals and their positions expected from theory and calculation indicate that the anions do not conform to lower site symmetry which would cause splittings of the predicted vibrational bands.

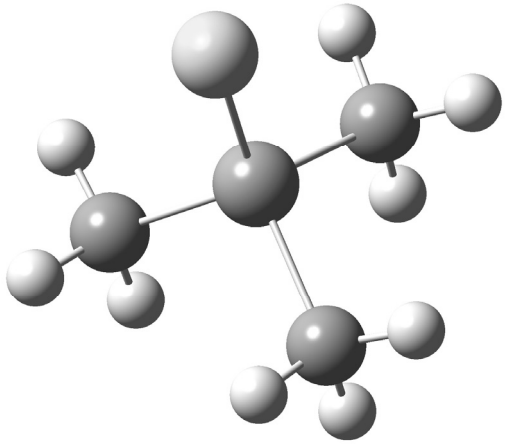

Figure 3.2.5 The geometry-optimized trimethylsilanothiolate anion shows approximate C_{3v} symmetry. Density functional theory calculations were performed at the B3LYP/6-31G(D) level of theory.

Table 3.2.7 Calculated Geometries of $(CH_3)_3SiS^-$ Anion and $(CH_3)_3SiSH$ Molecule at the B3LYP/6-31G(D) Level of Theory.

	$(CH_3)_3SiS^-$ Anion	$(CH_3)_3SiSH$
Bond	Bond length, pm	Bond Length, pm
S -Si	206	219
Si –C	192	189
C -H	110	110
	Bond Angle, °	Bond Angle, °
S-Si-C	114°	104°, 110°, 110°
C-Si-C	104°	111°

Table 3.2.8 Calculated Intensity of Raman and Infrared Vibrational Modes for the $SSi(CH_3)_3^-$ Anion and their Assignments within the C_{3v} Point Group

Frequency, cm^{-1}	Raman Activity[a]	Infrared Intensity[b]	Assignment
3098	116	58	ν(C-H), E
3097	114	59	ν_s(C-H), A_1
3079	228	123	ν_s(C-H), A_1
3072	23.2	17	ν_{as}(C-H), E
3007	394	94.6	ν_s(C-H), A_1
3000	7.9	23.6	ν_{as}(C-H), E
1513	2.1	0.1	$\delta_s(CH_3)$, A_1
1499	0.4	1	$\delta_{as}(CH_3)$, E
1493	48.7	0.3	$\delta_{as}(CH_3)$, E
1486	0.1	0	$\delta_s(CH_3)$, A_2
1298	3.6	6.1	$\delta_s(CH_3)$, A_1
1287	2.8	17	$\delta_{as}(CH_3)$, E
892	2.6	225	$\delta_s(CH_3)$ rocking, E
855	2.1	74.7	$\delta_{as}(CH_3)$ rocking, E
761	5.8	20.3	$\delta_{as}(CH_3)$ rocking, E
675	0	0	$\delta_s(CH_3)$ rocking, A_2
641	11	66.7	$\nu_s(SiC_3)$, A_1
632	8.1	26	$\nu_{as}(SiC_3)$, E
504	25.9	11.5	ν_s(S-Si), A_1
233	3.2	4.3	$\delta_{as}(SiC_3)$, E
227	0.6	0.3	$\delta_s(SiC_3)$, A_1
177	2.5	0.7	$\delta_{as}(SiC_3)$, E
155	0.2	0.1	(CH_3) rotation, A_2
135	0	0	(CH_3) rotation, A_2

[a] Calculated Raman scattering activity is in units of a^4/u. [b] Calculated infrared intensity is in units km/mol.

3.2.4 NMR Spectroscopy of Silanethiolate Salts

Nuclear magnetic resonance (NMR) spectroscopy was used to check the solubility and purity of the trimethylsilanethiolate salts in CH_3CN. The ^1H NMR chemical shifts of the anion for various salts are compared in Table 3.2.9.

The ^{13}C and ^1H NMR spectra showed that the $[N(CH_3)_4]^+$ salt was moderately soluble in CH_3CN. Chemical shifts of +3.35 and +0.16 ppm for $[N(CH_3)_4]^+$ and $[SSi(CH_3)_3]^-$ were observed, respectively, in the ^1H NMR spectrum. The chemical shift of the $[SSi(CH_3)_3]^-$ anion was close to the standard TMS. Two separate chemical shifts were recorded for $[N(CH_3)_4][SSi(CH_3)_3]$ in the ^1H-decoupled ^{13}C NMR spectrum. The cation $[N(CH_3)_4]^+$ was a 1:1:1 triplet at +55.7 ppm with a $^1J(^{13}C\text{-}^{14}N)$ coupling of 4.05 Hz while $[SSi(CH_3)_3]^-$ was a singlet at +8.43 ppm.

The ^1H NMR spectrum of $[N(CH_3)_4][SSi(CH_3)_3]$ in THF (C_4H_8O) showed a small singlet for $[SSi(CH_3)_3]^-$ at +0.12 ppm with ^{13}C-satellites with $^1J(^1H\text{-}^{13}C)$ coupling of 180 Hz. The 1H resonance for $[N(CH_3)_4]^+$ was obscured by the solvent signal. The difference in the chemical shift compared to $[N(CH_3)_4][SSi(CH_3)_3]$ in CH_3CN is an indication that an interaction may occur between the $SSi(CH_3)_3^-$ anion and the solvent THF.

In HF $[N(CH_3)_4][SSi(CH_3)_3]$ broke down to form $(CH_3)_3SiF$ which is easily recognized by $^3J(^1H\text{-}^{19}F)$ coupling of *ca* 8 Hz showing as a doublet at +0.44 ppm in the ^1H NMR spectrum and a decet at -157 ppm in the ^{19}F NMR spectrum. Signals at +3.25 ppm in the ^1H NMR spectrum and +29.9 and +34.1 ppm in the ^{19}F NMR spectrum were also observed.

The ^1H NMR spectrum of $[K(18\text{-crown-}6)][SSi(CH_3)_3]$ in CH_3CN contained a singlet at +3.67 ppm with complex ^{13}C satellite pattern showing coupling to several different carbons (ca. $^1J(^{13}C\text{-}^1H)$ = 148 to 132 Hz) corresponding to $[K(18\text{-crown-}6)]^+$. The satellites were comprised of at least five different components separated by 0.006 ppm (1.8 Hz). Magnetic inequivalence of the hydrogen environments is likely the cause of this complexity. The $[SSi(CH_3)_3]^-$ anion signal was found to be at +0.16 ppm, very close to the result for the $[N(CH_3)_4]^+$ salt. Carbon-13 satellites were barely discernable about the singlet. The ^1H-decoupled ^{13}C NMR spectrum showed one singlet at +70.95 ppm corresponding to the $[K(18\text{-crown-}6)]^+$ no signal for the anion could be detected.

The ^{1}H NMR spectrum of $KSSi(CH_3)_3$ showed a singlet from the anion at +0.17 ppm while the ^{1}H-decoupled ^{13}C NMR spectrum showed one small singlet at +8.43 ppm; both attributable to the $[SSi(CH_3)_3]^-$ anion. The ^{13}C NMR signal of the anion is corroborated by the ^{13}C NMR signal from $[SSi(CH_3)_3)]^-$ at +8.43 ppm for the $[N(CH_3)_4]^+$ salt.

The ^{1}H NMR spectrum of $CsSSi(CH_3)_3$ gave a singlet at +0.17 ppm with ^{13}C satellites from $^{1}J(^{1}H\text{-}^{13}C)$ coupling of 117 Hz corresponding to $[SSi(CH_3)_3]^-$. Also present was a doublet at +0.36 ppm corresponding to $(CH_3)_3SiF$ with the characteristic $^{3}J(^{1}H\text{-}^{19}F)$ coupling of *ca* 8 Hz. The ^{1}H decoupled ^{13}C NMR spectrum showed one singlet at +8.32 ppm corresponding to the $[SSi(CH_3)_3]^-$ anion differing only slightly from ^{13}C NMR shifts for K^+ and $[N(CH_3)_4]^+$ salts. A ^{19}F NMR spectrum contained a small signal at *ca.* -155 ppm from $(CH_3)_3SiF$ in agreement with ^{1}H NMR data indicating that a very small amount of starting material CsF may have been present in the $CsSSi(CH_3)_3$ product.

In Table 3.2.9 the chemical shift of the $SSi(CH_3)_3^-$ anion is relatively constant for all salts dissolved in CH_3CN, indicating the choice of cation has little to do with the anion-solution interaction (besides solubility). There is a relatively large discrepancy between the chemical shift of the anion in THF compared to CH_3CN, which is also coupled with a large change in the $^{1}J(^{1}H\text{-}^{13}C)$ observed, indicating that an interaction with the donor solvent likely occurs.

Attempts were made to collect ^{29}Si NMR signals for all salts though none were detected. It is likely that the signals were not observed due to slow spin-lattice relaxation.

Table 3.2.9 ^{1}H NMR Spectroscopy Data of $SSi(CH_3)_3^-$ Anion in Solution at Room Temperature.

Salt	Solvent	Chemical Shift (ppm)	$^{1}J(^{1}H-^{13}C)$ (Hz)
$[K(18\text{-crown-}6)][SSi(CH_3)_3]$	CH_3CN	+0.16	
$[N(CH_3)_4][SSi(CH_3)_3]$	CH_3CN	+0.16	
	THF	+0.12	180
$Cs[SSi(CH_3)_3]$	CH_3CN	+0.17	117
$K[SSi(CH_3)_3]$	CH_3CN	+0.17	

3.3 Summary

Hexamethyldisilathiane is a useful reagent for the preparation of ionic trimethylsilanethiolate salts. Novel salts of $N(CH_3)_4^+$, $K(18\text{-crown-}6)^+$, Cs^+, and K^+ were successfully prepared with excess amounts of $((CH_3)_3Si)_2S$ in CH_3CN solvent. Their vibrational spectra were collected and compared, to each other and density functional theory calculations showing many similarities and general trends based upon the size of the cation that accompanied $SSi(CH_3)_3^-$. The lack of extra vibrational bands indicates that lower site symmetry is not imposed on the anion in the solid state. Solutions of each salt in CH_3CN showed very similar chemical shifts for the anion indicating the cation did not seem to have a large effect on their interaction with solution.

References

(1) Banger, K. K.; Blackman, C. S.; Brisdon, A. K. *J. Chem. Soc., Dalton Trans.* **1996**, 2975–2978

(2) Degl'Innocenti, A.; Capperucci, A. *J. Sulfur Chem.* **1998**, *20*, 279.

(3) Shiao, M. J.; Lai, L. L.; Ku, W. S.; Lin, P. Y.; Hwu, J. R. *J. Org. Chem.* **1993**, *58*, 4742.

(4) Hwu, J. R.; Wong, F. F.; Shiao, M. J. *J. Org. Chem.* **1992**, *57*, 5254.

(5) Do, Y.; Simhon, E. D.; Holm, R. H. *Inorg. Chem.* **1983**, *22*, 3809.

(6) Lai, L. L.; Lin, P. Y.; Huang, W. H.; Shiao, M. J.; Hwu, J. R. *Tetrahedron Lett.* **1994**, *35*, 3545-3546.

(7) Shiao, M. J.; Ku, W. S.; Hwu, J. R. *Heterocycles* **1993**, *36*, 323.

(8) Hwu, J. R.; Tsay, S. C. *J. Org. Chem.* **1990**, *55*, 5987.

(9) Lin, P. Y.; Ku, W. S.; Shiao, M. J. *Synthesis* **1992**, 1219.

(10) Liang, H. C.; Shapley, P. A. *Organometallics* **1996**, *15*, 1331.

(11) Shapley, P. A.; Liang, H. C.; Dopke, N. C. *Organometallics* **2001**, *20*, 4700.

(12) Goubeau, J.; Hiersemann, W. D. *Z. Anorg. Allg. Chem.* **1957**, *290*, 292-301.

(13) Kriegsmann, H. *Z. Anorg. Allg. Chem.* **1958**, *294*, 113-119.

(14) Kabisch, G.; *J. Raman Spectrosc*. **1980**, *9*, 279.

Chapter 4

Synthesis and Characterization of WSF_4

4.1 Introduction

Tungsten sulfide tetrafluoride, WSF_4, is the transition-metal sulfide fluoride that has been studied most extensively. Prior syntheses of WSF_4 involved the reaction of WF_6 with B_2S_3 or Sb_2S_3 at high temperatures[1,2] or with $((CH_3)_3Si)_2S$ in CH_3CN and CH_2Cl_2 solvents at ambient temperature.[3] The production of significant amounts of the WS_3 byproduct which formed via side reactions made it of interest to find a simpler and more reliable synthetic route to WSF_4. Little is known about the reactivity of WSF_4 especially in comparison to the oxygen analogue. A reliable preparative method for pure WSF_4 is necessary for the extensive study of its chemistry.

4.2 Results and Discussion

4.2.1 Syntheses of WSF_4

The best synthesis for pure WSF_4 in 300-mg quantities was found to be the reaction of WF_6 and Sb_2S_3 in anhydrous HF at ambient temperature (Equation 4.2.1).

$$Sb_2S_3 + 3\ WF_6 \xrightarrow{aHF} 3\ WSF_4 + 2\ SbF_3 \qquad 4.2.1$$

The reaction is slow, and it took more than one hour before a colour change was observed at room temperature. The slow approach seemed to have the significant advantage that only WSF_4 was produced with no signs of side reactions. The yellow colour of the solution became more intense with time. It was quite evident that larger amounts of anhydrous HF solvent increased the yield of yellow WSF_4 solid at the end of reaction. Deficiencies or a large excess of WF_6 had no effect on the product. Raman spectroscopy conducted on the reaction solution showed strong signals corresponding to WF_6 after 24 hours even when the solution was deep yellow and Sb_2S_3 was still visibly present. The

deep yellow HF solution was decanted to a side-arm of the reactor where the solvent HF was removed by vacuum at –78 °C giving a yellow solid that was isolated in an 82 % yield. Tungsten sulfide tetrafluoride was fully characterized by vibrational and ^{19}F NMR spectroscopy and X-ray crystallography.

It was necessary to remove all HF from the reaction mixture at –78 °C to maintain the yellow colour of the product. Any unreacted WF_6 was removed under dynamic vacuum at room temperature after complete removal of HF. Removal of HF at room temperature resulted in a large amount of dark material among the yellow product. It was observed that the yellow WSF_4 turned brown over *ca.* 48 hours at room temperature in the dry box and proceeded to get darker over longer periods. At low temperatures the solid maintained the original yellow colour.

Freshly generated WSF_4 quickly lost its solubility in HF. At first glance this seemed puzzling, as WSF_4 was highly soluble in HF during production. The solubility is only lost when the original solvating HF has been removed to generate the yellow solid product. Presumably solvated WSF_4 monomers are formed in HF solution; after removal of HF infinite chains of WSF_5 octahedra are formed, as found in the X-ray crystal structure of WSF_4. From that point on HF is not a strong enough Lewis base to entice a large amount of WSF_4 to dissolve. This remains the case, as the yellow product turns brown, as solutions in HF only ever achieve a very slight yellow colour.

The tendency of yellow WSF_4 to turn brown was a concern at first as it was important to know whether or not it was the result of particle size or decomposition. It can now be stated with certainty that the brown colouration of the yellow solid is the result of increased particle size. It is evident that the longer WSF_4 has been stored in the dry box the less electrostatic it becomes; freshly produced WSF_4 adheres to sides of reaction vessels much more persistently than dark brown WSF_4 that has been stored at room temperature for weeks. Solutions of WSF_4 in HF have the same pale yellow colour whether they are made with freshly prepared WSF_4 or older WSF_4. The bands of the Raman spectrum remain the same, as only fluorescence increases as the solid darkens. The addition of Lewis bases, like pyridine, causes the solubility of WSF_4 to increase significantly in anhydrous HF solvent, regardless of the coloration of WSF_4. Fluorine-19

NMR spectroscopy of $WSF_4 \cdot C_5H_5N$ did not show other species in solution, besides small amounts of hydrolysis products.

Prior to the successful method presented above, other methods were attempted to prepare WSF_4. The ambient-temperature reaction of WF_6 with $((CH_3)_3Si)_2S$ in CH_3CN (Equation 4.2.2) has been reported by Brisdon *et al.*[3] The repetition of this reaction at various temperatures resulted in solutions of WSF_4 and significant amounts of insoluble brown solid. The large amount of brown solid was attributed to uncharacterized side reactions that have been observed in the literature.[3] Solutions of WSF_4 in CH_3CN by themselves were observed to undergo a solvent-assisted dismutation to form WS_3 and WF_6 (Equation 4.2.3). Conducting the reaction at temperatures below –35 °C still resulted in large amounts of brown solid indicating that temperature was insufficient to prevent side reactions from occurring.

$$WF_6 + ((CH_3)_3Si)_2S \xrightarrow{CH_3CN} WSF_4 + 2\ FSi(CH_3)_3 \qquad 4.2.2$$

$$3\ WSF_4 \xrightarrow{CH_3CN} WS_3 + 2\ WF_6 \qquad 4.2.3$$

The reaction of H_2S with WF_6 in $CFCl_3$ (Equation 4.2.4) was attempted on several occasions, as it was a potential method for producing WSF_4 with only volatile by-products that could easily be removed under dynamic vacuum. The reaction between WF_6 and H_2S

$$WF_6 + H_2S \xrightarrow{CFCl_3} WSF_4 + 2\ HF \qquad 4.2.4$$

was very difficult to control. At room temperature the reactants formed a slightly yellow solution immediately upon addition of both reactants, which did not seem to get appreciably stronger coloured with time. Above the solution, however, the reaction vessel slowly became coated with a thin layer of dark solid that could not be removed. The solid layer was very thin and could not be studied but it was presumably WS_3 or WS_5. The partial pressure of H_2S above the $CFCl_3$ solution would have presumably been much larger than that of WF_6 making the excess H_2S required for production of WS_3 or WS_5 readily accessible. Any warming of the solution above room temperature resulted in

instantaneous formation of dark brown/black solid; in fact exposure to the Raman laser at room temperature was enough to turn the entire reaction mixture dark brown/black. When a reaction vessel was left in the dry box for several days it was noticed that white crystals formed. The crystalline material was studied by single-crystal X-ray diffraction and was shown to be tetrameric WF_5.[4] Crystal-structure information for WF_5 is available in the Appendix.

4.2.2 X-ray Crystal structure of WSF_4

Crystals of WSF_4 were obtained from the slow removal of anhydrous HF solvent from the reaction mixture of Sb_2S_3 and WF_6 at -78°C (Equation 4.2.1). Crystallographic parameters are listed in Table 4.2.1. Bond lengths and bond angles are given in Table 4.2.2. The tables of isotropic and anisotropic displacement parameters can be found in the Appendix.

Tungsten sulfide tetrafluoride crystallizes in the orthorhombic space group $Pca2_1$ with eight molecules per unit cell with cell dimensions of a = 1693.1(3) pm, b = 539.01(8) pm, c = 946.93(1) pm. The unit cell parameters obtained were in agreement with those obtained previously by Holloway *et al.* on crystals grown by sublimation.[2] The previous crystal structure collected by Holloway *et al.* retained a significantly higher residual value of 0.072 while the present structure could be refined to an R_1 value of 0.022 and represents a much improved structure of WSF_4 with significantly lower standard deviations in the bond lengths and angles.

It was confirmed that WSF_4 forms an infinite polymeric chain of *cis*-linked WSF_5 octahedra (Figure 4.2.1) which propagate along the *c*-axis of the unit cell. Three significantly different sets of tungsten-fluorine bond distances were found, (a) terminal W-F bonds ranging from 183.5(5)-185.2(4) pm, (b) W-F bonds that were *cis* to the W=S bonds form bridges to adjacent WSF_4 moieties (193.2(5)-194.7(5) pm), and (c) long bridging W─F bonds *trans* to the W=S bonds (230.8(5)-232.3(4) pm). Characteristic of tungsten fluorides and oxide fluorides the tungsten in WSF_4 molecule retains hexacoordination through fluorine bridging *trans*- to the sulfur atom in the solid phase. As expected the fluorine atom bonded *trans*- to the sulfur atom had a much longer W─F bond.

The tungsten atom is raised above the plane of four equatorial fluorine atoms toward the doubly bonded sulfur atom. The equatorial fluorine atoms are likely pushed downward by the W=S bond domain with S=W-F_{eq} bond angles ranging from 99.48(16) to 102.59(19)°. The F_{bridge}-W=S angle, however, is slightly smaller than the $F_{terminal}$-W=S bond angles because of decreased repulsion caused by the elongated W-F_{bridge} bond. The smaller W-F_{bridge} domain is also reflected by the F_{trans}-W=S angle of 177.90(4)°.

The structure of WSF_4 contrasts significantly with the crystal structure of WOF_4.[5] Unlike WSF_4, WOF_4 crystallizes as a tetramer in the space group *C*2/*m*. The similar sized unit cell *a* = 965(1), *b* = 1442(2), *c* = 515(1) pm also contains eight molecules. The terminal W-F bonds of WOF_4 are similar to WSF_4 ranging from 183(4) to 186(4) pm. The bridging W-F bond lengths in the WOF_4 crystal structure range from 210(4) to 212(4) pm. This contrasts with the crystal structure of WSF_4 where the W-F--W bridge forms a long bond *trans* to the sulfur, ranging from 230.8(5) to 232.3(4) pm, and a shorter bond cis to the sulfur, ranging from 193.2(5) to 194.7(5) pm. The WOF_4 crystal structure was considered to be disordered with respect to oxygen and fluorine atoms, though a *cis*-fluorine-bridged structure was preferred upon vibrational analysis.[6] The WOF_4 crystal structure was refined to a large residual value of 12.8 % as a result of poor data quality.

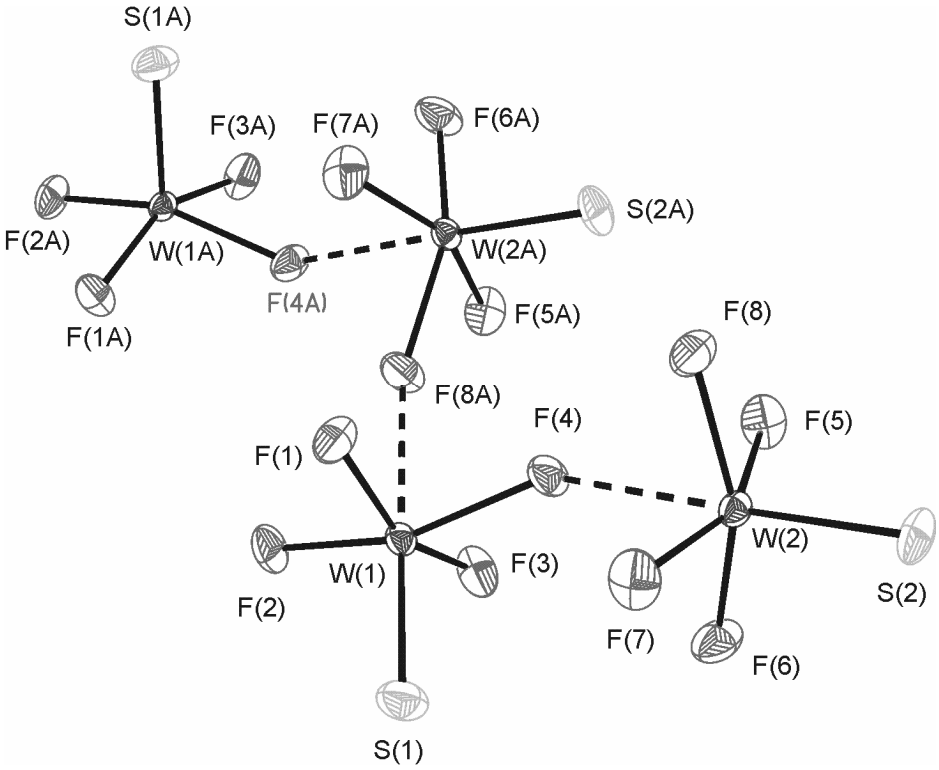

Figure 4.2.1 A view of the chain structure of WSF_4 with thermal ellipsoids shown at the 50 % probability level.

Table 4.2.1. Crystal Structure Refinement Data for WSF_4

Empirical formula	WSF_4
Formula weight, g mol^{-1}	291.91
Temperature, K	153(2)
Wavelength, pm	71.073
Crystal system	Orthorhombic
Space group	$Pca2_1$
Unit cell dimensions, pm	a = 1693.1(3)
	b = 539.01(8)
	c = 946.93(15)
Volume, 10^6 pm^3	0.8642(2)
Z	8
Density (calculated), mg mm^{-3}	4.487
Absorption coefficient, mm^{-1}	27.159
F(000)	1008
Crystal size, mm^3	0.10 x 0.06 x 0.03
Theta range for data collection	2.41 to 28.50°.
Index ranges	$-22 \le h \le 22$, $-7 \le k \le 6$, $-12 \le l \le 12$
Reflections collected	8865
Independent reflections	2058 [R(int) = 0.0380]
Completeness to theta = 28.50°	96.1 %
Max. and min. transmission	0.4963 and 0.1721
Refinement method	Full-matrix least-squares on F^2
Data / restraints / parameters	2058 / 1 / 110
Goodness-of-fit on F^2	1.112
Final R indices [I>2sigma(I)]	R_1 = 0.0217, wR_2 = 0.0403
R indices (all data)	R_1 = 0.0258, wR_2 = 0.0413
Absolute structure parameter	0.022(13)
Extinction coefficient	0.00022(6)
Largest diff. peak and hole, e 10^{-6} pm^{-3}	1.188 and -1.173

Table 4.2.2 Experimental Bond Lengths and Bond Angles of WSF_4.

Bond Length, pm		Bond Angle, °	
W(1)-F(1)	183.5(5)	F(1)-W(1)-F(3)	155.0(2)
W(1)-F(3)	184.4(5)	F(1)-W(1)-F(2)	91.9(2)
W(1)-F(2)	185.0(5)	F(3)-W(1)-F(2)	90.3(2)
W(1)-F(4)	194.7(5)	F(1)-W(1)-F(4)	85.1(2)
W(1)-S(1)	208.4(2)	F(3)-W(1)-F(4)	84.0(2)
W(1)-F(8)#1	230.8(5)	F(2)-W(1)-F(4)	158.8(2)
W(2)-F(6)	184.0(5)	F(1)-W(1)-S(1)	101.37(18)
W(2)-F(5)	184.5(5)	F(3)-W(1)-S(1)	102.59(19)
W(2)-F(7)	185.2(4)	F(2)-W(1)-S(1)	101.66(18)
W(2)-F(8)	193.2(5)	F(4)-W(1)-S(1)	99.48(16)
W(2)-S(2)	209.1(2)	F(6)-W(2)-F(5)	91.2(3)
W(2)-F(4)	232.3(4)	F(6)-W(2)-F(7)	90.1(3)
F(8)-W(1)#2	230.8(5)	F(5)-W(2)-F(7)	155.1(2)
		F(6)-W(2)-F(8)	158.2(2)
		F(5)-W(2)-F(8)	84.4(2)
		F(7)-W(2)-F(8)	85.2(2)
		F(6)-W(2)-S(2)	101.92(17)
		F(5)-W(2)-S(2)	102.48(17)
		F(7)-W(2)-S(2)	101.5(2)
		F(8)-W(2)-S(2)	99.86(16)
		F(6)-W(2)-F(4)	80.1(2)
		F(5)-W(2)-F(4)	77.9(2)
		F(7)-W(2)-F(4)	77.8(2)
		F(8)-W(2)-F(4)	78.07(19)
		S(2)-W(2)-F(4)	177.86(15)
		W(1)-F(4)-W(2)	147.0(3)

4.2.3 NMR Spectroscopy of WSF_4.

Fluorine-19 NMR spectra of WSF_4 in HF, CH_3CN, and C_4H_8O solvents were collected at ambient temperature. The chemical shifts and $^1J(^{19}F\text{-}^{183}W)$ coupling constants are listed in Table 4.2.3.

The equivalency of the fluorine environments in WSF_4 was confirmed by ^{19}F NMR spectroscopy. The only signal in CH_3CN was a singlet at +85.3 ppm with ^{183}W-satellites separated by 33.3 Hz (Table 4.2.3). It has been reported that CH_3CN acts as a Lewis base coordinating to WSF_4 forming the $WSF_4 \cdot CH_3CN$ adduct with the nitrogen atom trans to the sulfur.[2] The chemical shift at +85.3 ppm is in the same range as those found in the literature.[1,3] A small amount of the hydrolysis product WOF_4 was observed in the spectrum also at +66.7 ppm with a $^1J(^{19}F\text{-}^{183}W)$ coupling of 68 Hz illustrating the marked difference between the $^1J(^{19}F\text{-}^{183}W)$ coupling constants for sulfur and oxygen containing tungsten fluorides noted in the literature.[7] The large difference in $^1J(^{19}F\text{-}^{183}W)$ coupling aids distinguishing the respective species by ^{19}F NMR spectroscopy.

Over an extended period of time the yellow solution of WSF_4 in CH_3CN turned brown in colour, which may have been from the solvent assisted dismutation that WSF_4 is known to undergo in CH_3CN (Equation 4.2.3). A small unexplained doublet at +72.3 ppm with a *J*-coupling of 36 Hz was observed in the ^{19}F NMR spectrum.

Fluorine-19 NMR spectroscopy of a yellow solution in HF at room temperature showed a singlet at +77.42 ppm with a $^1J(^{19}F\text{-}^{183}W)$ coupling constant of 42.1 Hz corresponding to a solvated WSF_4 monomer. The spectrum contained a small amount of WOF_4 (from hydrolysis) indicated by a small singlet at +60.8 ppm.

The chemical shifts and coupling constants in Table 4.2.3 illustrate a trend with respect to the donor strength of the coordinating ligand. It is apparent that C_5H_5N, a strong electron donor, donor number (D.N) of 33.1, decreases the chemical shift of WSF_4 more than C_4H_8O (D.N = 20.0).[8] Donor numbers are a qualitative measure of Lewis basicity and are defined by the negative enthalpy of formation of a 1:1 adduct between the Lewis base and the standard Lewis acid $SbCl_5$. The trend continues with CH_3CN the weakest electron donor of the three organic ligands. The same trend is observed with regard to the $^1J(^{19}F\text{-}^{183}W)$ coupling of the WSF_4 adducts.

Table 4.2.3 ^{19}F NMR Spectroscopy of WSF_4

Chemical shift (ppm)	Solvent	$^1J(^{19}F\text{-}^{183}W)$ (Hz)	Assignment
77.4	HF	42.1	WSF_4
85.3	CH_3CN	33.3	$WSF_4 \cdot CH_3CN$
85.0	THF	28.5	$WSF_4 \cdot THF$
82.7	CH_3CN	29	$WSF_4 \cdot THF$
81.8	CH_3CN	26.8	$WSF_4 \cdot C_5H_5N$

4.2.4 Vibrational Spectroscopy of WSF_4

The Raman spectrum of freshly produced WSF_4 as a yellow solid was collected at room temperature and at –100 °C in a sealed melting point capillary. The vibrational frequencies together with tentative assignments are presented in Table 4.2.4. The vibrational bands were dominated by the intense W=S stretching and bending modes. Many smaller signals attributable to W-F stretching and bending vibrations were apparent in the spectrum. The vibrational spectrum is complicated by the presence of different W-F bonds and by vibrational coupling of fluorine-bridged WSF_4 moieties which makes a full vibrational assignment of the vibrational bands for solid WSF_4 difficult.

The stretching modes observed in the Raman spectrum of solid WOF_4 for W-F terminal stretching at 744 w, 728 m, and 705 vvw cm^{-1} are at slightly higher frequency than the analogous bands of WSF_4 at 717, 709, and 697 cm^{-1}. This trend is a result of the greater electron-withdrawing capability of the oxygen atom compared to the sulfur atom. The bands from the bridging W-F stretching modes follow the same trend at 663 vw, 563 vvw, and 523 vvw for WOF_4.[9]

The infrared spectrum of the solid shows very intense bands that overlap in the terminal W-F stretching region and bridging W-F stretching regions, which is typical of the solid tungsten and molybdenum fluorides. The spectrum also contained a strong band from the W=S stretching mode at 576 cm^{-1} between the terminal and bridging W-F stretching modes. Overlap of W-F stretching bands made fine details indiscernible in the infrared spectrum.

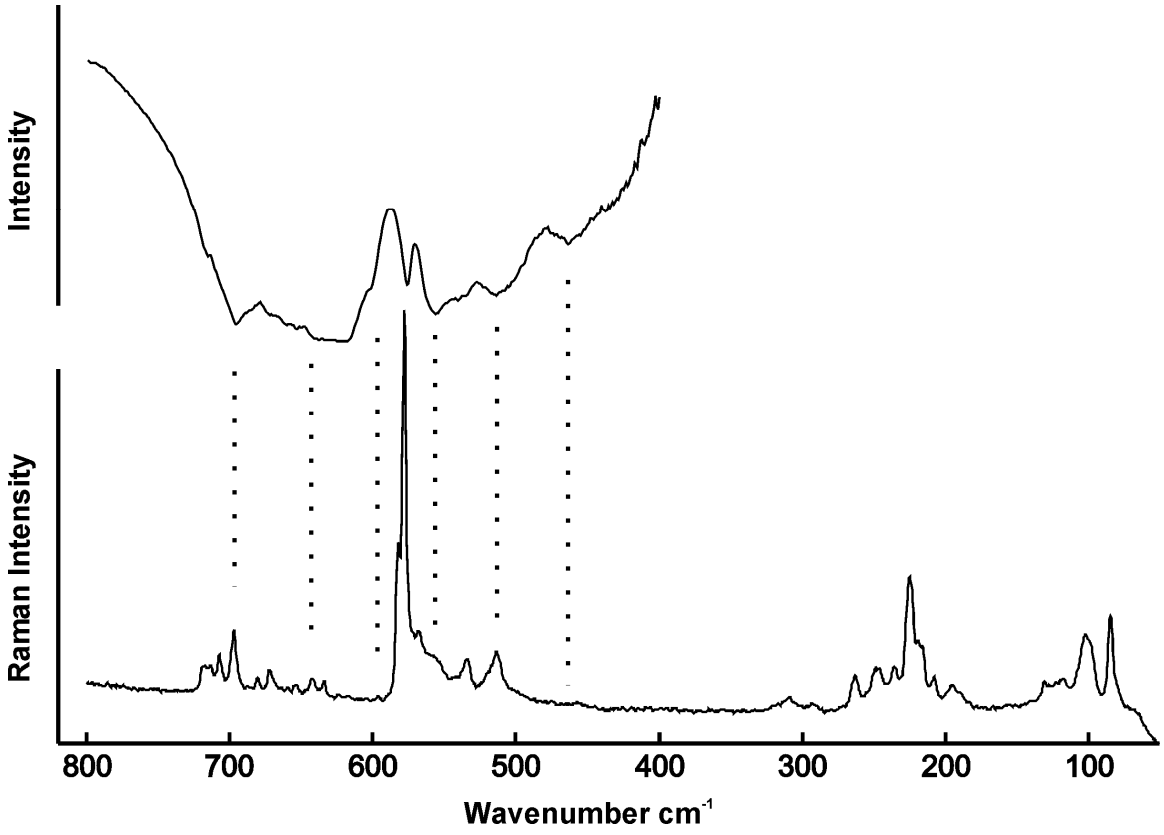

Figure 4.2.2 The vibrational spectra of solid WSF_4. The Raman spectrum (lower trace) was recorded of the neat solid in a m.p. capillary at -100 °C. The infrared spectrum (upper trace) was recorded at room temperature as a KBr pellet.

Table 4.2.4 Vibrational Spectroscopy Data Collected for WSF_4

Frequency,[a] cm^{-1}			
Raman[b]	Infrared[c]		
Solid (-100 °C)	Solid	Literature [1]	Assignment
717 (9)			
707 (9)			
697 (16)			
681 (4)	695 s	699 s	
672 (7)		673 s	$\nu_s(WF_{term})$
659 (2)	660 vw		
654 (3)	653 vw		
642 (5)	637 vw	643 s	
634 (4)	625 vs		
583 (36)			
577 (100)	576 vs	577 s	$\nu(WS)$
557 (7)			
553 (7)	556 vs		
534 (13)		534	$\nu(W\text{-}F_{bridge})$
513 (16)	514 vs	514	
	463 vs		
309 (5)			
291 (3)			
262 (9)			
247 (13)			
235 (13)			
224 (38)			Bending Modes
216 (16)			
208 (9)			
196 (7)			
188 (5)			

[a] Abbreviations denote shoulder (sh), very strong (vs), strong (s), medium (m), weak (w), and very weak (vw). [b] Neat solid in melting point capillary at -100 °C. [c] KBr pellet at room temperature.

4.2.5 Density Functional Theory Calculations of WSF_4

Calculations were performed with Gaussian 98[10] at the B3LYP/LANL2DZ level of theory. The geometry was optimized using calculations to find the minimum energy before frequency calculations were performed. The geometry was not exactly C_{4v} symmetry but was very close; therefore C_{4v} symmetry was assumed for the assignment of the calculated vibrational bands. Tungsten sulfide tetrafluoride is known to exhibit C_{4v} symmetry in the gas phase based on electron-diffraction studies.[11]

The calculated structure for the molecule is shown in Figure 4.2.3 with bond lengths and angles and comparisons to electron diffraction data from the literature[11] listed in Table 4.2.6. The calculated vibrational frequencies with their calculated Raman scattering activities and infrared intensities can be found in Table 4.2.6. The values are compared to the gas phase infrared literature values.[12]

Analysis of Table 4.2.5 indicates that the bond lengths and angles of the calculated monomeric WSF_4 are quite close to those observed for electron diffraction in the gas phase and in the crystal structure of solid polymeric WSF_4 when effects of the bridging fluorine atom are ignored. The W-F bond lengths (Table 4.2.5) are slightly shorter in the crystal structure at with an average terminal W-F bond length of 184.4(6) pm compared to the calculated values of 188.1 and 188.2 pm. The calculated W=S bond distance at 214 pm is also longer than the experimental value 208.8(5) pm as are the calculated S=W-F bond angles. All of these discrepancies can easily be explained by the effects of fluorine bridging in the crystal structure.

It is important to remember that the calculations are representative of the monomeric molecule in the gas phase, hence, a direct comparison between the solid form of WSF_4 and the calculations is difficult. The calculated frequency of the W=S stretching mode is very close at 544 cm^{-1} compared to the observed frequency of 577 cm^{-1}. The terminal tungsten-fluorine bond stretching modes were also quite close indicating the model is a good fit with experiment. The one shortcoming of the above model is its inability to describe or account for the W-F--W bridging modes. The calculations also provide an invaluable tool for visualizing vibrational modes.

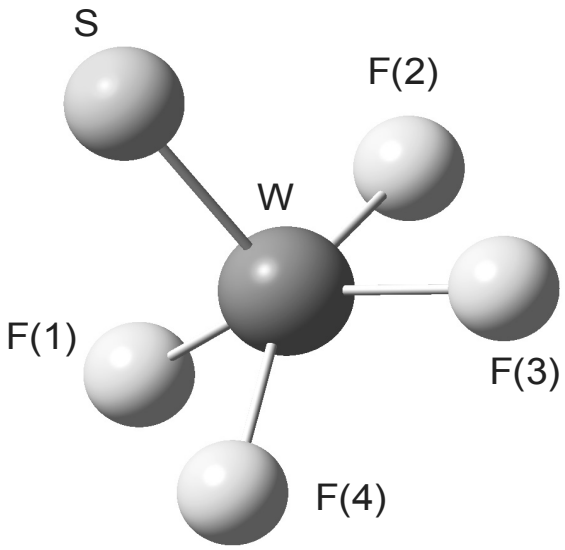

Figure 4.2.3 The calculated geometry of WSF_4 using density functional theory at the B3LYP/LANL2DZ level of theory.

Table 4.2.5 Calculated Bond Distances and Angles for WSF_4 using the B3LYP/LANL2DZ Level of Theory.

Bond Distance, pm			Bond Angle, °		
	Calculated	Electron diffraction[11]		Calculated	Electron diffraction[11]
W – F(1)	188.1		S – W – F(1)	104.25	
W – F(2)	188.2	184.7(3)	S – W – F(2)	103.89	104.5(11)
W – F(3)	188.1		S – W – F(3)	104.23	
W – F(4)	188.2		S – W – F(4)	103.86	
W = S	214	210.4(7)	F(1) – W – F(2)	86.67	
			F(2) – W – F(3)	86.54	86.6(5)
			F(3) – W – F(4)	86.63	
			F(4) – W – F(1)	86.64	

Table 4.2.6 The Calculated Vibrational Frequencies of WSF_4 using the B3LYP/LANL2DZ Level of Theory Compared to Gas-Phase Infrared Data.

Calc. Frequency, cm^{-1}	Raman Activity [a]	Infrared Intensity [a]	Frequency, cm^{-1} Gas-Phase Infrared[12]	Assignment	
692	15	58	707	$\nu_s(WF_4)$	$\nu_2(A_1)$
686	1.2	161	671	$\nu_{as}(WF_4)$	$\nu_7(E)$
614	5	0		$\nu(WF_4)$	$\nu_4(B_1)$
544	21	23	577	$\nu(WS)$	$\nu_1(A_1)$
322	2.6	0		δ	$\nu_6(B_2)$
234	1	8		δ	$\nu_3(A_1)$
231	0	21		$\delta(SWF)$	$\nu_9(E)$
201	6	0		δ	$\nu_8(E)$
123	0	0		δ	$\nu_5(B_1)$

[a]Intensities are in units a^4/amu and km/mole for Raman scattering activity and infrared intensity, respectively.

4.3 Summary

The compound WSF_4 was successfully generated in high purity by an easier and more direct method than was previously known. An improved crystal structure was determined that confirmed the fluorine-bridged chain structure of WSF_4. Tungsten sulfide tetrafluoride was characterized by Raman, infrared, and ^{19}F NMR spectroscopy. Density functional theory calculations for geometry optimization and frequency were performed and compared to the structure obtained from the X-ray crystal structure of WSF_4.

References

(1) Atherton, M. J.; Holloway, J. H. *J. Chem. Soc., Chem. Commun.* **1977**, 424.

(2) Holloway, J. H.; Kaucic, V.; Russell, D. R. *J. Chem. Soc., Chem. Commun.* **1983**, 1079.

(3) Banger, K. K.; Blackman, C. S.; Brisdon, A. K. *J. Chem. Soc., Dalton Trans.* **1996**, 2975

(4) Edwards, A. J. *J. Chem. Soc. A.* **1969**, 909.

(5) Edwards, A. J.; Jones, G. R. *J. Chem. Soc. A.* **1968**, 2074.

(6) Bennett, M. J.; Haas, T. E.; Purdham, J. T. *Inorg. Chem.* **1972**, *11*, 207.

(7) Buslaev, Y. A.; Kokynov, Y. B.; Chubar, Y. D. *Proc. Acad. Sci.* **1973**, *213*, 912.

(8) Gutmann, V. *Coordination Chemistry in Nonaqueous Solutions*; Springer- Verlag: Berlin, 1968.

(9) Beattie, I. R.; Reynolds, D. J. *J. Chem. Soc., Chem. Commun.* **1968**, 1531.

(10) M. J. Frisch, G. W. T., H. B. Schlegel, G. E. Scuseria, M. A. Robb, J. R. Cheeseman, V. G. Zakrzewski, J. A. Montgomery, Jr., R. E. Stratmann, J. C. Burant, S. Dapprich, J. M. Millam, A. D. Daniels, K. N. Kudin, M. C. Strain, O. Farkas, J. Tomasi, ; V. Barone, M. C., R. Cammi, B. Mennucci, C. Pomelli, C. Adamo, S. Clifford, J. Ochterski, G. A. Petersson, P. Y. Ayala, Q. Cui, K. Morokuma, D. K. Malick, A. D. Rabuck, K. Raghavachari, J. B. Foresman, J.,Cioslowski, J. V. Ortiz, A. G. Baboul, ; B. B. Stefanov, G. L., A. Liashenko, P. Piskorz, I. Komaromi, R. Gomperts, R. L. Martin, D. J. Fox, T. Keith, M. A. Al-Laham, C. Y. Peng, A. Nanayakkara, M. Challacombe, P. M. W. Gill, B. Johnson, W. Chen, M. W. Wong, J. L. Andres, C. Gonzalez, M. Head-Gordon, E. S. Replogle, and J. A. Pople; Gaussian, Inc: Pittsburgh PA, 1998.

(11) Rice, D. A.; Hagen, K.; Hedberg, L.; Hedberg, K.; Staunton, G. M.; Holloway, J. H. *Inorg. Chem.* **1984,** *23,* 1826.

(12) Jones, P. J.; Levason, W.; Ogden, J. S.; Turff, J. W. *J. Chem. Soc., Dalton Trans.* **1983**, 2625.

Chapter 5

Lewis-Acid Chemistry of WSF_4

5.1 Introduction

The fluoride-ion affinity of WF_6 and WOF_4 has been studied extensively. Tungsten sufide tetrafluoride has received relatively little attention in that regard. The thiotetrafluorotungstate (VI), WSF_5^-, anion has been observed by ^{19}F NMR, as side products of reactions to produce WSF_4 in solution[1,2] and by X-ray crystallography.[4] Solution-state reactions have also tended to produce the larger $W_2S_2F_9^-$ anion in addition to WSF_4 and WSF_5^- as observed by ^{19}F NMR spectroscopy. This behaviour is analogous to reactions of the tungsten oxide fluorides. For reactions in CH_3CN it was postulated that the formation of anions might be a result of its poor solvating ability toward the F^- anion.[3]

5.2 Results and Discussion

5.2.1 Synthesis of $[N(CH_3)_4][WSF_5]$ and Generation of $W_2S_2F_9^-$ and $W_2OSF_9^-$ Anions

Reaction between WF_6 and $[N(CH_3)_4][SSi(CH_3)_3]$ in tetrahydrofuran (THF) solvent (Equation 5.2.1) yielded the new $[N(CH_3)_4][WSF_5]$ salt with minor impurities as a homogeneous pink powder. The sample was characterized by ^{19}F NMR spectroscopy in CH_3CN solvent and vibrational spectroscopy in the solid state.

$$[N(CH_3)_4][SSi(CH_3)_3] + WF_6 \xrightarrow[-78\ °C]{THF} [N(CH_3)_4][WSF_5] + (CH_3)_3SiF \qquad 5.2.1$$

Upon mixing of the reactants the solution immediately became yellow. With continued agitation the solution eventually turned red. The red solution was stable at room temperature with no signs of decomposition and could be kept for weeks reliably in FEP outside of the dry box at room temperature. Fluorine-19 NMR spectroscopy of an orange-coloured solution, harvested in mid-reaction, showed a mixture of WSF_4 and

WSF_5^-. Therefore, it was postulated that WSF_4 was generated quickly, present as the WSF_4·THF adduct in yellow solutions which slowly formed WSF_5^- as the THF ligand was replaced by F^- on WSF_4. Larger-scale reactions in a ¾" FEP reactor indicated that excess WF_6 needed to be avoided since $[N(CH_3)_4][WF_7]$ was readily formed. Excess amounts of WF_6 were also thought to cause polymerization of THF. Cooling the reaction mixture to -78 °C seemed to prevent polymerization of the solvent.

Re-crystallization of pink $[N(CH_3)_4][WSF_5]$ was attempted from CH_2Cl_2. Slow removal of the CH_2Cl_2 resulted in a white/pale yellow powder. The powder was characterized by Raman spectroscopy as $[N(CH_3)_4][WSF_5]$ with less fluorescence than found for the pink, impure $[N(CH_3)_4][WSF_5]$ (Table 5.2.2). Hence, dissolution of $[N(CH_3)_4][WSF_5]$ in CH_2Cl_2 followed by removal of volatiles serves as a method of purification.

The ability to produce WSF_4 on a preparative scale allowed for the alternative synthesis of $[N(CH_3)_4][WSF_5]$ by stoichiometric combination of $[N(CH_3)_4][F]$ and WSF_4 in CH_3CN solvent (Equation 5.2.2). The reaction resulted in a yellow solution with a white solid; the white solid was presumed to be $[N(CH_3)_4][WSF_5]$ that was unable to dissolve in the solvent as saturation had been reached. Fluorine-19 NMR spectroscopy of the solution showed the presence of the WSF_5^- anion, as the only product.

$$[N(CH_3)_4][F] + WSF_4 \xrightarrow{CH_3CN} [N(CH_3)_4][WSF_5] \qquad 5.2.2$$

The difference in appearance of $[N(CH_3)_4][WSF_5]$ from two different syntheses indicated that the red colour was likely from the presence of a small amount of organic impurities that formed upon oxidative decomposition of THF solvent. This was confirmed by the presence of a very small resonance in the ^1H NMR spectrum of the pink solid dissolved in CH_3CN at 12.4 ppm corresponding to the formation of a carboxylic acid.

Initially, the reaction between WF_6 and $[N(CH_3)_4][SSi(CH_3)_3]$ in CH_3CN solvent to prepare pure $[N(CH_3)_4][WSF_5]$ was attempted, but resulted in red/yellow/brown mixtures of WSF_4, WSF_5^-, $W_2S_2F_9^-$ and large amounts of insoluble brown solids. Lower concentrations and temperatures of –35 °C did not prevent the side reactions from

occurring. Another aprotic, polar solvent with a lower freezing point than CH_3CN in which the products were soluble, such as THF, was necessary to control the reactions.

The formation of $W_2S_2F_9^-$ anions was the result of the combination of WSF_4 and WSF_5^- in CH_3CN (Equation 5.2.4)

$$WSF_4 + WSF_5^- \overset{CH_3CN}{\leftrightarrows} W_2S_2F_9^- \qquad 5.2.3$$

Reaction of $[N(CH_3)_4][F]$ and WSF_4 in a 1:2 ratio forms primarily $W_2S_2F_9^-$ in CH_3CN. The $W_2S_2F_9^-$ anion was in equilibrium with WSF_4 and WSF_5^-, as both WSF_4 and WSF_5^- were present in the ^{19}F NMR spectrum though the equilibrium clearly lies to the right for Equation 5.2.3.

Tungsten sulfide fluorides are extremely sensitive toward moisture resulting in hydrolysis of the sulfide group on tungsten. A small amount of hydrolysis occurred in the NMR sample generating WOF_4 and WOF_5^-. The $W_2O_2F_9^-$ anion was gave rise to a very small ^{19}F resonance while the novel mixed oxo-sulfido anion $W_2OSF_9^-$ was readily observed (Table 5.2.1). It is evident that WOF_4 is a stronger Lewis acid than WSF_4 as no WOF_4 was detected in solution by ^{19}F NMR spectroscopy. Like the reaction between WSF_5^- and WSF_4 the mixed $W_2OSF_9^-$ anion is formed in equilibrium with WOF_5^- and WSF_4 (Equation 5.2.4).

$$WOF_5^- + WSF_4 \overset{CH_3CN}{\leftrightarrows} W_2OSF_9^- \qquad 5.2.4$$

Analogous reactions with $[Cs][SSi(CH_3)_3]$ and WF_6 in THF were attempted. A yellow solution which turned red/brown in colour upon agitation was observed. Polymerization of THF occurred, even at –78 °C, indicating the solution was not stable. When THF solvent was removed quickly to prevent polymerization, the ^{19}F NMR spectrum of the resulting brown powder dissolved in CH_3CN showed WF_7^- and WSF_5^-. The poor solubility of the $Cs[SSi(CH_3)_3]$ salt in THF meant that excess WF_6 was present in solution to participate in Equation 5.2.5 to form the WF_7^- anion as well as catalyze THF polymer formation.

$$2\ WF_6 + [SSi(CH_3)_3]^- \xrightarrow{THF} [WF_7]^- + WSF_4 + (CH_3)_3SiF \qquad 5.2.5$$

Tetrahydrofuran has been observed to polymerized via a cationic mechanism where the propagating species is an oxonium ion.[7] In this case, however, no cations were available to initiate the reaction. It could be that the strong Lewis-acidic character of WF_6 was instead sufficiently electron-withdrawing to cause pseudo-oxonium ion propagation leading to polymer formation.

5.2.2 NMR Spectroscopy

The $[N(CH_3)_4][WSF_5]$ salt was characterized by ^{19}F NMR spectroscopy in CH_3CN and THF solvents. The NMR parameters are listed in Table 5.2.1.

Fluorine-19 NMR spectroscopy of $[N(CH_3)_4][WSF_5]$ (Figure 5.2.1-2) dissolved in CH_3CN showed a doublet attributed to WSF_5^- at +77.2 ppm with $^2J(^{19}F\text{-}^{19}F)$ coupling of 75.5 Hz and $^1J(^{19}F\text{-}^{183}W)$ satellites (28.34 Hz). The corresponding quintet with the same $^2J(^{19}F\text{-}^{19}F)$ coupling was centered at –111.3 ppm. Small ^{183}W-satellites were visible with $^1J(^{19}F\text{-}^{183}W)$ = 68.6 Hz. The hydrolysis product WOF_5^- was observed as a doublet with ^{183}W-satellites at +47.2 ppm($^2J(^{19}F\text{-}^{19}F)$ = 52.5 Hz and $^1J(^{19}F\text{-}^{183}W)$ = 71.0 Hz) and a quintet at –82.7 ppm.

The ^1H NMR spectrum of $[N(CH_3)_4][WSF_5]$ dissolved in CH_3CN showed a singlet at +3.25 ppm attributable to $[N(CH_3)_4]^+$. The ^{19}F NMR spectrum of $[Cs][WSF_5]$ in CH_3CN was very similar to that of $[N(CH_3)_4][WSF_5]$ with a doublet and quintet at chemical shifts of +77.9 and –111.7 ppm, respectively. Tungsten-183 satellites were observed with $^1J(^{19}F\text{-}^{183}W)$ coupling constants of 28.6 and 59.3 Hz for F_{eq} and F_{ax}, respectively. The ^{19}F NMR signal at +143.5 ppm also indicated that significant amounts of WF_7^- were present in the sample.

In the literature conflicting reports can be found about the ^{19}F chemical shifts of WSF_5^-.[1,2,4] Buslaev *et al.*[1] assigned a doublet at +80.0 ppm and a quintet at -141.5 ppm in the ^{19}F NMR spectrum to WSF_5^- in solution. Their assignment of the quintet to -141.5 ppm is in contrast with our observation (-111.35 ppm). The ^{19}F NMR spectrum of $[Na(15\text{-crown-}5)][WSF_5]$ was reported as the doublet at -62.8 ppm and the quintet at -116.2 ppm in CD_3CN solvent.[4] The chemical shift for the doublet is in disagreement

with the chemical shifts observed in this work and in other literature previously mentioned. The $^{2}J(^{19}F\text{-}^{19}F)$ coupling constants reported for WSF_5^- by Buslaev *et al.*[1] and Hilbers *et al.*[4] were 74 and 75.6 Hz, respectively, in accordance with our value of 75.5 Hz.

Fluorine-19 NMR spectroscopy of $[N(CH_3)_4][W_2S_2F_9]$ showed a doublet centered at +85.6 ppm and a nonet centered at –156.5 ppm (Figures 5.2.3, 5.2.5). Tungsten-183 satellites for $F_{terminal}$ and $F_{bridging}$ atoms were resolved on both signals with coupling constants of 31.3 and 83.9 Hz, respectively. The chemical shifts and $^{2}J(^{19}F\text{-}^{19}F)$ coupling constant of 70.0 Hz are in accordance with those previously reported in the literature.[1,2]

A complex multiplet (Figure 5.2.6), derived from a quintet split into quintets by secondary coupling, with ^{183}W satellites, was centered at -148.1 ppm. The multiplet is attributed to the new $W_2OSF_9^-$ anion. The bridging fluorine atom in $W_2OSF_9^-$ is coupled to two sets of four fluorine atoms generating an A_4B_4X spin system. The $^{2}J(^{19}F\text{-}^{19}F)$ couplings 57 and 70 Hz are assigned to the WOF_4 and WSF_4 moieties, respectively. The $^{2}J(^{19}F\text{-}^{19}F)$ couplings to each set of fluorine atoms was the same or very close to those observed for $W_2O_2F_9^-$ and $W_2S_2F_9^-$ anions. The same couplings were observed in a doublet centered at +86.0 ppm (Figure 5.2.3) and a doublet centered at +60.8 ppm (Figure 5.2.4). Tungsten-183 satellites were resolved about the doublet at +60.8 ppm giving a $^{1}J(^{19}F_{W=O}\text{-}^{183}W)$ coupling of 71.0 Hz in good agreement with $^{1}J(^{19}F\text{-}^{183}W)$ observed in the oxide fluorides. Other tungsten satellites for the doublet at +86.0 ppm and the multiplet could not be resolved fully due to overlap with the doublet arising from the terminal fluorine environment in $W_2S_2F_9^-$, though $^{1}J(F_{W=S}\text{-}^{183}W)$ coupling could be estimated at between 16 and 19 Hz.

Fluorine-19 NMR spectroscopy of reactions of $[N(CH_3)_4][SSi(CH_3)_3]$ with excess WF_6 (Equation 5.2.3) dissolved in CH_3CN revealed that WF_7^- is stable with respect to $WSF_4 \cdot CH_3CN$ in solution and does not donate a fluoride to WSF_4 indicating WF_6 is a stronger Lewis acid than WSF_4.

Combinations of $[N(CH_3)_4][WSF_5]$ and pyridine showed no sign of Lewis adduct formation by Raman or ^{19}F NMR spectroscopy, even at –40°C, indicating that WSF_5^- does not possess significant Lewis-acid character.

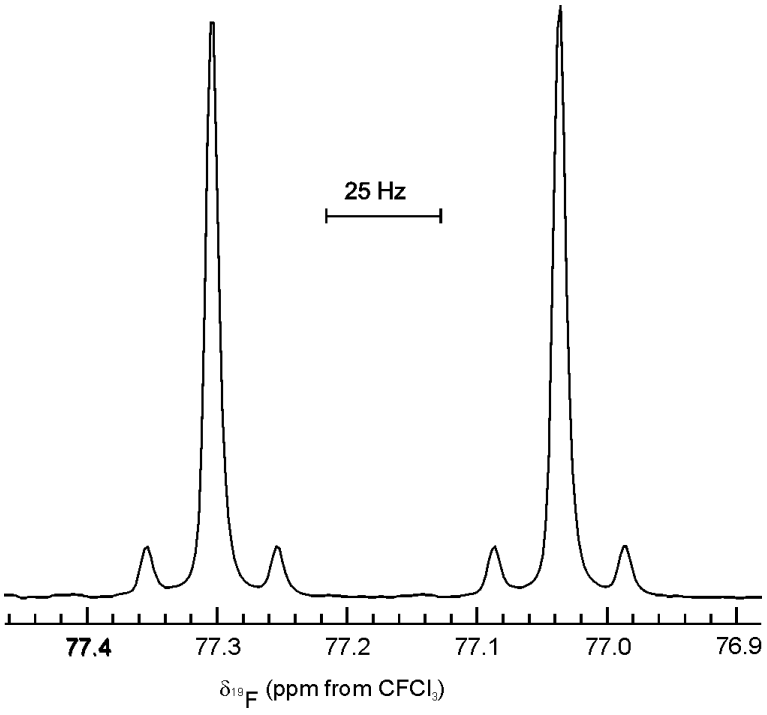

Figure 5.2.1 The ^{19}F NMR spectrum of equatorial fluorine atoms of the WSF_5^- anion in CH_3CN at room temperature.

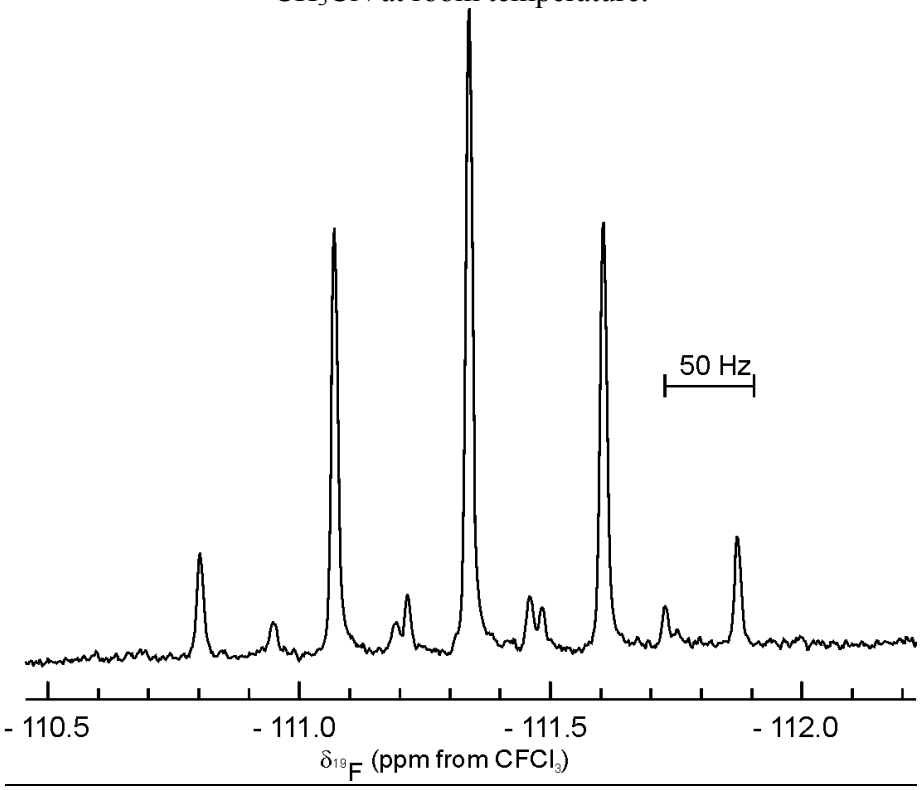

Figure 5.2.2 The ^{19}F NMR spectrum of the axial fluorine atom of the WSF_5^- anion in CH_3CN at room temperature.

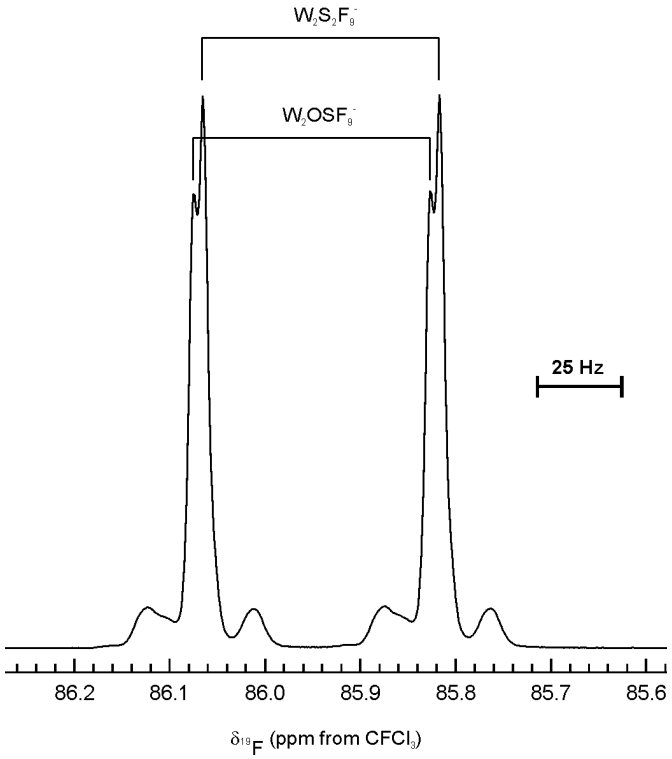

Figure 5.2.3 The ^{19}F NMR spectrum of the terminal-fluorine atoms of $W_2S_2F_9^-$ and the W=S portion of $W_2SOF_9^-$ anions overlapped.

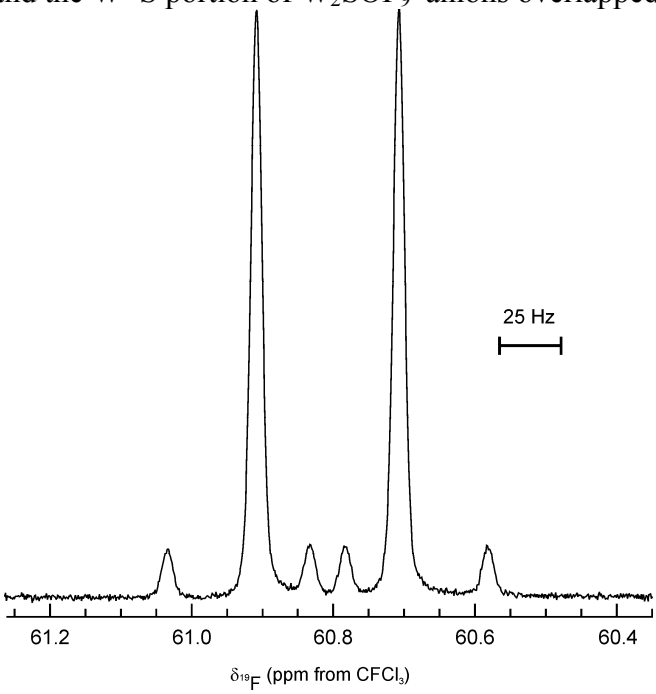

Figure 5.2.4 The ^{19}F NMR spectrum of the terminal-fluorine atoms of the W=O portion of the $W_2SOF_9^-$ anion in CH_3CN at room temperature.

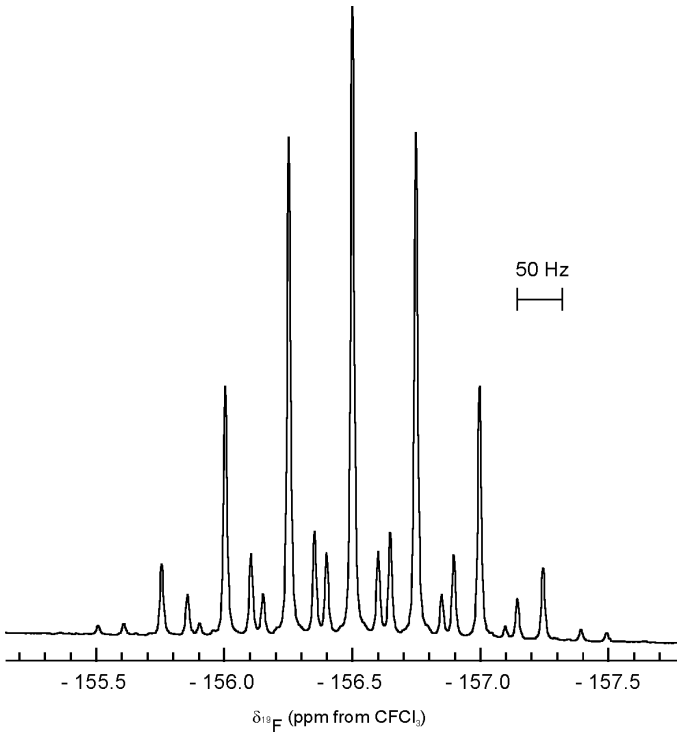

Figure 5.2.5 The ^{19}F NMR spectrum of the bridging-fluorine atom in the $W_2S_2F_9^-$ anion in CH_3CN at room temperature.

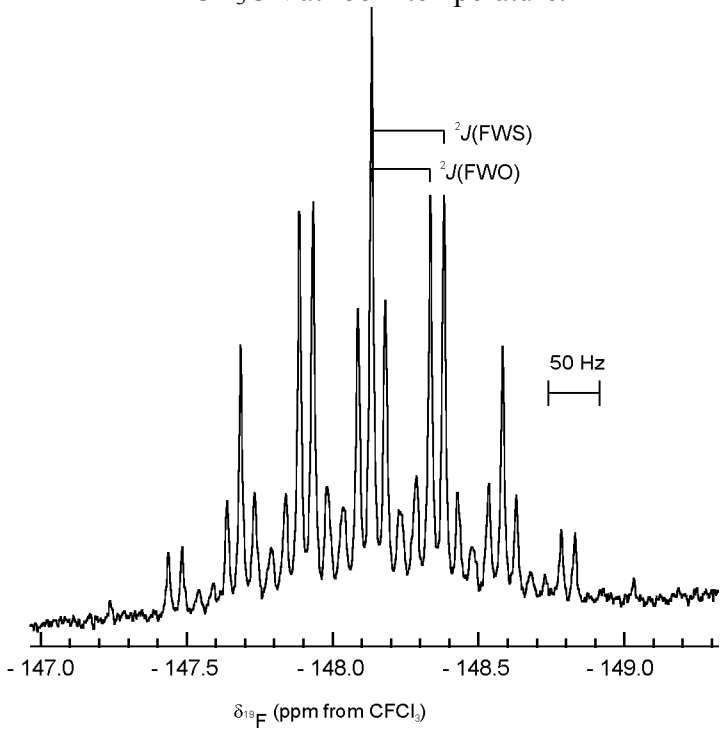

Figure 5.2.6 The ^{19}F NMR spectrum of the bridging-fluorine atom of the $W_2SOF_9^-$ anion in CH_3CN at room temperature.

Table 5.2.1 ^{19}F NMR Spectroscopy Data for WSF_5^-, $W_2S_2F_9^-$ and $W_2OSF_9^-$ Anions

Chemical shift [a,] (ppm)	Solvent	$^1J(^{19}F\text{-}^{183}W)$ (Hz)	$^2J(^{19}F\text{-}^{19}F)$ (Hz)	Assignment
77.15 (d)	CH_3CN	28.3 (F_{eq})	75.5	WSF_5^-
-111.35 (qn)		68.6 (F_{ax})		
47.2 (d)	CH_3CN	71.0 (F_{eq})	52.2	WOF_5^-
-82.7 (qn)		62 (F_{ax})		
79.0 (d)	THF	28.2 (F_{eq})	76.0	WSF_5^-
-111.8 (qn)		68.6 (F_{ax})		
85.6 (d)	CH_3CN	31.3 (F_{eq})	70.0	$W_2S_2F_9^-$
-156.5 (n)		83.9 (F_{bridge})		
61.8 (d)	CH_3CN		58.4	$W_2O_2F_9^-$
86.0 (d)	CH_3CN	16-19 (F_{eq}, WS)	70 (WS)	$W_2OSF_9^-$
60.8 (d)		71.0 (F_{eq}, WO)	56.7 (WO)	
-148.1 (qn/qn)				

[a] Abbreviations denote doublet (d), quintet (qn), nonet (n), and quintet of quintets (qn/qn).

5.2.3 Vibrational Spectroscopy of $[N(CH_3)_4][WSF_5]$

Raman and infrared spectra of $[N(CH_3)_4][WSF_5]$ were recorded. The vibrational frequencies together with their assignments are listed in Table 5.2.2.

The WSF_5^- anion was expected to exhibit C_{4v} symmetry according to calculations (Section 5.2.4) like monomeric WSF_4 (see Chapter 4) and $MoSF_4$ (see Chapter 6). Under group theoretical treatment all vibrations span the reducible representation $\Gamma_{vib} = 4\ A_1 + 2\ B_1 + B_2 + 4\ E$. The stretching modes form a basis for $\Gamma_{stretch} = 3\ A_1 + B_1 + E$ leaving the bending modes to $\Gamma_{bend} = A_1 + B_1 + B_2 + 3\ E$. All vibrational modes are Raman active while only A_1 and E are infrared active. The calculated vibrations (Section 5.2.4) and actual experimental vibrations in Table 5.2.2 were described by the applied symmetry. Vibrational bands of the solid phase may be split by crystallographic symmetry requirements causing direct correlation of data to be difficult.

The Raman spectrum collected on the pink solid, $[N(CH_3)_4][WSF_5]$, corresponds reasonably well to the calculated values with the exception of several smaller bands that could have been the result of crystallographic symmetry requirements.

Some small bands disappeared from the Raman spectrum when $[N(CH_3)_4][WSF_5]$ was dissolved in CH_2Cl_2 though the major bands remained. A significant drop in the intensity of the W-F_{ax} stretching band at 473 cm^{-1} coupled with the lack of any new bands indicates that CH_2Cl_2 did not react with WSF_5^-, instead it separated the anion from THF polymer impurities.

The $\nu_s(WF_4)$ and $\nu(W{=}S)$ bands observed in the Raman spectrum and the $\nu_s(WF_4)$, $\nu_{as}(WF_4)$, $\nu(W{=}S)$ and $\nu(W\text{-}F_{ax})$ observed in the infrared spectrum of [Na(15-crown-5)][WSF_5][4] (Table 5.2.2) agree well with the strong bands observed in the Raman spectrum of $[N(CH_3)_4][WSF_5]$ (Figure 5.2.7). The splitting of the W=S stretch into two bands indicates that distortion of the WSF_5^- anion reduces the symmetry to less than C_{4v} symmetry in solid $[N(CH_3)_4][WSF_5]$.

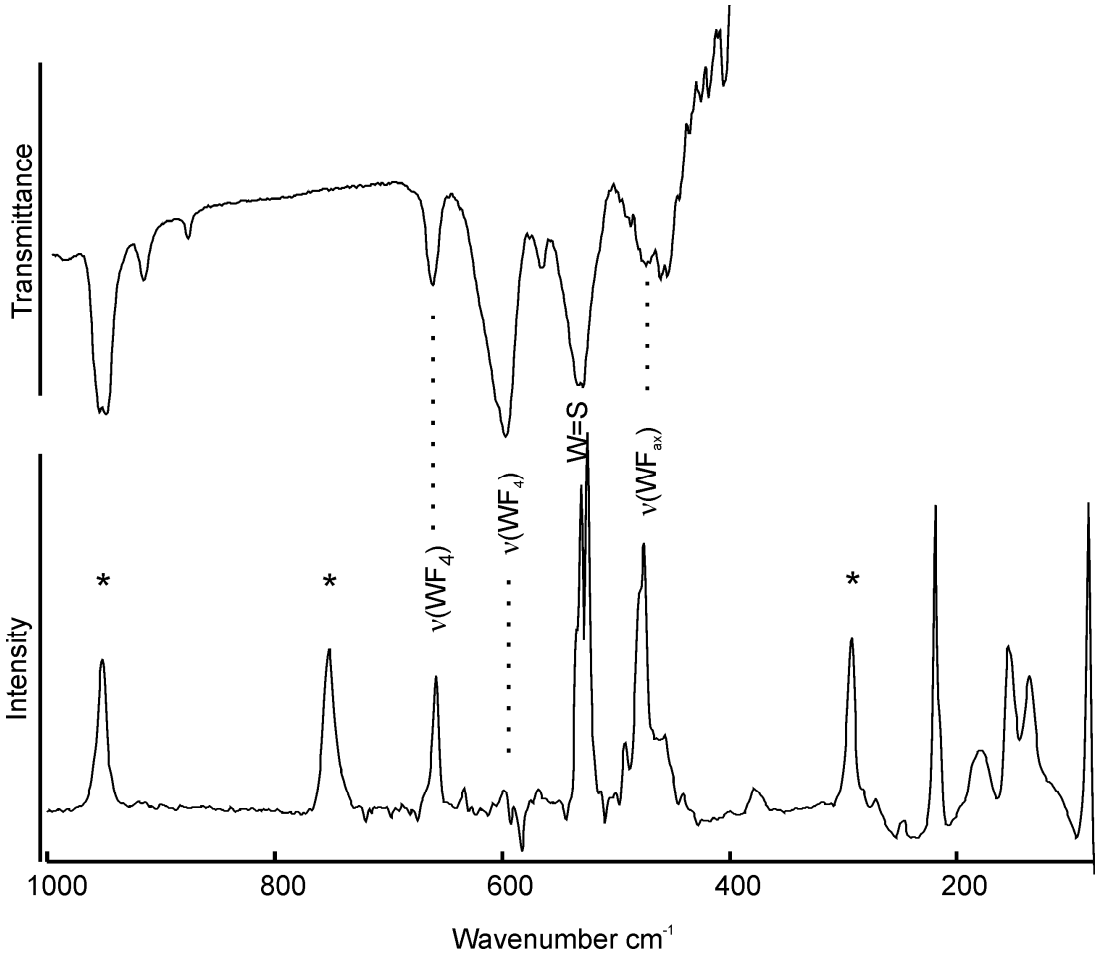

Figure 5.2.7 Vibrational spectroscopy of solid $[N(CH_3)_4][WSF_5]$ collected at room temperature. The Raman spectrum (lower trace) was recorded on the neat powder in glass melting point capillary. The infrared spectrum (upper trace) was collected as a KBr pellet. Asterisks (*) denote bands attributable to $[N(CH_3)_4]^+$.

Table 5.2.2 Vibrational Spectroscopy of Solid $[N(CH_3)_4][WSF_5]$ Compared to Calculations and Values for [Na(15-crown-5)][WSF_5]

Frequency,[a] cm^{-1}						Assignment
$[N(CH_3)_4][WSF_5]$			[Na(15-crown-5)] $[WSF_5]$[4]			WSF_5^-
Raman [b,c]	Raman [b]	Infrared[d]	Raman	Infrared	Calc.[e]	
pink solid from reaction in THF	white solid recrystallized from CH_2Cl_2	pink solid				
658 (38)	657 (28)	662 s	662 m	662 s	643 [78]	$\nu_s(WF_4)$, A_1
597 (10)		597 vs		607 vs	628 [218]	$\nu_{as}(WF_4)$, E
567 (3)		566 w			566 [0]	$\nu(WF_4)$, B_1
530 (86)	531 sh	529 s			542 [133]	
524 (100)	524 (100)		525 vs	526 s	471 [39]	$\nu(W=S)$, A_1
491 (21)						Impurity
474 (72)	473 (41)	473 m		472 s		$\nu(SWF_{ax})$,A_1
456 (21)	456 (18)	458 m				
440 (7)						Impurity
377 (7)	378 (4)					Impurity
292 (41)	292 (40)				285 [5.5]	$\delta_{scis}(WSF_3)$E
246 (7)					279 [17]	Impurity
219 (83)	221 (79)				272 [0]	$\delta_{scis}(WF_4)$, B_2
182 (14)	177 (22)				207 [29]	δ, E
155 (34)	153 (59)				202 [0]	$\delta_{out\text{-}of\text{-}plane}$
137 (21)	134 (22)				109 [0.2]	$\delta_{wag}(WSF_3)$, E

[a] Abbreviations denote shoulder (sh), very strong (vs), strong (s), medium (m), weak (w), very weak (vw), [b] Neat solid in melting point capillary at room temperature. [c] Vibrations attributable to $[N(CH_3)_4]^+$ not shown were at 3033 (27), 2981 (16), 2962 (20), 2930 (21), 2831 (7), 2819 (7), 1476 (19), 1465 (22), 1460 (25), 1417 (6),1176 (6), 950 (34), 917 (7), 752 (34) cm^{-1}. [d] KBr pellet at room temperature.[e] Calculated infrared intensities were included.

5.2.4 Density Functional Theory Calculations for WSF_5^-

Geometry optimization was performed using the B3LYP/LANL2DZ level of theory to optimize the molecular geometry and calculate the vibrational frequencies of WSF_5^-.

The bond lengths of the geometry optimized anion (Table 5.2.3) are longer than those observed for WSF_4 as expected due to the increased electron density about the tungsten from the addition of a fluoride. The fluoride coordinates *trans* to the sulfur atom with the W–F_{ax} bond distance, greater than the W-F_{eq} distance because of the *trans*-effect. The calculated difference is just under 5.5 pm, which is a reasonably small amount that is reflected in the close proximity of the calculated W–F_{eq} and W–F_{ax} stretching bands. When the calculated bond lengths and angles are compared to literature[4] values it is found that the W=S bond is calculated to be much longer than the observed bond length of 212.3(1) pm. The calculated W-F_{eq} and W-F_{ax} bond lengths are quite close to the experimental values for W-F_{ax} (196.3(3) pm) and W-F_{eq} (ranging from 185.4(3) to 188.9(3) pm).

The calculated W=S bond length is 7 pm longer than that calculated for WSF_4. As a result, the calculated W=S stretching vibration for WSF_5^- (Table 5.2.3) was significantly lower than the calculated value for WSF_4 (544 cm^{-1}). The addition of the fluoride *trans* to the sulfur atom would be expected to weaken the W=S bond in accordance with the decreased frequency provided from the calculations. Stretching bands close to the calculated value of 471 cm^{-1} for W=S stretching were observed in the vibrational spectrum of the solid (Table 5.2.2). This is not in line with calculated Raman activities, as the strongest band in the Raman spectrum is at 524 cm^{-1} not 473 cm^{-1} and the W=S stretch would be the most polarizable bond in the system generating the strongest signals in the Raman spectrum. The observed vibrational bands contained many similar frequencies to the calculated bands but the assignment of strong bands was different.

The equatorial fluorine atoms still form a plane below the tungsten atom, though not as pronounced as for the calculated WSF_4 molecule. The addition of the fluoride changed the S=W–F_{eq} angle from *ca.* 104 ° to 95.7 °. The presence of the fluoride also increased the energy of the calculated out-of-plane WF_4 (B_1) bending mode quite

considerably from *ca.* 120 to 202 cm^{-1} while the calculated in-plane WF_4 (B_2) bending mode dropped in energy considerably from 322 to 272 cm^{-1}. The WF_4 (A_1) bending mode increased in energy while the WF_4 (A_1) stretching modes decreased in energy. The WF_4 (E) bending modes maintained similar energies while the WF_4 (E) stretching mode decreased in energy somewhat.

In Table 5.2.3 the calculated data is shown to fit the observed X-ray data very closely. All calculated angles and bond lengths are either slightly larger than or matching to what was observed by Hilbers *et al.*[4]

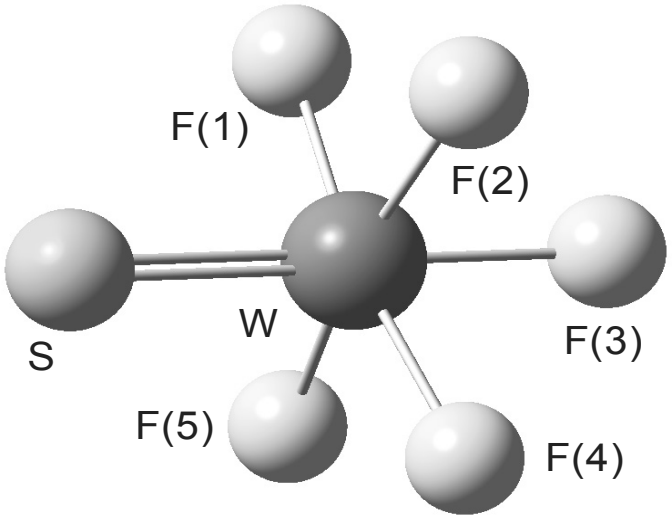

Figure 5.2.8 The calculated geometry of the WSF_5^- anion using density functional theory at the B3LYP/LANL2DZ level of theory.

Table 5.2.3 Calculated Bond Lengths and Angles for the WSF_5^- Anion Compared to Values from the X-ray Crystal Structure.

Bond Lengths, pm			Bond Angles, °		
	Calc	X-ray[4]		Calc.	X-ray[4]
W–F(1)	191.47	188.9(3)	$S=W–F_{eq}$	95.7	95.4 - 97.4
W–F(2)	191.48	188.6(2)	$S=W–F_{ax}$	179.9	178.1
W–F(3)	196.93	196.3(3)	$F_{eq}–W–F_{ax}$	84.3	83.4 - 85.1
W–F(4)	191.47	185.4(3)	$F_{eq}–W–F_{eq}$	89.4	88.8 -91.9
W–F(5)	191.48	186.3(2)			
W=S	221.00	212.3(1)			

Table 5.2.4 Calculated Vibrations for WSF_5^- Anion using Density Functional Theory at the B3LYP/LANL2DZ Level of Theory

Frequency, cm^{-1}	Raman Activity[a]	Infrared Intensity[a]	Assignment	
643	19	78	$\nu_s(WF_{4eq})$	$\nu_3(A_1)$
628	0	218	$\nu_{as}(WF_{4eq})$	$\nu_8(E)$
566	5	0	$\nu(WF_{4eq})$	$\nu_5(B_1)$
542	1	133	$\nu(WF_{ax})$,	$\nu_2(A_1)$
471	27	39	ν(WS),	$\nu_1(A_1)$
285	5	5.5	δ(FWS)	$\nu_9(E)$
279	1	17	$\delta_s(WF_4)$	$\nu_4(A_1)$
272	3	0	$\delta_{in\text{-}plane}$	$\nu_7(B_2)$
207	1	29	δ	$\nu_{11}(E)$
202	0	0	$\delta_{out\text{-}of\text{-}plane}$	$\nu_6(B_1)$
109	1.3	0	δ	$\nu_{10}(E)$

[a] Raman Intensity is in units a^4/u and Infrared intensity is in km/mole

5.3 The $WSF_4 \cdot C_5H_5N$ Lewis Adduct

5.3.1 Synthesis of $WSF_4 \cdot C_5H_5N$

Brown WSF_4 dissolved in pyridine resulting in a distinctly orange solution upon formation of the $WSF_4 \cdot C_5H_5N$ adduct (Equation 5.3.1). A Raman spectrum was collected of both, dilute and very concentrated solutions.

$$WSF_4 + C_5H_5N \rightarrow WSF_4 \cdot C_5H_5N \qquad 5.3.1$$

The $WSF_4 \cdot C_5H_5N$ adduct was soluble in CH_3CN yielding an orange solution, which was studied by ^{19}F NMR spectroscopy. The $WSF_4 \cdot C_5H_5N$ adduct also formed in anhydrous HF solvent as evidenced by the deep orange colour of the solution. Pyridine was vacuum transferred onto a pale yellow HF solution with brown insoluble WSF_4 at the bottom. Upon warming to –80°C the HF solution instantly became a much deeper yellow. Melting of C_5H_5N at –42°C resulted in two separate layers with C_5H_5N above HF. With agitation the C_5H_5N became orange/yellow while the HF remained yellow. With more vigorous agitation the C_5H_5N mixed with HF and large amounts of heat were given off indicating reaction between HF and C_5H_5N. The solution was frozen at –30°C well above the freezing points of HF or C_5H_5N at -83°C and -42°C, respectively. and the solvent could not be removed under dynamic vacuum indicating a significant change to the solvent had occurred. The addition of HF likely protonated the C_5H_5N resulting in the formation of an ionic liquid $[C_5H_5NH][HF_2]$.

5.3.2 ^{19}F NMR Spectroscopy of $WSF_4 \cdot C_5H_5N$

The pyridine adduct of WSF_4 was characterized by ^{19}F NMR spectroscopy in CH_3CN solvent. The chemical shift of 81.8 ppm and $^1J(^{19}F\text{-}^{183}W)$ of 26.8 Hz are in line with the NMR values observed for WSF_4 in the donor solvents THF and CH_3CN. In the case of WOF_4 it was noted by ^1H and ^{19}F NMR spectroscopy that $WOF_4 \cdot C_5H_5N$ would coordinate with another C_5H_5N to become $WOF_4 \cdot 2C_5H_5N$ at temperatures below 0 °C.[5,6] Upon addition of a second C_5H_5N ligand, the fluorine atoms were no longer equivalent instead becoming an A_2MX spin-system. Fluorine-19 NMR spectra were collected of

$WSF_4 \cdot C_5H_5N$ with excess pyridine in CH_3CN. Spectra were collected at –20, -30 and –40 °C and all showed signals for WSF_4 as a singlet, indicating that WSF_4 was either unable to coordinate two pyridine ligands or the ligands were still fluxional at this temperature. Considering that the A_2MX spin-system of $WOF_4 \cdot 2C_5H_5N$ was observable at 0 °C and -40 °C is close to both the freezing points of C_5H_5N and CH_3CN, it is likely that either a second C_5H_5N does not coordinate to WSF_4 or that the $WSF_4 \cdot 2C_5H_5N$ adduct is fluxional.

5.3.3 Raman Spectroscopy of $WSF_4 \cdot C_5H_5N$

The pyridine adduct of WSF_4 was studied by Raman spectroscopy. The observed Raman bands in concentrated pyridine solution and as a solid are listed in Table 5.3.1 together with the Raman bands of neat pyridine and the tentative vibrational assignments.

The Raman spectra of the concentrated solution and the solid showed bands at 673 and 539 cm^{-1} attributable to terminal W-F and W=S stretching modes, respectively. The emergence of a vibrational band at 1015 cm^{-1} was observed in the Raman spectrum of the concentrated solution. The Raman spectrum of solid (Figure 5.3.1) $WSF_4 \cdot C_5H_5N$ was also observed to contain this band except in this case it was the second strongest band in the spectrum. Based on the Raman spectrum of $WOF_4 \cdot C_5H_5N$ from the literature[5] the band at 1015 cm^{-1} is assigned to the in-plane ring deformation which appears at 1030 cm^{-1} in free pyridine. The electron-withdrawing effect of the Lewis acid WSF_4 on a strong pyridine deformation peak clearly indicates that the $WSF_4 \cdot C_5H_5N$ adduct was formed. In $WOF_4 \cdot C_5H_5N$ the band was reported at 1020 cm^{-1}.[5]

The W=S stretch was shifted to 539 cm^{-1} compared to 577 cm^{-1} in solid WSF_4. An even lower frequency was observed for the WSF_5^- anion (524 cm^{-1}). The W=O stretch of $WOF_4 \cdot C_5H_5N$ was shifted to 996 cm^{-1} from 1053 cm^{-1} in WOF_4.[5]

Terminal W-F stretches are found at 673 cm^{-1} in the Raman spectrum of the solid (Figure 5.3.1) compared to *ca.* 700 cm^{-1} in WSF_4. Only one strong band for the W-F symmetric stretch is observed which is different from the multiple bands observed in WSF_4. This band compares with 694 cm^{-1} reported for $WOF_4 \cdot C_5H_5N$.[5] The small band at 525 cm^{-1} could easily be a result of ^{34}S-isotope instead of the more common ^{32}S.

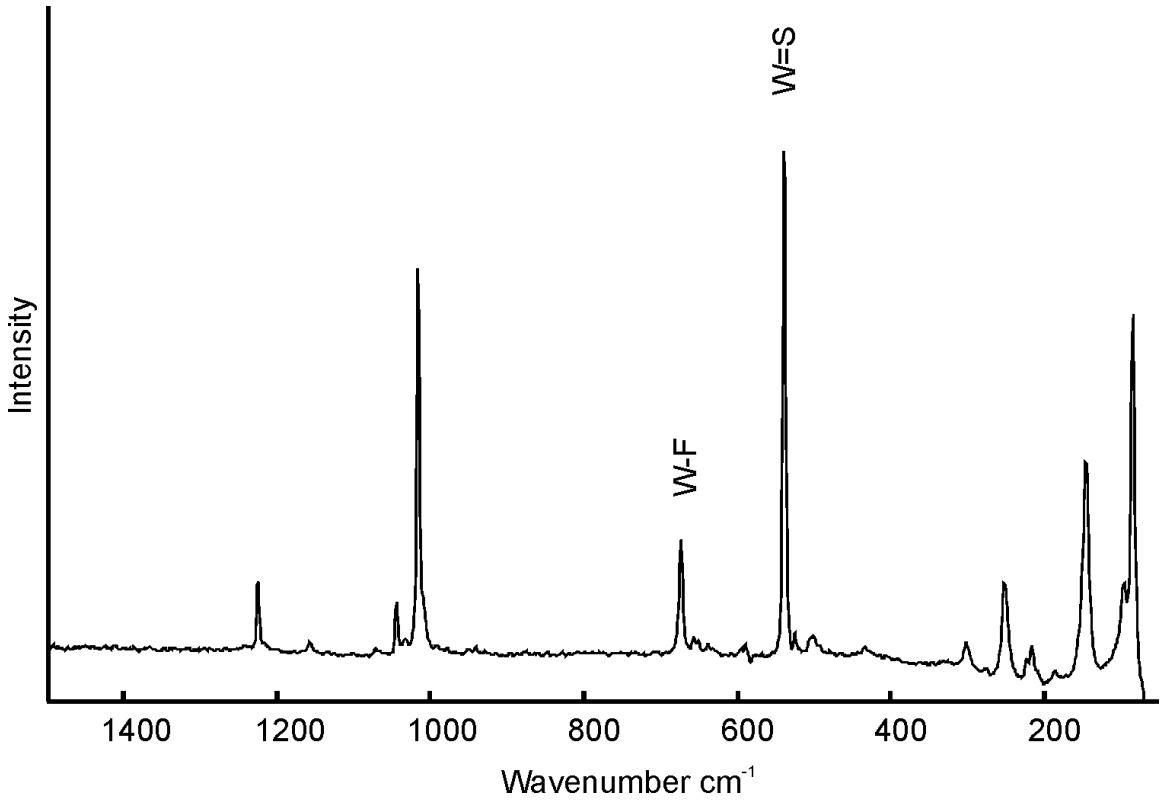

Figure 5.3.1 The Raman spectrum of solid $WSF_4 \cdot C_5H_5N$

Table 5.3.1 Comparison of Raman Spectroscopy of $WSF_4 \cdot C_5H_5N$ Adduct as Solid and in Solution with Free Pyridine

Frequency, cm^{-1}			
$WSF_4 \cdot C_5H_5N$ in Pyridine	$WSF_4 \cdot C_5H_5N$ Dark Solid	Pyridine [a]	Assignment [b]
3145 (3)	3146 (2)	3145 (3)	C-H Stretching
3091 (8)	3091 (16)	3091 (5)	
3056 (37)	3067 (17)	3056 (39)	
	3010 (2)		
1598 (5)	1610 (11)	1597 (5)	C-C and C-N Stretching
1581 (10)	1574 (6)	1581 (9)	
1573 (8)		1573 (7)	
1482 (4)	1491 (2)	1482 (3)	
1217 (10)	1225 (16)	1217 (8)	In-plane C-H Bending
1147 (4)	1157 (4)	1146 (2)	
1068 (3)	1072 (3)	1068 (2)	
1045 (4)	1044 (13)		
1030 (78)	1033 (6)	1030 (75)	In-plane ring def
1015 (15)	1016 (77)		
991 (100)		990 (100)	Sym stretching of ring
675 (4)	673 (25)		W-F stretching
	657 (6)		
652 (6)	650 (5)	652 (5)	In plane ring def
	639 (2)		W-F stretching
602 (3)		603 (3)	In plane ring def
	595 (1)		
	588 (2)		W-F Stretching
540 (12)	539 (100)		W = S Stretching
	525 (6)		Pyridine
504 (3)	501 (6)		
	493 (2)		
385 (3)	434 (2)	406 (1)	Out of plane ring def
	301 (8)		Def and lattice modes
	275 (2)		
247 (4)	251 (21)		
	224 (6)		
	215 (8)		
	185 (4)		
	145 (44)		
	96 (22)		

[a]Only Bands corresponding to $WSF_4 \cdot C_5H_5N$ Tabulated for Free Pyridine [b] Assignments from comparison with $WOF_4 \cdot C_5H_5N$ in Literature[5]

5.5 Summary

The new $[N(CH_3)_4][WSF_5]$ salt was prepared by two methods, through the addition of $[N(CH_3)4][F]$ to WSF_4 and directly from WF_6 and $[N(CH_3)_4][SSi(CH_3)_3]$. Experiments to produce $Cs[WSF_5]$ suffered from the lack of solubility of $Cs[SSi(CH_3)_3]$ in THF. Raman and infrared spectroscopy were used to study the WSF_5^- anion, which show a significant decrease in the frequency of the W=S stretching mode compared to WSF_4. It was also shown conclusively that the $W_2S_2F_9^-$ anion forms in an equilibrium reaction by combination of WSF_4 with WSF_5^- by ^{19}F NMR spectroscopy. The new mixed $W_2OSF_9^-$ anion was observed in solution for the first time. Density functional theory calculations were performed on the WSF_5^- anion and compared to the calculations performed on WSF_4, and values from literature. The calculated geometry of WSF_5^- was in close agreement with literature values from X-ray diffraction. The new Lewis acid/base adduct $WSF_4 \cdot C_5H_5N$ was prepared and characterized by Raman and ^{19}F NMR spectroscopy.

References

(1) Buslaev, Y. A.; Kokynov, Y. B.; Chubar, Y. D. *Proc. Acad. Sci.* **1973**, *213*, 912.

(2) Atherton, M. J.; Holloway, J. H. *J. Chem. Soc., Chem. Commun.* **1977**, 424.

(3) Prescott, A.; Sharp, D. W. A.; Winfield, J. M. *J.Chem. Soc., Dalton Trans.* **1975**, 934.

(4) Hilbers, M.; Lage, M.; Mattes, R. *Inorg. Chim. Acta,* **1992**, *201*, 1.

(5) Arnaudet, L.; Bougon, R.; Ban, B.; Charpin, P.; Isabey, J.; Lance, M.; Nierlich, M.; Vigner, J. *Inorg. Chem* **1989**, *28*, 257.

(6) Arnaudet, L.; Bougon, R.; Buu, B. *J. Fluorine Chem.* **1995**, *74*, 223.

(7) Kang, J.W.; Han, Y-K. *Bull. Korean Chem. Sot.* **1997**, *18*, 433.

Chapter 6

Preparation and Characterization of $MoSF_4$

6.1 Introduction

Molybdenum sulfide fluorides have been the subject of very little reported research. Few reports have mentioned their formation or characterization.[1,2] The synthesis of small amounts of $MoSF_4$ was reported in one publication.[1] The product was poorly characterized by a few infrared bands and mass spectrometry that showed significant amounts of hydrolysis products. No reliable preparation has been reported that produces pure $MoSF_4$ on a preparative scale. Methods of preparing $MoSF_4$ in reasonable quantities were investigated to aid in its unambiguous characterization.

6.2 Results and Discussion

6.2.1 Synthesis of $MoSF_4$

Molybdenum sulfide tetrafluoride was prepared most efficiently by reaction of MoF_6 with $((CH_3)_3Si)_2S$ in $CFCl_3$ at low temperature according to Equation 6.2.1. The reaction mixture began to turn yellow/brown even before the solvent had melted at *ca.* – 120 °C and had to be quenched several times to prevent the reaction from going out of control. The reaction was stirred once the solvent had melted at *ca.* -110 °C and slowly allowed to warm to room temperature. The solvent $CFCl_3$ was chosen as it has a low melting point allowing for the mixing reagents at low temperatures thus preventing localized heating which could lead to unwanted side reactions. Trichlorofluoromethane is oxidatively resistant compared to other solvents that would form miscible solutions with $((CH_3)_3Si)_2S$.

$$MoF_6 + ((CH_3)_3Si)_2S \xrightarrow{CFCl_3} MoSF_4 + 2\,(CH_3)_3SiF \qquad 6.2.1$$

The reaction produced a purple solid that settled from solution and was insoluble in $CFCl_3$. The sample was slowly warmed to room temperature where no further changes were observed. After removal of the $CFCl_3$ solvent at room temperature yellow/brown

$MoSF_4$ was isolated and characterized by X-ray crystallography, and Raman, infrared, and ^{19}F NMR spectroscopy.

Like WSF_4, $MoSF_4$ also seemed to undergo a colour change to a darker shade of brown after long periods at room temperature. Decomposition and increase in particle size are considered to be possible causes of the change in colour.

Prior to the successful method described (Equation 6.2.1) efforts were made to synthesize $MoSF_4$ using methods similar to those used for WSF_4. Reactions between MoF_6 and $((CH_3)_3Si)_2S$ in CH_3CN, however, yielded mainly MoF_5 and another undetermined product. The coloured solution slowly turned dark brown at room temperature.

When MoF_6 was reacted with Sb_2S_3 in HF a brown-coloured product was isolated. The products were a mixture containing mainly MoF_5 and some $MoSF_4$ according to ^{19}F NMR spectroscopy of the product dissolved in CH_3CN. The formation of $MoSF_4$ was believed to occur by Equation 6.2.2. The by-product of the reduction of Mo^{VI} to Mo^{V} has not been identified.

$$3\ MoF_6 + Sb_2S_3 \xrightarrow{aHF} 3\ MoSF_4 + 2\ SbF_3 \qquad 6.2.2$$

Conducting the reaction between MoF_6 and Sb_2S_3 in neat MoF_6 without solvent (Equation 6.2.3) resulted in a yellow solution at room temperature. After decanting the yellow solution and removing excess MoF_6 under dynamic vacuum at room temperature a yellow solid was isolated. The yellow solid was characterized by Raman and ^{19}F NMR spectroscopy in CH_3CN and single crystal X-ray diffraction. The product was found to be pure MoF_5. This reaction serves as a new preparative route for MoF_5.

$$MoF_6 + Sb_2S_3 \rightarrow MoF_5 + (\text{other products}) \qquad 6.2.3$$

Similar reactions between MoF_6 and Sb_2S_5 in HF (Equation 6.2.4) were also attempted as it was thought that Sb^{III} may have been involved in the reduction of MoF_6 experienced previously in reactions with Sb_2S_3. Upon removal of HF solvent the walls of the reaction vessel were coated with a yellow/orange powder. Fluorine-19 NMR

spectroscopy, in CH_3CN, showed that MoF_5 with a small amount of $MoSF_4$ had been produced.

$$5\ MoF_6 + Sb_2S_5 \xrightarrow{aHF} 5\ MoSF_4 + 2\ SbF_5 \qquad 6.2.4$$

Unlike reactions of WF_6 with H_2S, reactions involving MoF_6 and H_2S (Equation 6.2.5) were very exothermic and occurred instantaneously upon mixing even at -100 °C. A yellow/brown powder was isolated from the reaction at -110 °C. Fluorine-19 NMR spectroscopy indicated that moderate amounts of $MoSF_4$ were produced by this method along with MoF_5. The Raman spectrum of the sample did contain a band at 580 cm^{-1} indicative of Mo=S stretching of $MoSF_4$.

$$MoF_6 + H_2S \xrightarrow{CFCl_3} MoSF_4 + 2\ HF \qquad 6.2.5$$

The Mo=S bond was shown to be cleaved quite easily.[2] Since at least some $MoSF_4$ was produced in most of the reactions proposed it is likely that $MoSF_4$ acted as an intermediate to production of MoF_5. In products containing small amounts of $MoSF_4$ the Mo=S bond may have cleaved to form MoF_5. One possible driving force may have been a more favourable lattice energy for MoF_5 compared to $MoSF_4$.

6.2.2 X-ray Crystal Structure of $MoSF_4$

Crystals of $MoSF_4$ were grown in anhydrous HF solvent at a temperature slowly varied from -53 to -59 °C. The X-ray crystal structure of $MoSF_4$ was collected at -120 °C (Figure 6.2.1). The least squares refinement on F^2 resulted in an R_1 value of 2.24 % when data with intensity over 2σ was considered and 2.60 % when all of the data was considered. Information on collection and refinement is available in Table 6.2.1. The bond lengths and bond angles are listed in Table 6.2.2. All other information pertaining to the crystal structure is available in the Appendix.

Molybdenum sulfide tetrafluoride crystallizes in the orthorhombic space group $Pca2_1$ with the cell dimensions a = 1099.21(8), b = 829.57(6), c = 2777.4(2) pm. The structure contained six molecules per asymmetric unit giving 24 molecules per unit cell. Molybdenum sulfide tetrafluoride crystallizes in polymeric chains of *cis*-fluorine-bridged $MoSF_5$ octahedra with chain propagation along the *a*-axis of the unit cell. In comparison,

$MoOF_4$ crystallizes in the monoclinic $P2_1/c$ space group with unit cell dimensions a = 550(1), b = 1698(2), c = 784(1) pm. The much smaller unit cell contains only 8 molecules. The crystal structures of $MoSF_4$ and $MoOF_4$, however, are very similar. Molybdenum oxide tetrafluoride, also forms a *cis*-fluorine bridged polymeric chain structure of $MoOF_5$ octahedra, analogous to $MoSF_4$. The terminal Mo-F bond lengths are also similar as they range from 182(1) – 184(1) pm in $MoOF_4$ and from 181.1(3) – 184.8(3) pm in $MoSF_4$. The bridging fluorine bonds are also quite similar at 193(1) – 196(1) pm and 192.6(3) – 194.8(2) pm for $MoOF_4$ and $MoSF_4$, respectively. The Mo--F bond distances for fluorine atoms *trans* to the sulfur ranges from 225.4(2) – 229.5(2) pm, similar to the range for $MoOF_4$ of 227 – 231 pm. As expected the bond length of Mo-S in $MoSF_4$ is much longer than the Mo-O bond in $MoOF_4$. The bond angles in the two structures are also in agreement.[3]

It was found that $MoSF_4$ is isostructural with $ReSF_4$ which also has six molecular units in the asymmetric unit with unit cell edge lengths of a = 1089.3(10), b = 827.8(11), c = 2766.3(5) pm.[4] Both structures were *cis*-fluorine bridged polymeric chain structures of MSF_5 octahdra (where M = Mo, Re), similar to WSF_4.

It is apparent upon analysis of the bonds about each molybdenum centre (Table 6.2.3) that the environments are similar about the six crystallographically independent molybdenum atoms; because of this only the angles about three molybdenum centers were given in Table 6.2.3. The Ranges in bond length for particular bonds are given in Table 6.2.2. A complete listing of bond angles is available in the Appendix.

The thermal ellipsoids of some terminal fluorine atoms are elongated perpendicular to the bonding axis. The ellipsoid elongation of the terminal F(3) and F(4) atoms are particularly significant, indicating residual motion in the crystal structure.

Table 6.2.1 Crystal Data and Structure Refinement for $MoSF_4$

Empirical formula	$MoSF_4$
Formula weight, g mol^{-1}	204.00
Temperature, K	153(2)
Wavelength, pm	71.073
Crystal system	Orthorhombic
Space group	$Pca2_1$
Unit cell dimensions, pm	a = 1099.21(8)
	b = 829.57(6)
	c = 2777.4(2)
Volume, 10^6 pm^3	2.5326(3)
Z	24
Density (calculated), mg mm^{-3}	3.210
Absorption coefficient, mm^{-1}	3.542
F(000)	2256
Crystal size, mm^3	0.1 x 0.06 x 0.05
Theta range for data collection	2.46 to 28.47°.
Index ranges	$-14 \leq h \leq 14$, $-11 \leq k \leq 11$, $-36 \leq l \leq 37$
Reflections collected	28014
Independent reflections	6165 [R(int) = 0.0301]
Completeness to theta = 28.47°, %	98.4
Refinement method	Full-matrix least-squares on F^2
Data / restraints / parameters	6165 / 1 / 326
Goodness-of-fit on F^2	1.074
Final R indices [$I>2\sigma(I)$]	R_1 = 0.0224, wR_2 = 0.0427
R indices (all data)	R_1 = 0.0260, wR_2 = 0.0438
Absolute structure parameter	0.07(3)
Extinction coefficient	0.00000(2)
Largest diff. peak and hole, e 10^{-6} pm^{-3}	0.654 and -0.435

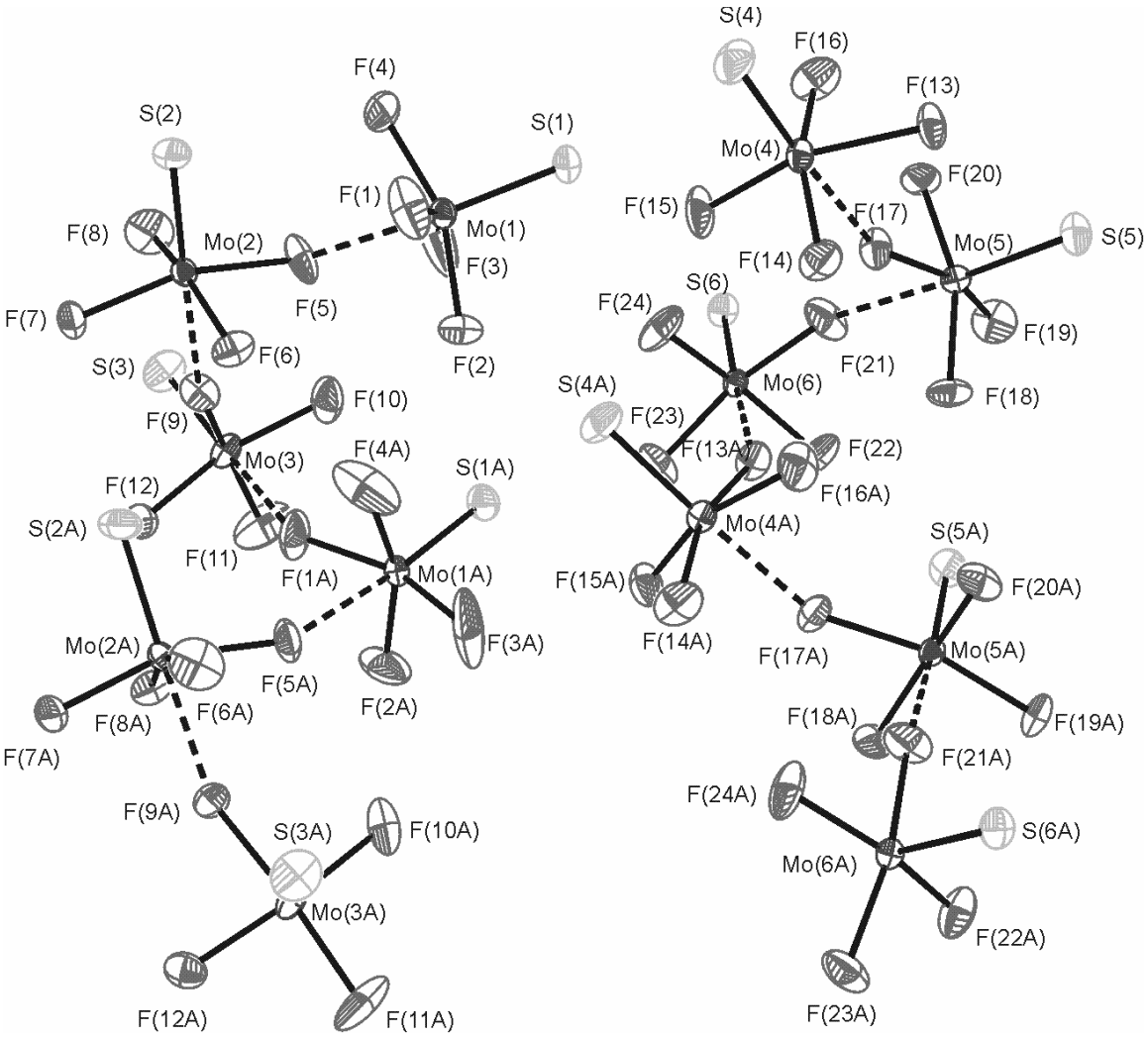

Figure 6.2.1 The X-ray crystal structure showing the chain structure of $MoSF_4$. The data was collected at -120 °C with thermal ellipsoids drawn at 50 % probability.

Table 6.2.2 Ranges of Bond Lengths from the X-ray Crystal Structure of $MoSF_4$

Bonds	Bond Lengths, pm
Mo-$F_{terminal}$	181.1(3) – 184.8(3)
Mo-F_{bridge} *cis* to Mo=S	192.6(3) – 194.8(2)
Mo--F_{bridge} *trans* to Mo=S	225.4(2) – 229.5(2)
Mo=S	205.69(12) – 206.58(13)

Table 6.2.3 Bond Lengths and Bond Angles from X-ray Crystal Structure of $MoSF_4$

Bond Lengths, pm		Bond Angles, deg. [a]	
		Angles about Mo(1)	
		F_{term}–Mo–F_{term}	
Mo(1)-F(3)	181.1(3)	F(3)-Mo(1)-F(2)	91.9(2)
Mo(1)-F(2)	182.1(3)	F(3)-Mo(1)-F(4)	91.8(2)
Mo(1)-F(4)	182.4(3)	F(2)-Mo(1)-F(1)	83.69(17)
Mo(1)-F(1)	193.7(3)	F(4)-Mo(1)-F(1)	85.30(19)
Mo(1)-S(1)	205.69(12)	S=Mo–F	
Mo(1)-F(5)	229.1(3)	F(3)-Mo(1)-S(1)	101.34(11)
Mo(2)-F(6)	182.2(2)	F(2)-Mo(1)-S(1)	101.68(11)
Mo(2)-F(7)	184.5(3)	F(4)-Mo(1)-S(1)	99.65(11)
Mo(2)-F(8)	184.5(3)	F(1)-Mo(1)-S(1)	98.31(9)
Mo(2)-F(5)	192.6(3)	S(1)-Mo(1)-F(5)	174.98(8)
Mo(2)-S(2)	206.20(13)	F_{term}–Mo–F_{brig}	
Mo(2)-F(9)	225.4(2)	F(3)-Mo(1)-F(5)	82.43(12)
Mo(3)-F(11)	182.5(3)	F(2)-Mo(1)-F(5)	81.40(13)
Mo(3)-F(10)	183.1(3)	F(4)-Mo(1)-F(5)	76.78(13)
Mo(3)-F(12)	184.6(3)	F(1)-Mo(1)-F(5)	77.99(11)
Mo(3)-F(9)	194.8(2)	Angles About Mo(2)	
Mo(3)-S(3)	206.58(13)	F_{term}–Mo–F_{term}	
Mo(4)-F(15)	182.7(3)	F(6)-Mo(2)-F(7)	90.86(12)
Mo(4)-F(16)	183.0(3)	F(7)-Mo(2)-F(8)	89.95(14)
Mo(4)-F(14)	184.1(2)	F(6)-Mo(2)-F(5)	86.17(12)
Mo(4)-F(13)	194.3(2)	F(8)-Mo(2)-F(5)	85.91(14)
Mo(4)-S(4)	206.52(13)	S=Mo–F	
Mo(4)-F(17)	229.5(2)	F(6)-Mo(2)-S(2)	100.53(9)
Mo(5)-F(20)	183.5(2)	F(7)-Mo(2)-S(2)	100.14(9)
Mo(5)-F(19)	183.6(3)	F(8)-Mo(2)-S(2)	100.19(11)
Mo(5)-F(18)	184.0(2)	F(5)-Mo(2)-S(2)	99.68(9)
Mo(5)-F(17)	193.0(3)	S(2)-Mo(2)-F(9)	178.46(8)
Mo(5)-S(5)	206.49(12)	F_{term}–Mo–F_{brig}	
Mo(5)-F(21)	225.7(3)	F(6)-Mo(2)-F(9)	79.76(10)
Mo(6)-F(23)	183.1(3)	F(7)-Mo(2)-F(9)	81.36(11)
Mo(6)-F(24)	184.0(3)	F(8)-Mo(2)-F(9)	79.40(12)
Mo(6)-F(22)	184.8(3)	F(5)-Mo(2)-F(9)	78.81(10)
Mo(6)-F(21)	193.0(3)	Angles About Mo(3)	
Mo(6)-S(6)	205.89(11)	F_{term}–Mo–F_{term}	
Mo(6)-F(13)#4	229.0(2)	F(11)-Mo(3)-F(10)	92.50(18)
F(13)-Mo(6)#5	229.0(2)	F(11)-Mo(3)-F(12)	91.07(16)
F(1)-Mo(5)#2	225.6(3)	F(10)-Mo(3)-F(9)	86.31(13)
		F(12)-Mo(3)-F(9)	83.12(11)
		S=Mo–F	
		F(11)-Mo(3)-S(3)	101.60(12)
		F(10)-Mo(3)-S(3)	100.14(10)
		F(12)-Mo(3)-S(3)	101.66(9)
		F(9)-Mo(3)-S(3)	96.69(9)

[a] Only bond angles for three molybdenum centres are shown.

6.2.3 X-ray Crystal Structure of MoF_5

Reaction between neat MoF_6 and Sb_2S_3 at room temperature resulted in crystals of MoF_5 (Figure 6.2.2) which were studied by X-ray crystallography. The structure was anisotropically refined, resolved with a residual R_1 value of 1.47 %. Complete crystallographic information for MoF_5 can be found in the Appendix.

Molybdenum pentafluoride crystallizes in the monoclinic *C2/m* space group. The unit cell dimensions of our improved crystal structure are a = 951.4(1), b = 1417.4(2), c = 512.66(6) pm with angle β = 95.6620(10)°. The literature unit cell dimensions of MoF_5 are a = 961(1), b = 1422(2), c = 516(1) pm where the structure was refined with a much larger residual value of 12 %.[5]

Molybdenum pentafluoride crystallizes as a fluorine-bridged tetramer. Mo(2) and the terminal fluorine atoms F(4) and F(6) are located on a crystallographic mirror plane. The second molybdenum atom, Mo(1), is located on a crystallographic two-fold rotational axis. The MoF_5 tetramer displays symmetric Mo─F─Mo bridging unlike $MoSF_4$. The Mo-$F_{terminal}$ bonds *tran*s to bridging Mo-F bonds range from 181.49(13) to 182.10(13) pm in length while the Mo-$F_{terminal}$ bonds cis to bridging Mo-F bonds are shorter ranging from 179.86(13) to 179.96(19) pm. The Mo-F_{bridge} bond lengths are significantly larger than the Mo-$F_{terminal}$ bond lengths, ranging from 204.46(12) to 204.95(12) pm.

The ligand environment about molybdenum is pseudo-octahedral with *trans*-bond angles F(3)-Mo(1)-F(2) of 177.87(6)° and *cis*-bond angles F(3)-Mo(1)-F(1) of 83.93°. The bond angles between terminal Mo-F bonds range from 95.79(7) ° to 96.37(6)°, while the bond angles between terminal and bridging Mo-F bonds are much smaller ranging from 83.13(6) to 83.93 °

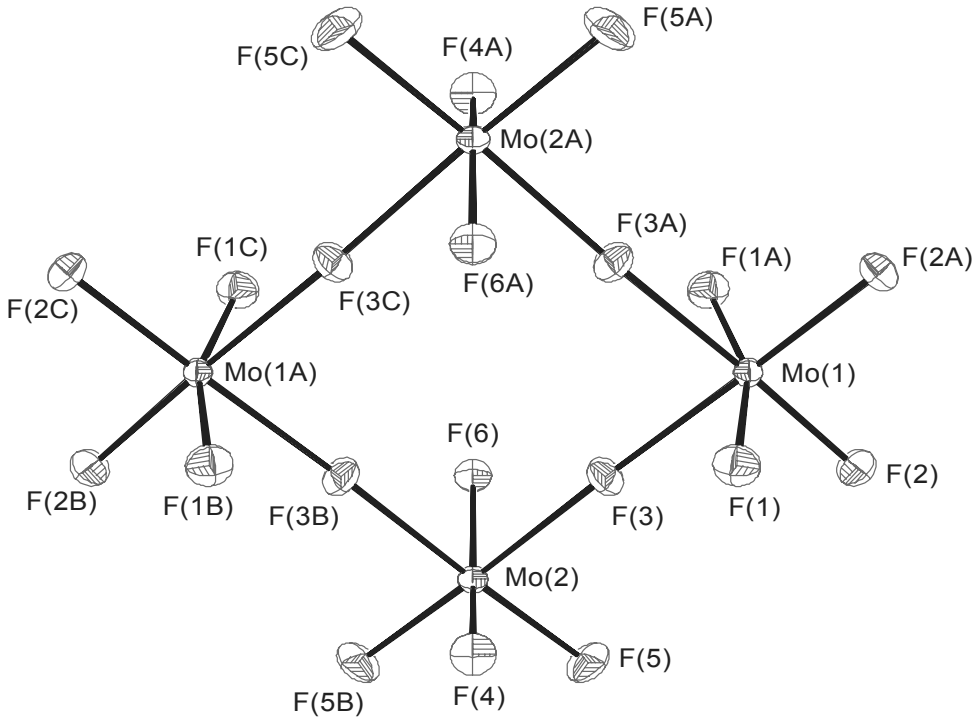

Figure 6.2.2 The X-ray crystal structure of the MoF_5 tetramer. The Data was collected at -120 °C and Thermal Ellipsoids at 50 % Probability)

6.2.4 NMR Spectroscopy of $MoSF_4$ and MoF_5

Fluorine-19 NMR spectroscopy was performed on solutions of $MoSF_4$ (Figure 6.2.4) and MoF_5 (Figure 6.2.5) in CH_3CN at room temperature. The chemical shifts and available coupling constants are listed in Table 6.2.4.

A solution of $MoSF_4$ in CH_3CN gave rise to a singlet at 155.0 ppm in the ^{19}F NMR spectrum. This chemical shift is significantly higher than the chemical shift of $MoOF_4$ at +145.9 but much lower than MoF_6 which had been reported at +278 ppm. This is similar to WSF_4 as WOF_4 has a smaller chemical shift and WF_6 has a much larger chemical shift than WSF_4, though the difference in chemical shifts between sulfide and oxide-containing species is much less.[6] No satellites from $^1J(^{95}Mo\text{-}^{19}F)$ could be observed for $MoSF_4$ as ^{95}Mo is quadrupolar and expected to undergo rapid relaxation in the asymmetric environment.

Molybdenum pentafluoride dissolved in CH_3CN resulted in a ^{19}F NMR signal at +149.2 ppm with poorly resolved ^{95}Mo-satellites at its base (Figure 6.2.5). The paramagnetic nature of MoF_5 would be expected to broaden the ^{19}F NMR signals to the

point where it would not be observable; furthermore, a paramagnetic centre at molybdenum would erase all *J*-coupling information. Raman spectroscopy (*vide infra*) and single crystal X-ray crystallography verified the purity of the MoF_5. A possible explanation for the observation of the signal at +149.2 ppm in the ^{19}F NMR spectrum is the formation of a diamagnetic MoF_5 dimer containing a Mo-Mo bond (Figure 6.2.3). The fluorine atoms are expected to be in the fast-exchange regime on the NMR time scale, rendering all fluorine environments equivalent. The symmetry about the molybdenum atoms would be close to octahedral allowing for relatively slow quadrupolar relaxation and the observation of ^{95}Mo satellites in the ^{19}F NMR spectrum.

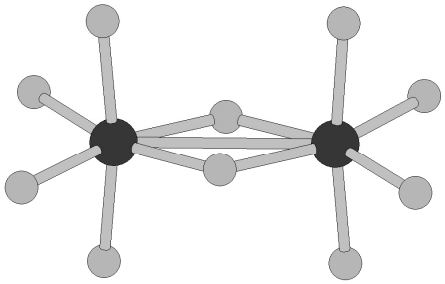

Figure 6.2.3 A possible structure of the MoF_5 dimer in CH_3CN solution

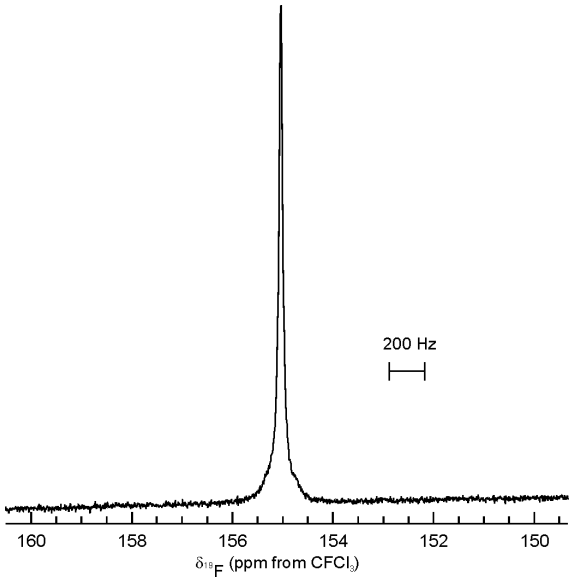

Figure 6.2.4 The ^{19}F NMR spectrum of $MoSF_4$ in CH_3CN at room temperature.

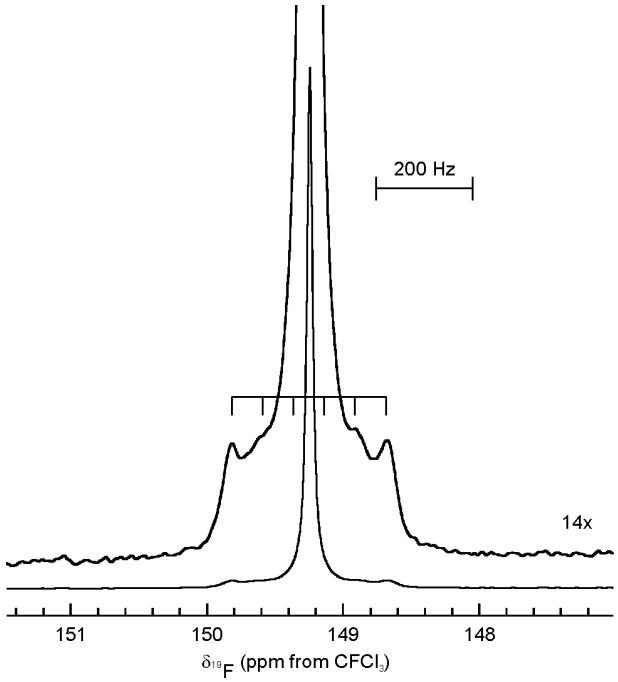

Figure 6.2.5 The ^{19}F NMR spectrum of MoF_5 in CH_3CN at room temperature

Table 6.2.4 ^{19}F NMR Spectroscopy Data of $MoSF_4$ and Related Species in Various Solvents at Room Temperature.

Chemical Shift (ppm) [a]	Solvent	$^1J(^{19}F\text{-}^{95}Mo)$ (Hz)	Assignment
155.0 s	CH_3CN		$MoSF_4 \cdot CH_3CN$
283.7 s	MoF_6	48.0	MoF_6

[a] Abbreviation denotes, singlet (s)

6.2.5 Vibrational Spectroscopy

The Raman spectrum of $MoSF_4$ was collected (Figure 6.2.6) on freshly produced $MoSF_4$ in a melting point capillary at room temperature. The infrared spectrum of $MoSF_4$ was collected as a KBr pellet formed inside the dry box. The vibrational bands are listed in Table 6.2.5 together with the tentative assignments. The Raman spectrum of MoF_5 was also collected (Figure 6.2.7) at room temperature as a test of the purity for the yellow solid obtained with the values listed in Table 6.2.6

The infrared spectrum of $MoSF_4$ contained bands at 671 and 648 cm^{-1} corresponding to terminal Mo-F stretching modes. Holloway *et al*. reported strong bands in the same area at 690, 670, and 633 cm^{-1}. A band at 562 cm^{-1} corresponding to Mo=S stretching was observed, comparing closely to the literature value of 564 cm^{-1}. Bridging Mo-F stretching modes were observed at 518 and 511 cm^{-1}, while the literature reported bridging Mo-F stretching bands significantly lower at 500 and 458 cm^{-1}.[1]

The Raman spectrum (Figure 6.2.6) of $MoSF_4$ was very similar to that of WSF_4. The same level of resolution could not be achieved which was most likely a result of the large number of molybdenum isotopes with masses between 92 and 100 u. The Raman spectrum displayed several terminal Mo-F stretching bands in the range 608 – 724 cm^{-1}, Mo=S stretching bands were displayed at 580 and 563 cm^{-1}, while bridging Mo-F and *trans* Mo---F bond stretching were observed from 492 - 536 cm^{-1} and 450 to 488 cm^{-1}, respectively.

The similarity in frequencies for stretching bands of $MoSF_4$ and WSF_4 was unexpected considering that molybdenum is approximately half the mass of tungsten. This same trend is observed for WOF_4 and $MoOF_4$. Spectroscopic data on the oxide fluorides, WOF_4 and $MoOF_4$, show very similar metal-oxygen stretches of 1056 and 1049 cm^{-1}, respectively.[7] This similarity in stretching frequency can only be attributed to weaker bond strengths for the molybdenum (VI) compounds. The Mo=S bond was found to be easily cleaved yielding MoF_5.[2]

Comparison of the crystal structures of $MoOF_4$ and $MoSF_4$ shows very similar bond lengths for the Mo-F bonds. It could therefore be reasonably expected that the Mo-F stretching modes would have similar stretching frequencies. This is observed in that

terminal Mo-F stretches are found around 700 cm^{-1} and bridging stretches are found around 500 cm^{-1} for both compounds.[3]

The Raman spectrum of MoF_5 (Figure 6.2.7) was basically identical to the Raman spectra of solid MoF_5 reported in the literature.[8,9] The differences in the collected spectrum versus the literature spectra were small differences in the relative intensities of bands; in addition the lower signal-to-noise ratio did not allow for the observation of weak signals that were reported in the literature (Table 6.2.6). The methods used to produce MoF_5 in the literature involved the reduction of MoF_6 with molybdenum metal followed by sublimation in a Pyrex apparatus [9] and material sublimed on the sides of a quartz reaction vessel during a one-stage reaction to generate MoF_3.[8] It is not unreasonable to assume that the MoF_5 generated by reaction of neat MoF_6 with Sb_2S_3 is of greater purity than the MoF_5 used in the Raman vibrational studies of MoF_5 found in the literature.

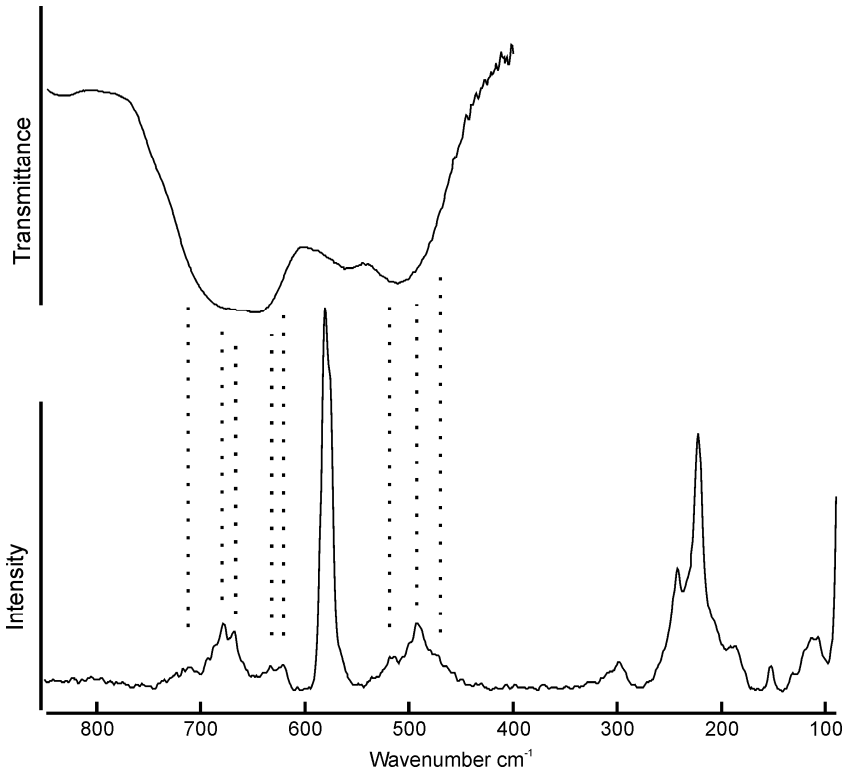

Figure 6.2.6 Vibrational spectroscopy of Solid $MoSF_4$ at room temperature. The Raman spectrum (lower trace) was recorded on the neat solid in a glass melting point capillary. The infrared spectrum (upper trace) was recorded as a KBr pellet.

Table 6.2.5 Vibrational Spectroscopy Data of $MoSF_4$

Frequency,[a] cm^{-1}			
Raman[b]	Infrared[c]	Literature [1] Infrared	Assignment
724 (3)			
717 (4)			
709 (5)			
693 (7)		690 s	
678 (17)			$\nu(Mo–F_{terminal})$
668 (14)	671 sh	670 s	
633 (6)	648 vs br	633 s	
620 (6)			
608 (1)			
580 (100)			$\nu(Mo=S)$
563 (sh)	562 s	564	
533 (3)			
518 (8)	519 sh		$\nu(Mo–F_{bridge})$
514 (8)	511 vs		
500 (sh)		500	
492 (17)			$\nu(Mo---F)$
472 (sh)		458	
310 (sh)			
298 (7)			
242 (32)			
222 (67)			$\delta(Mo=S)$
206 (sh)			
191 (11)			
187 (11)			
152 (6)			
132 (4)			
121 (sh)			
112 (13)			
107 (13)			

[a] Abbreviations denote shoulder (sh), broad (br), very strong (vs), and strong (s). [b] Neat solid in melting point capillary at room temperature. [c] KBr pellet at room temperature.

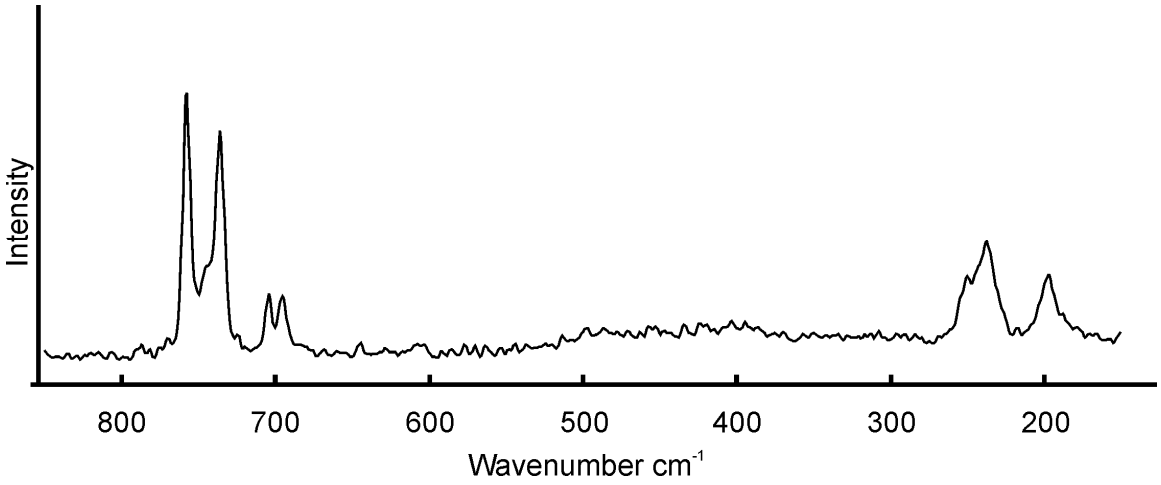

Figure 6.2.7 The Raman spectrum of crystalline MoF_5 recorded at room t temperature in a glass melting point capillary

Table 6.2.6 Raman Spectroscopy Data Recorded for MoF_5 at Room Temperature in a Glass Melting Point Capillary.

Frequency, cm^{-1}		
MoF_5 Yellow Solid	Literature [8 a] (Crystal)	Assignment [8] (C_{2h})
757 (100)	759 s	ν_1 (A_1')
744 (36)	747 m	ν_5 (E')
736 (86)	738 s	ν_1 (A_1')
704 (25)	706 m	ν_2 (A_1')
695 (24)	696 m	
	684 w	
	494 vw	
	436 w	
	402	
	332	
	282	
250 (25)	252 m	
244 (sh)		ν_6 (E')
238 (39)	239 m	
197 (26)	199 m	ν_7 (E')
	181 w	

[a] Abbreviations denote, strong (s), medium (m), weak (w), weak (w), very weak (vw)

6.2.6 Density Functional Theory Calculations

Calculations were performed on the $MoSF_4$ monomer (Figure 6.2.8) in the gas phase with Gaussian 98 at the B3LYP/LANL2DZ level of theory.

The calculated molecular geometry was of C_{4v} point group symmetry. The bond lengths and angles of the calculated molecule are listed in Table 6.2.7 and compare well with those of the solid shown in the X-ray crystal structure. Like the case of WSF_4 the calculated bond lengths are slightly larger than those observed. The bridging fluorine present in the actual structure could explain this, as it would withdraw significant electron density. The S=Mo–F angle at 104 ° for the calculated molecule is slightly larger than the *ca.* 100 ° found in the crystal structure while the F_{term}–Mo–F_{term} angle is slightly less than the *ca.* 91 ° found in the solid. The structures are quite close and deviations are attributable to fluorine bridging.

Calculated bond vibrations are shown in Table 6.2.8. Many of the frequencies compare well to within a few wavenumbers with the experimental values. The calculated Mo=S stretching mode at 568 cm^{-1} was close to those observed at 580 and 562 cm^{-1} in the Raman and infrared spectra, respectively. The close correlation of the Mo=S stretch indicates that the bridging does not have a large effect on the stretching frequency of the Mo=S bond. The calculated Mo-F bond stretching frequencies show surprising similarity to the Mo-F_{term} stretching frequencies found in the solid indicating that the bonds are not greatly affected by the bridging fluorine atoms.

Like WSF_4, monomeric $MoSF_4$ was expected to be found in a square pyramidal geometry with C_{4v} point group symmetry. Therefore the group theory applied in Chapter 4 to WSF_4 would be identical. Therefore the stretching vibrations have symmetry, $\Gamma_{stretch} = 2\ A_1 + B_1 + E$ and bending vibrations, $\Gamma_{bend} = A_1 + B_1 + B_2 + 2\ E$.

When the calculated vibrational frequencies for $MoSF_4$ are compared to those for WSF_4 (see Chapter 4), it is interesting to note that the ν_s(Mo–F), (A_1) band at 680 cm^{-1} appears below the ν_{as}(Mo–F), (E) band at 704 cm^{-1}, while for WSF_4 the reverse sequence is found.

Comparison of the calculations to actual vibrational data for $MoSF_4$ vapour is not possible as such studies have not been performed.

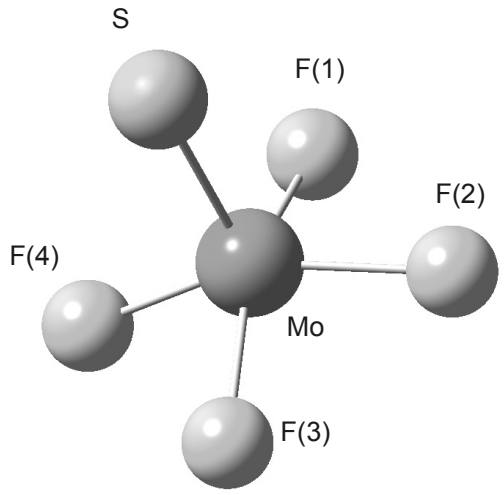

Figure 6.2.8 The calculated geometry of $MoSF_4$ in C_{4v} symmetry using density functional theory at the B3LYP/LANL2DZ level of theory.

Table 6.2.7 Calculated Bond Lengths and Angles for $MoSF_4$ using Density Functional Theory at the B3LYP/LANL2DZ Level of Theory.

Bond Length, pm	Assignment
188.7	Mo–F
212.6	Mo=S
Bond Angles, °	
104.3	S=Mo–F
86.5	F–Mo–F

Table 6.2.8 Calculated Vibrational Frequencies for $MoSF_4$ using Density Functional Theory at the B3LYP/LANL2DZ Level of Theory.

Frequency, cm^{-1}	Raman Activity	Infrared Intensity	Assignment	
704	1.9	184	$\nu_{as}(MoF_4)$	$\nu_7(E)$,
680	15	76	$\nu_s(MoF_4)$	$\nu_2(A_1)$
587	6.7	0	$\nu(MoF_4)$	$\nu_4(B_1)$
568	25	18	ν(MoS)	$\nu_1(A_1)$
301	2.9	0	δ	$\nu_6(B_2)$
239	2.4	6	δ	$\nu_3(A_1)$
207	0	18	δ(SMoF)	$\nu_8(E)$
195	6.8	0.8	δ	$\nu_9(E)$
113	0.4	0	δ	$\nu_5(B_1)$

6.3 Summary

Molybdenum sulfide tetrafluoride was prepared in large amounts by a facile process at low temperature. Raman, infrared, and ^{19}F NMR spectroscopy were used to characterize the resulting yellow/brown solid. The previously unknown crystal structure of $MoSF_4$ was successfully solved and refined from the X-ray diffraction data showing a *cis*-fluorine-bridged polymeric chain structure of $MoSF_5$ octahedra very similar to structures observed for $MoOF_4$ and $ReSF_4$. Calculations on monomeric $MoSF_4$ bond stretching frequencies showed a reasonable agreement with the vibrational frequencies observed in the vibrational spectra of the solid.

A new reliable room temperature synthesis of MoF_5 was also discovered. Molybdenum pentafluoride was studied by ^{19}F NMR spectroscopy in CH_3CN and an improved crystal structure was obtained.

References

(1) Holloway, J. H.; Puddick, D. C. *Inorg. Nucl. Chem. Letters* **1979**, *15*, 85.

(2) Malkerova, I. P.; Alikhanyan, A. S.; Gorgoraki, V. I. *Russ. J. Inorg. Chem.* **1980**, *25*, 1742.

(3) Edwards, A. J.; Steventon, B. R. *J. Chem. Soc. A.* **1968**, 2503.

(4) Holloway, J. H.; Kaucic, V.; Russell, D. R. *J. Chem. Soc., Chem. Commun.* **1983**, 1079.

(5) Edwards, A. J.; Peacock, R. D.; Small, R. W. H. *J. Chem. Soc.* **1962**, 4486.

(6) Berger, S.; Braun, S.; Kalinowski, H. O. *^{19}F NMR Spectroskopie*; Georg Thieme Verlag: Stuttgart, 1994.

(7) Weidlein, J.; Muller, U.; Dehnicke, K. *Schwingunsfrequenzen II*; Georg Thieme Verlag: Stuttgart, 1986.

(8) Bates, J. B. *Spectrochim. Acta.* **1971**, *27*, 1255.

(9) Quellette, T. J.; Ratcliffe, C. T.; Sharp, D. W. A. *J. Chem. Soc.* **1969**, 2351.

Chapter 7

Conclusions and Future Work

I have shown that trimethylsilanethiolate salts are useful sulfur-transfer agent for inorganic fluorine chemistry. The $[N(CH_3)_4][SSi(CH_3)_3]$ reagent was used for the preparation of $[N(CH_3)_4][WSF_5]$ salt. Their ability to generate sulfide fluoride anions directly from metal fluorides is expected to be extended to other metals in high oxidation states. The commercial availability of $((CH_3)_3Si)_2Se$ and $((CH_3)_3Si)_2Te$ raises the possibility to synthesize the new trimethylsilylselenide and telluride reagents $[N(CH_3)_4][SeSi(CH_3)_3]$ and $[N(CH_3)_4][TeSi(CH_3)_3]$, respectively. These salts could serve as reagents for the generation of the $WSeF_5^-$ and $WTeF_5^-$ anions.

The facile method described in this thesis for production of bulk quantities of pure WSF_4 allows for the detailed study of its reaction behavior. The pyridine adduct, $WSF_4 \cdot C_5H_5N$, was produced and characterized in this work, showcasing the Lewis acidity of WSF_4. Other organic donor molecules could be used to form a wide variety of adducts. The Lewis basicity of WSF_4 has been investigated with SbF_5 in preliminary experiments and require the unambiguous characterization of the reaction products.

The novel $W_2OSF_9^-$ anion was observed by ^{19}F NMR spectroscopy in a mixture with $W_2S_2F_9^-$ in CH_3CN. The production of $W_2OSF_9^-$ from WOF_4 and WSF_5^- in solution would allow for the isolation of its salts and the full characterization of this mixed anion.

The successful bulk production and full characterization of $MoSF_4$ demonstrates that such reactive compounds can be generated and stored for an extended period of time. Very little is known about molybdenum sulfide fluorides. The ability to generate $MoSF_4$ reliably on a preparative scale makes possible the study of its fluoride-ion donor and acceptor properties. The information provided by such research could expand our knowledge of the chemistry of elements in group six.

Appendix

Table A.1.1 Crystal Data and Structure Refinement for WF_5.

Empirical formula	WF_5
Formula weight, g mol^{-1}	278.85
Temperature, K	293(2)
Wavelength , pm	71.073
Crystal system	Monoclinic
Space group	*C2/m*
Unit cell dimensions, pm	a = 956.5(10)
	b = 1437.0(15) β = 96.494(10)°.
	c = 506.0(5)
Volume, 10^6 pm^3	0.6910(12)
Z	8
Density (calculated), mg mm^{-3}	5.361
Absorption coefficient, mm^{-1}	33.410 mm^{-1}
F(000)	952
Theta range for data collection	2.57 to 28.68°.
Index ranges	-12<=h<=12, -18<=k<=19, -6<=l<=6
Reflections collected	4013
Independent reflections	889 [R(int) = 0.0175]
Completeness to theta = 28.68°, %	95.6 %
Refinement method	Full-matrix least-squares on F^2
Data / restraints / parameters	889 / 0 / 61
Goodness-of-fit on F^2	1.272
Final R indices [I>2sigma(I)]	R1 = 0.0221, wR2 = 0.0665
R indices (all data)	R1 = 0.0236, wR2 = 0.0671
Extinction coefficient	0.00021(10)
Largest diff. peak and hole, e 10^6 pm^{-3}	1.757 and -1.465

Table A.1.2. Atomic coordinates (x 10^4) and equivalent isotropic displacement parameters (pm^2x 10^{-1}) for WF_5. U(eq) is defined as one third of the trace of the orthogonalized U^{ij} tensor.

x	y	z	U(eq)	
W(1)	0	2932(1)	5000	18(1)
W(2)	2640(1)	5000	2341(1)	19(1)
F(5)	3618(4)	4068(3)	1412(8)	18(1)
F(6)	3395(5)	5000	5845(10)	10(1)
F(1)	1077(4)	3148(3)	8173(7)	8(1)
F(3)	1201(4)	4058(2)	3756(7)	10(1)
F(4)	1337(5)	5000	-585(10)	8(1)
F(2)	1167(5)	2167(3)	3756(9)	16(1)

Table A.1.3. Bond Lengths [pm] and Angles [°] for WF_5.

W(1)-F(2)	173.4(4)
W(1)-F(2)#1	173.4(4)
W(1)-F(1)	183.3(4)
W(1)-F(1)#1	183.3(4)
W(1)-F(3)#1	212.1(4)
W(1)-F(3)	212.1(4)
W(2)-F(5)#2	172.8(4)
W(2)-F(5)	172.8(4)
W(2)-F(4)	182.4(5)
W(2)-F(6)	183.7(5)
W(2)-F(3)#2	211.3(4)
W(2)-F(3)	211.3(4)
F(2)-W(1)-F(2)#1	101.4(3)
F(2)-W(1)-F(1)	95.98(19)
F(2)#1-W(1)-F(1)	96.3(2)
F(2)-W(1)-F(1)#1	96.3(2)
F(2)#1-W(1)-F(1)#1	96.0(2)
F(1)-W(1)-F(1)#1	160.5(2)
F(2)-W(1)-F(3)#1	169.58(18)
F(2)#1-W(1)-F(3)#1	89.05(18)
F(1)-W(1)-F(3)#1	83.14(16)
F(1)#1-W(1)-F(3)#1	82.01(16)
F(2)-W(1)-F(3)	89.05(18)
F(2)#1-W(1)-F(3)	169.58(18)
F(1)-W(1)-F(3)	82.01(16)
F(1)#1-W(1)-F(3)	83.14(16)
F(3)#1-W(1)-F(3)	80.5(2)
F(5)#2-W(2)-F(5)	101.6(3)
F(5)#2-W(2)-F(4)	96.92(18)
F(5)-W(2)-F(4)	96.92(18)
F(5)#2-W(2)-F(6)	95.56(17)
F(5)-W(2)-F(6)	95.56(17)
F(4)-W(2)-F(6)	160.2(2)
F(5)#2-W(2)-F(3)#2	89.35(18)
F(5)-W(2)-F(3)#2	169.05(17)
F(4)-W(2)-F(3)#2	82.15(17)
F(6)-W(2)-F(3)#2	82.68(16)
F(5)#2-W(2)-F(3)	169.05(17)
F(5)-W(2)-F(3)	89.35(18)
F(4)-W(2)-F(3)	82.15(17)
F(6)-W(2)-F(3)	82.68(16)
F(3)#2-W(2)-F(3)	79.7(2)
W(2)-F(3)-W(1)	170.09(19)

Symmetry transformations used to generate equivalent atoms:
#1 -x,y,-z+1 #2 x,-y+1,z

Table A.1.4. Anisotropic displacement parameters ($pm^2 x\ 10^{-1}$) for WF_5. The anisotropic displacement factor exponent takes the form: $-2\pi^2[\ h^2 a^{*2} U^{11} + ... + 2\ h\ k\ a^*\ b^*\ U^{12}\ ]$

	U^{11}	U^{22}	U^{33}	U^{23}	U^{13}	U^{12}
W(1)	22(1)	9(1)	21(1)	0	-8(1)	0
W(2)	10(1)	35(1)	13(1)	0	3(1)	0
F(5)	17(2)	17(2)	20(2)	-2(2)	5(2)	9(2)
F(6)	9(2)	17(3)	3(2)	0	1(2)	0
F(1)	11(2)	10(2)	4(2)	0(1)	-1(1)	-1(1)
F(3)	10(2)	8(2)	12(2)	2(1)	3(1)	1(1)
F(4)	5(2)	10(2)	7(2)	0	-2(2)	0
F(2)	13(2)	16(2)	19(2)	-2(2)	6(2)	5(2)

Table A.2.1. Crystal Data and Structure Refinement for MoF_5

Empirical formula	MoF_5	
Formula weight	190.94	
Temperature, K	296(2)	
Wavelength, pm	71.073	
Crystal system	Monoclinic	
Space group	*C*2/*m*	
Unit cell dimensions, pm	a = 951.45(11)	
	b = 1417.42(16)	β = 95.6620(10)°
	c = 512.66(6)	
Volume, 10^6 pm^3	0.68800(14)	
Z	8	
Density (calculated), mg mm^{-3}	3.939	
Absorption coefficient, mm^{-1}	4.346	
F(000)	752	
Theta range for data collection	2.59 to 28.65°.	
Index ranges	-12<=h<=12, -18<=k<=18, -6<=l<=6	
Reflections collected	3931	
Independent reflections	864 [R(int) = 0.0148]	
Completeness to theta = 28.65°, %	93.8	
Refinement method	Full-matrix least-squares on F^2	
Data / restraints / parameters	864 / 0 / 61	
Goodness-of-fit on F^2	1.220	
Final R indices [I>2sigma(I)]	R_1 = 0.0147, wR_2 = 0.0365	
R indices (all data)	R_1 = 0.0151, wR_2 = 0.0367	
Extinction coefficient	0.00102(15)	
Largest diff. peak and hole, e 10^{-6} pm^{-3}	0.688 and -0.561	

Table A.2.2. Atomic coordinates (x 10^4) and equivalent isotropic displacement parameters (pm^2x 10^{-1}) for MoF_5. U(eq) is defined as one third of the trace of the orthogonalized U^{ij} tensor.

	x	y	z	U(eq)
Mo(1)	0	2040(1)	10000	12(1)
Mo(2)	2592(1)	0	7473(1)	12(1)
F(3)	1266(1)	1010(1)	8710(3)	21(1)
F(1)	1033(1)	1845(1)	13083(3)	21(1)
F(2)	1158(2)	2926(1)	8779(3)	21(1)
F(4)	3316(2)	0	10850(4)	22(1)
F(5)	3720(1)	926(1)	6396(3)	25(1)
F(6)	1351(2)	0	4586(4)	20(1)

Table A.2.3. Bond Lengths [pm] and Angles [°] for MoF_5

Mo(1)-F(1)#1	179.86(13)
Mo(1)-F(1)	179.86(13)
Mo(1)-F(2)#1	182.10(13)
Mo(1)-F(2)	182.10(13)
Mo(1)-F(3)#1	204.46(12)
Mo(1)-F(3)	204.46(12)
Mo(2)-F(4)	179.90(19)
Mo(2)-F(6)	179.96(19)
Mo(2)-F(5)	181.49(13)
Mo(2)-F(5)#2	181.49(13)
Mo(2)-F(3)#2	204.95(12)
Mo(2)-F(3)	204.95(12)
F(1)#1-Mo(1)-F(1)	162.31(9)
F(1)#1-Mo(1)-F(2)#1	96.38(6)
F(1)-Mo(1)-F(2)#1	95.79(7)
F(1)#1-Mo(1)-F(2)	95.79(7)
F(1)-Mo(1)-F(2)	96.38(6)
F(2)#1-Mo(1)-F(2)	92.90(9)
F(1)#1-Mo(1)-F(3)#1	83.45(6)
F(1)-Mo(1)-F(3)#1	83.93(6)
F(2)#1-Mo(1)-F(3)#1	89.16(6)
F(2)-Mo(1)-F(3)#1	177.87(6)
F(1)#1-Mo(1)-F(3)	83.93(6)
F(1)-Mo(1)-F(3)	83.45(6)
F(2)#1-Mo(1)-F(3)	177.87(6)
F(2)-Mo(1)-F(3)	89.16(6)
F(3)#1-Mo(1)-F(3)	88.78(7)
F(4)-Mo(2)-F(6)	161.63(9)
F(4)-Mo(2)-F(5)	96.37(6)
F(6)-Mo(2)-F(5)	96.29(6)
F(4)-Mo(2)-F(5)#2	96.37(6)
F(6)-Mo(2)-F(5)#2	96.29(6)
F(5)-Mo(2)-F(5)#2	92.62(9)
F(4)-Mo(2)-F(3)#2	83.75(6)
F(6)-Mo(2)-F(3)#2	83.13(6)
F(5)-Mo(2)-F(3)#2	177.95(6)
F(5)#2-Mo(2)-F(3)#2	89.40(6)
F(4)-Mo(2)-F(3)	83.75(6)
F(6)-Mo(2)-F(3)	83.13(6)
F(5)-Mo(2)-F(3)	89.40(6)
F(5)#2-Mo(2)-F(3)	177.95(6)
F(3)#2-Mo(2)-F(3)	88.58(7)
Mo(1)-F(3)-Mo(2)	178.11(8)

Symmetry transformations used to generate equivalent atoms:
#1 -x,y,-z+2 #2 x,-y,z

Table A.2.4. Anisotropic displacement parameters ($pm^2 x\ 10^{-1}$)for MoF_5. The anisotropic displacement factor exponent takes the form: $-2\pi^2[\ h^2a^{*2}U^{11} + ... + 2\ h\ k\ a^*\ b^*\ U^{12}\ ]$

	U^{11}	U^{22}	U^{33}	U^{23}	U^{13}	U^{12}
Mo(1)	11(1)	10(1)	16(1)	0	4(1)	0
Mo(2)	10(1)	12(1)	16(1)	0	5(1)	0
F(3)	20(1)	17(1)	28(1)	-3(1)	8(1)	5(1)
F(1)	20(1)	23(1)	19(1)	2(1)	1(1)	1(1)
F(2)	18(1)	17(1)	29(1)	5(1)	6(1)	-4(1)
F(4)	23(1)	24(1)	18(1)	0	2(1)	0
F(5)	22(1)	25(1)	29(1)	1(1)	10(1)	-10(1)
F(6)	17(1)	20(1)	21(1)	0	0(1)	0

Table A.3.1. Atomic coordinates (x 10^4) and equivalent isotropic displacement parameters (pm^2x 10^{-1}) for $MoSF_4$ U(eq) is defined as one third of the trace of the orthogonalized U^{ij} tensor.

	x	y	z	U(eq)
Mo(1)	3973(1)	4540(1)	890(1)	19(1)
Mo(4)	2573(1)	3785(1)	-455(1)	17(1)
Mo(6)	-131(1)	1243(1)	224(1)	23(1)
S(7)	4184(1)	4702(2)	-719(1)	35(1)
S(9)	708(1)	-823(2)	-26(1)	42(1)
Mo(2)	5762(1)	10473(1)	2058(1)	19(1)
Mo(3)	4448(1)	9090(1)	3396(1)	18(1)
Mo(5)	2294(1)	5652(1)	2729(1)	16(1)
S(8)	3176(1)	3534(1)	2896(1)	26(1)
S(1)	4973(1)	5449(2)	1454(1)	31(1)
S(3)	5396(1)	10912(2)	3736(1)	33(1)
S(2)	6777(1)	11181(2)	1469(1)	38(1)
F(9)	1463(3)	6063(3)	3295(1)	39(1)
F(7)	4707(2)	9768(3)	2739(1)	29(1)
F(1)	1690(2)	3632(4)	-1018(1)	34(1)
F(5)	2984(3)	3625(3)	218(1)	39(1)
F(8)	2947(2)	10042(3)	3327(1)	34(1)
F(4)	865(3)	1735(4)	731(1)	45(1)
F(3)	1785(2)	5642(3)	-294(1)	29(1)
F(2)	837(2)	2767(3)	-148(1)	31(1)
F(25)	4532(2)	11980(3)	2045(1)	36(1)
F(16)	5686(2)	7633(3)	3310(1)	34(1)
F(15)	3501(3)	7115(3)	2982(1)	41(1)
F(17)	2941(3)	6054(3)	2130(1)	43(1)
F(14)	4764(3)	8973(4)	1782(1)	44(1)
F(12)	6767(3)	8936(4)	2314(1)	43(1)
F(13)	6456(2)	11903(3)	2539(1)	30(1)
F(10)	-1268(2)	1620(3)	-252(1)	32(1)
F(11)	2903(3)	1607(3)	-484(1)	47(1)
F(22)	889(3)	4867(4)	2464(1)	43(1)
F(18)	4066(3)	6390(4)	466(1)	52(1)
F(19)	-1300(3)	408(4)	619(1)	65(1)
F(20)	2462(3)	5320(5)	1024(1)	61(1)
F(21)	5201(3)	3717(5)	523(1)	79(1)
F(23)	3891(3)	7954(4)	3919(1)	40(1)
F(24)	3578(4)	2561(4)	1116(1)	91(2)

Table A.3.2 Bond Lengths [pm] and Angles [°] for $MoSF_4$.

Mo(1)-F(3)	181.1(3)
Mo(1)-F(2)	182.1(3)
Mo(1)-F(4)	182.4(3)
Mo(1)-F(1)	193.7(3)
Mo(1)-S(1)	205.69(12)
Mo(1)-F(5)	229.1(3)
Mo(2)-F(6)	182.2(2)
Mo(2)-F(7)	184.5(3)
Mo(2)-F(8)	184.5(3)
Mo(2)-F(5)	192.6(3)
Mo(2)-S(2)	206.20(13)
Mo(2)-F(9)	225.4(2)
Mo(3)-F(11)	182.5(3)
Mo(3)-F(10)	183.1(3)
Mo(3)-F(12)	184.6(3)
Mo(3)-F(9)	194.8(2)
Mo(3)-S(3)	206.58(13)
Mo(3)-F(1)#1	225.6(3)
Mo(4)-F(15)	182.7(3)
Mo(4)-F(16)	183.0(3)
Mo(4)-F(14)	184.1(2)
Mo(4)-F(13)	194.3(2)
Mo(4)-S(4)	206.52(13)
Mo(4)-F(17)	229.5(2)
Mo(5)-F(20)	183.5(2)
Mo(5)-F(19)	183.6(3)
Mo(5)-F(18)	184.0(2)
Mo(5)-F(17)	193.0(3)
Mo(5)-S(5)	206.49(12)
Mo(5)-F(21)	225.7(3)
Mo(6)-F(23)	183.1(3)
Mo(6)-F(24)	184.0(3)
Mo(6)-F(22)	184.8(3)
Mo(6)-F(21)	193.0(3)
Mo(6)-S(6)	205.89(11)
Mo(6)-F(13)#4	229.0(2)
F(13)-Mo(6)#5	229.0(2)
F(1)-Mo(5)#2	225.6(3)

Bond Angles [°]	
F(3)-Mo(1)-F(2)	91.9(2)
F(3)-Mo(1)-F(4)	91.8(2)
F(2)-Mo(1)-F(4)	157.18(15)
F(3)-Mo(1)-F(1)	160.35(13)
F(2)-Mo(1)-F(1)	83.69(17)
F(4)-Mo(1)-F(1)	85.30(19)
F(3)-Mo(1)-S(1)	101.34(11)
F(2)-Mo(1)-S(1)	101.68(11)
F(4)-Mo(1)-S(1)	99.65(11)
F(1)-Mo(1)-S(1)	98.31(9)
F(3)-Mo(1)-F(5)	82.43(12)
F(2)-Mo(1)-F(5)	81.40(13)
F(4)-Mo(1)-F(5)	76.78(13)
F(1)-Mo(1)-F(5)	77.99(11)
S(1)-Mo(1)-F(5)	174.98(8)
F(6)-Mo(2)-F(7)	90.86(12)
F(6)-Mo(2)-F(8)	158.78(13)
F(7)-Mo(2)-F(8)	89.95(14)
F(6)-Mo(2)-F(5)	86.17(12)
F(7)-Mo(2)-F(5)	160.17(12)
F(8)-Mo(2)-F(5)	85.91(14)
F(6)-Mo(2)-S(2)	100.53(9)
F(7)-Mo(2)-S(2)	100.14(9)
F(8)-Mo(2)-S(2)	100.19(11)
F(5)-Mo(2)-S(2)	99.68(9)
F(6)-Mo(2)-F(9)	79.76(10)
F(7)-Mo(2)-F(9)	81.36(11)
F(8)-Mo(2)-F(9)	79.40(12)
F(5)-Mo(2)-F(9)	78.81(10)
S(2)-Mo(2)-F(9)	178.46(8)
F(11)-Mo(3)-F(10)	92.50(18)
F(11)-Mo(3)-F(12)	91.07(16)
F(10)-Mo(3)-F(12)	156.71(12)
F(11)-Mo(3)-F(9)	161.58(14)
F(10)-Mo(3)-F(9)	86.31(13)
F(12)-Mo(3)-F(9)	83.12(11)
F(11)-Mo(3)-S(3)	101.60(12)
F(10)-Mo(3)-S(3)	100.14(10)
F(12)-Mo(3)-S(3)	101.66(9)
F(9)-Mo(3)-S(3)	96.69(9)
F(11)-Mo(3)-F(1)#1	82.88(15)
F(10)-Mo(3)-F(1)#1	79.06(12)
F(12)-Mo(3)-F(1)#1	78.56(11)
F(9)-Mo(3)-F(1)#1	78.85(12)
S(3)-Mo(3)-F(1)#1	175.50(11)
F(15)-Mo(4)-F(16)	92.88(15)
F(15)-Mo(4)-F(14)	90.76(14)
F(16)-Mo(4)-F(14)	157.44(13)
F(15)-Mo(4)-F(13)	160.02(13)
F(16)-Mo(4)-F(13)	85.49(13)
F(14)-Mo(4)-F(13)	83.55(12)
F(15)-Mo(4)-S(4)	100.71(11)
F(16)-Mo(4)-S(4)	100.34(10)
F(14)-Mo(4)-S(4)	100.84(10)
F(13)-Mo(4)-S(4)	99.17(8)
F(15)-Mo(4)-F(17)	82.45(12)
F(16)-Mo(4)-F(17)	78.89(12)
F(14)-Mo(4)-F(17)	79.54(11)
F(13)-Mo(4)-F(17)	77.68(10)
S(4)-Mo(4)-F(17)	176.79(8)
F(20)-Mo(5)-F(19)	90.68(13)
F(20)-Mo(5)-F(18)	159.05(12)
F(19)-Mo(5)-F(18)	90.26(13)
F(20)-Mo(5)-F(17)	87.68(12)
F(19)-Mo(5)-F(17)	161.11(12)
F(18)-Mo(5)-F(17)	84.71(12)
F(20)-Mo(5)-S(5)	99.65(9)
F(19)-Mo(5)-S(5)	100.52(11)

F(18)-Mo(5)-S(5)	100.75(10)	F(23)-Mo(6)-F(13)#4	83.28(12)
F(17)-Mo(5)-S(5)	98.31(8)	F(24)-Mo(6)-F(13)#4	77.65(11)
F(20)-Mo(5)-F(21)	78.31(11)	F(22)-Mo(6)-F(13)#4	80.43(10)
F(219)-Mo(5)-F(21)	82.91(13)	F(21)-Mo(6)-F(13)#4	78.63(11)
F(18)-Mo(5)-F(21)	81.04(11)	S(6)-Mo(6)-F(13)#4	175.61(8)
F(17)-Mo(5)-F(21)	78.32(11)	Mo(5)-F(17)-Mo(4)	158.14(14)
S(5)-Mo(5)-F(21)	176.08(9)	Mo(2)-F(5)-Mo(1)	151.55(14)
F(23)-Mo(6)-F(24)	91.48(15)	Mo(3)-F(9)-Mo(2)	154.96(14)
F(23)-Mo(6)-F(22)	89.53(14)	Mo(6)-F(21)-Mo(5)	163.53(17)
F(24)-Mo(6)-F(22)	157.78(12)	Mo(4)-F(13)-Mo(6)#5	149.03(14)
F(23)-Mo(6)-F(21)	161.75(13)	Mo(1)-F(1)-Mo(3)#2	153.10(16)
F(24)-Mo(6)-F(21)	87.05(14)		
F(22)-Mo(6)-F(21)	85.11(14)		
F(23)-Mo(6)-S(6)	100.61(11)		
F(24)-Mo(6)-S(6)	100.09(9)		
F(22)-Mo(6)-S(6)	101.53(9)		
F(21)-Mo(6)-S(6)	97.56(9)		

Symmetry transformations used to generate equivalent atoms:
#1 x-1/2,-y+1,z #2 x-1/2,-y+2,z #3 x+1/2,-y+2,z
#4 x+1/2,-y+1,z

Table A.3.3. Anisotropic displacement parameters ($pm^2 x\ 10^{-1}$) for $MoSF_4$. The anisotropic displacement factor exponent takes the form: $-2\pi^2[\ h^2a^{*2}U^{11} + ... + 2\ h\ k\ a^*\ b^*\ U^{12}\ ]$

	U^{11}	U^{22}	U^{33}	U^{23}	U^{13}	U^{12}
Mo(1)	22(1)	19(1)	16(1)	1(1)	-2(1)	2(1)
Mo(4)	18(1)	16(1)	18(1)	-2(1)	-3(1)	2(1)
Mo(6)	33(1)	16(1)	21(1)	2(1)	8(1)	0(1)
S(7)	21(1)	46(1)	37(1)	-9(1)	3(1)	-5(1)
S(9)	53(1)	20(1)	52(1)	-4(1)	6(1)	7(1)
Mo(2)	24(1)	16(1)	17(1)	-2(1)	0(1)	-2(1)
Mo(3)	19(1)	14(1)	20(1)	3(1)	1(1)	1(1)
Mo(5)	20(1)	14(1)	15(1)	-1(1)	1(1)	1(1)
S(8)	33(1)	16(1)	28(1)	0(1)	-1(1)	4(1)
S(1)	33(1)	37(1)	22(1)	-6(1)	-4(1)	-2(1)
S(3)	40(1)	31(1)	27(1)	-5(1)	-3(1)	-6(1)
S(2)	43(1)	44(1)	27(1)	-2(1)	13(1)	-10(1)
F(9)	54(2)	33(1)	29(2)	5(1)	19(1)	14(1)
F(7)	38(2)	29(1)	21(1)	1(1)	3(1)	-11(1)
F(1)	29(2)	53(2)	20(1)	-4(1)	-4(1)	-6(1)
F(5)	51(2)	43(2)	24(1)	11(1)	-19(1)	-18(1)
F(8)	21(1)	31(1)	50(2)	3(1)	2(1)	11(1)
F(4)	65(2)	44(2)	26(2)	-2(1)	-11(1)	18(2)
F(3)	32(1)	16(1)	40(2)	-1(1)	9(1)	1(1)
F(2)	33(2)	26(1)	35(2)	11(1)	-2(1)	-9(1)
F(25)	38(2)	43(2)	28(1)	3(1)	0(1)	16(1)
F(16)	25(1)	26(1)	50(2)	-5(1)	-3(1)	11(1)
F(15)	38(2)	18(1)	66(2)	-3(1)	-18(1)	-7(1)
F(17)	63(2)	40(2)	26(2)	10(1)	21(1)	20(1)
F(14)	55(2)	45(2)	31(2)	-16(1)	0(1)	-27(1)
F(12)	47(2)	35(2)	46(2)	7(1)	4(1)	19(1)
F(13)	41(2)	25(1)	24(1)	-5(1)	-4(1)	-15(1)
F(10)	30(1)	30(1)	37(2)	-8(1)	-2(1)	-2(1)
F(11)	53(2)	19(1)	69(2)	-6(1)	-4(2)	11(1)
F(22)	37(2)	39(2)	53(2)	-3(1)	-24(2)	-4(1)
F(18)	78(2)	44(2)	33(2)	18(1)	-17(2)	-31(2)
F(19)	72(2)	56(2)	67(2)	24(2)	44(2)	0(2)
F(20)	23(2)	105(3)	54(2)	-19(2)	-1(1)	13(2)
F(21)	44(2)	129(4)	65(2)	-67(2)	-11(2)	39(2)
F(23)	47(2)	42(2)	32(2)	19(1)	6(1)	-6(1)
F(24)	173(4)	41(2)	58(2)	29(2)	-71(3)	-46(2)

Table A.4.1. Atomic coordinates (x 10^4) and equivalent isotropic displacement parameters (pm^2x 10^{-1}) for WSF_4. U(eq) is defined as one third of the trace of the orthogonalized U^{ij} tensor.

	x	y	z	U(eq)
W(1)	3725(1)	6601(1)	5328(1)	16(1)
W(2)	3458(1)	9686(1)	9252(1)	16(1)
S(2)	3593(2)	10870(4)	11342(2)	28(1)
S(1)	4749(1)	5198(5)	6251(3)	31(1)
F(4)	3270(3)	8275(10)	6959(5)	26(1)
F(7)	3854(3)	6487(8)	9345(6)	34(1)
F(8)	2434(3)	8123(9)	9381(5)	33(1)
F(5)	2908(3)	12277(9)	8444(5)	31(1)
F(1)	3013(3)	4131(9)	5726(5)	28(1)
F(2)	3832(3)	5534(10)	3482(5)	29(1)
F(6)	4385(3)	10752(11)	8441(5)	34(1)
F(3)	4025(3)	9758(9)	4804(6)	33(1)

Table A.4.2. Anisotropic displacement parameters ($pm^2 x\ 10^{-1}$)for WSF_4. The anisotropic displacement factor exponent takes the form: $-2\pi^2[\ h^2 a^{*2} U^{11} + ... + 2\ h\ k\ a^*\ b^*\ U^{12}\ ]$

	U^{11}	U^{22}	U^{33}	U^{23}	U^{13}	U^{12}
W(1)	16(1)	18(1)	13(1)	-1(1)	2(1)	2(1)
W(2)	17(1)	18(1)	12(1)	-1(1)	-1(1)	-2(1)
S(2)	38(1)	31(1)	14(1)	-3(1)	-5(1)	-8(1)
S(1)	23(1)	39(1)	31(1)	1(1)	-2(1)	9(1)
F(4)	24(3)	38(3)	16(2)	-3(2)	1(2)	8(2)
F(7)	46(3)	23(3)	32(3)	4(3)	-9(3)	11(2)
F(8)	26(3)	53(3)	20(2)	-8(3)	5(2)	-16(2)
F(5)	43(3)	27(3)	22(3)	5(2)	-5(2)	9(2)
F(1)	29(3)	30(3)	26(3)	-3(2)	-3(2)	-8(2)
F(2)	36(3)	32(3)	19(3)	-7(2)	6(2)	6(2)
F(6)	23(3)	50(3)	28(3)	-1(2)	2(2)	-14(3)
F(3)	41(3)	26(3)	33(3)	-3(2)	12(2)	1(2)